

Clean porphyrin films on a silver (111) surface:
a Scanning Tunneling Microscopy study

Den Naturwissenschaftlichen Fakultäten
der Friedrich-Alexander-Universität Erlangen-Nürnberg
zur
Erlangung des Doktorgrades

vorgelegt von

Karmen Comănici
aus Călărași (Rumänien)

Als Dissertation genehmigt von den Naturwissenschaftlichen Fakultäten
der Universität Erlangen-Nürnberg

Tag der mündlichen Prüfung:

Vorsitzender der Promotionskommission: Prof. Dr. E. Bänsch

Erstberichterstatter: Prof. Dr. H.-P. Steinrück

Zweitberichterstatter: Prof. Dr. R. Fink

The important thing is not to stop questioning.

Albert Einstein

Table of contents

Table of contents	i
Abbreviations	iii
1. Introduction.....	4
2. Experimental	7
2.1. Scanning Tunneling Microscopy (STM)	7
2.1.1. Tunneling effect	9
2.1.2. The Tersoff Hamann model	12
2.1.3. STM image processing	15
2.2. Quadrupol mass spectrometry (QMS)	17
2.3. Low energy electron diffraction (LEED).....	19
2.4. Ultraviolet photoelectron spectroscopy (UPS)	23
3. Experimental set-up.....	25
3.1. Main chamber	25
3.2. Preparation chamber	30
3.3. Sample preparation	31
3.3.1. Ag (111) preparation.....	32
3.3.2. Porphyrin deposition.....	32
4. Theoretical background and Literature overview	35
4.1. Short description of porphyrins.....	35

4.2. Porphyrins on surfaces	38
4.3. Electronic properties of organic molecules on surfaces	45
4.4. 2D-Chirality on surface.....	53
5. Results	57
5.1. Atomic resolution on Ag(111)	57
5.2. Arrangements of TPP molecules	62
5.3. Arrangement of TTBP molecules	68
5.4. Identification of distinct features in Co-porphyrin layers.....	74
5.5. 2D-Chirality of non-chiral molecules	83
5.6. Investigating the multilayer regime	85
5.7. Temperature stability of porphyrin layers.....	90
6. Summary.....	94
8. Zusammenfassung	96
List of figures.....	98
Bibliography	102

Abbreviations

2H-TPP	meso-Tetraphenylporphyrin
Ag	Silver
Co-TPP	Copper(II)- meso-Tetraphenylporphyrin
Co-TTBPP	Copper(II) tetrakis(3,5-di- <i>tert</i> -butylphenyl) porphyrin
fcc	face centered cubic
HOMO	Highest occupied molecular orbital
IRAS	Infra-red adsorption spectroscopy
LDOS	Local density of states
LEED	Low Energy Electron Diffraction
LUMO	Lowest unoccupied molecular orbital
QMS	Quadrupole Mass Spectrometer
STM	Scanning tunnelling microscopy
UHV	Ultra high vacuum
UPS	Ultraviolet Photoelectron Spectroscopy
UV	Ultra-violet
XPS	X-ray Photoelectron Spectroscopy
Zn-TPP	Zinc(II)- meso-Tetraphenylporphyrin

1. Introduction

Organic molecules are building blocks of living systems and of novel materials and devices. The organization of these molecules on solid surfaces is a possibility to realize molecular devices. An important group of such molecules is represented by porphyrins. The molecules from the porphyrin class have gained interest from the scientific community due to their potential in technological applications, because of biologically important porphyrins such as chlorophyll and hemoglobin molecules that play a vital role in life processes.

A porphyrin is a heterocyclic macrocycle made from four pyrrole subunits linked on opposite sides through four methine bridges. The heterocyclic macrocycle in which no metal is inserted in its cavity is called a free base. A porphyrin with metals coordinated in the central cavity is called metalloporphyrin. Well-known metal containing porphyrins are the iron-(heme), magnesium-(chlorophyll), zinc-, copper-, nickel-, and cobalt-porphyrins. Other metals can also be inserted in the cavity. Some iron-containing porphyrins are called hemes. Hemoglobin, a heme-containing porphyrin is important in biochemistry. Hemoglobin iron is the actual transfer site for oxygen and could be preferentially bound up with carbon monoxide, thus poisoning by asphyxiation can occur. The magnesium-containing reduced porphyrin (one of the four pyrrole subunits is reduced to pyrroline producing a chlorine) found in chlorophyll is important in the photosynthesis process.

One of the interesting things about porphyrins is how small variations on the basic structural theme of the tetrapyrrolic macrocycle, lead to a wide diversity of biochemical functions. Keeping or reversibly changing the oxidation state of the involved central metal atom is crucial for the functionality of the porphyrin in natural and technological processes.

Fig.1.1 shows the sketches of the core porphyrin structure and of a metal porphyrin.

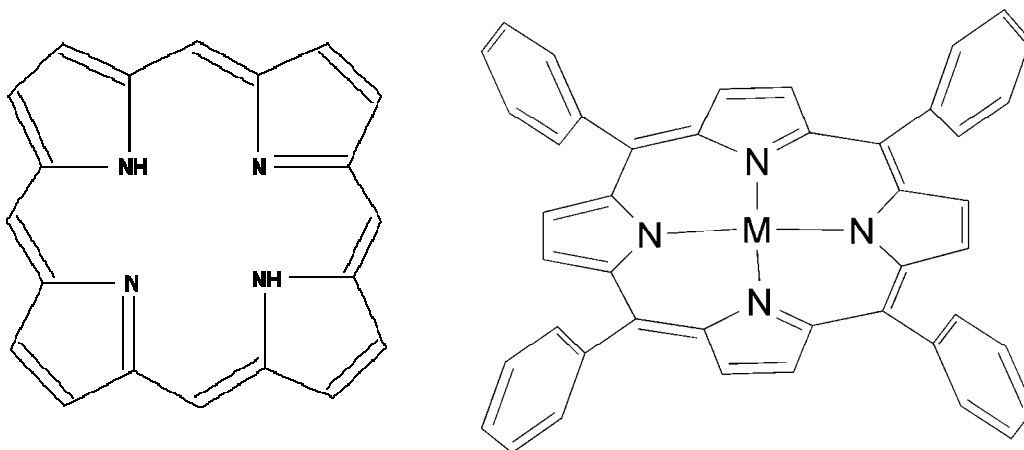


Fig.1.1 Sketches for the core porphyrin and a typical metalloporphyrin.

The way to adjust the basic molecular properties of the porphyrins is to change the ligands or the central metal atom. Therefore, the porphyrins thin films are important in many field of application, e.g., metalloporphyrins can act as catalysts.

The scanning probe methods are a powerful tool to investigate molecules on the surface. They permit to determine properties such as shape, size, diffusion, conductivity, etc., of individual molecules on surfaces for the first time [1]. The different types of scanning probe microscopes provide the possibility of investigating periodic and non-periodic, electrical, topographic, optical, magnetic and many other types of surface properties with atomic resolution.

In the present thesis, the focus was the investigation of self-assembled porphyrin monolayers via scanning tunneling microscopy in ultra high vacuum. The main theme is a part of the project A9 "Adsorption and Reactivity of Redoxactive Metallo-porphyrins", within the Sonderforschungsbereich 583 „Redox-Active Metal Complexes: Control of Reactivity via Molecular Architecture". One method to produce porphyrin films in UHV research is vacuum thermal sublimation [1-3]. The vacuum thermal evaporation deposition technique consists in heating until evaporation of the material to be deposited. The material vapor finally condenses in form of thin film on the cold substrate surface and on the vacuum chamber walls. Usually low pressures are used. With this method, one can obtain films with high purity in a controlled way. This method is also compatible with the techniques used by the traditional Surface Science, i.e., techniques, which require ultra high vacuum. One limitation is that only the molecules, which do not decompose by the heating, can

sublimated in vacuum. The substrate surface represents here a template for a well-defined molecular architecture, on which the characteristics of the porphyrins can be examined without the disturbing influence of solvents.

This work reports the scanning tunneling microscopy studies of 2H-TPP, Zn-TPP, Co-TPP and Co-TTBPP molecules. The thesis is structured as follows: after a brief general introduction, chapter 2 serves as an introduction into the fundamental concepts of scanning tunneling microscopy, and some aspects of mass spectrometry and electron diffraction. Chapter 3 describes the ultrahigh vacuum chambers used for sample preparation and sample investigation. Chapter 4 introduces the porphyrin molecules and puts together some results of the studied porphyrins on different substrates. Chapter 5 presents the result obtained by scanning tunneling microscopy of the porphyrin molecules adsorbed on the silver surface.

In summary, this thesis provides answers to questions related to the molecular arrangement of the porphyrin molecules, about the identification of distinct topographic / electronic features in porphyrin layers and the temperature dependency for porphyrin layers.

2. Experimental

2.1. Scanning Tunneling Microscopy (STM)

Scanning tunneling microscopy (STM) is a powerful technique to image surfaces with extremely high spatial resolution (below 0.1 \AA). The development of the scanning probe microscopes started with the invention of the STM in 1982 [4]. The first working STM was developed by Gerd Binnig and Heinrich Rohrer at the IBM Zürich Research Laboratories in Switzerland. In 1986, they were awarded a Nobel Prize for their invention.

The principle of scanning tunneling microscope (STM) is based on the so-called tunneling effect. Due to this effect, a tunneling current starts to flow when a sharp tip approaches a surface at a distance of approximately one nanometer. The tip and the sample must be conductors or semiconductors.

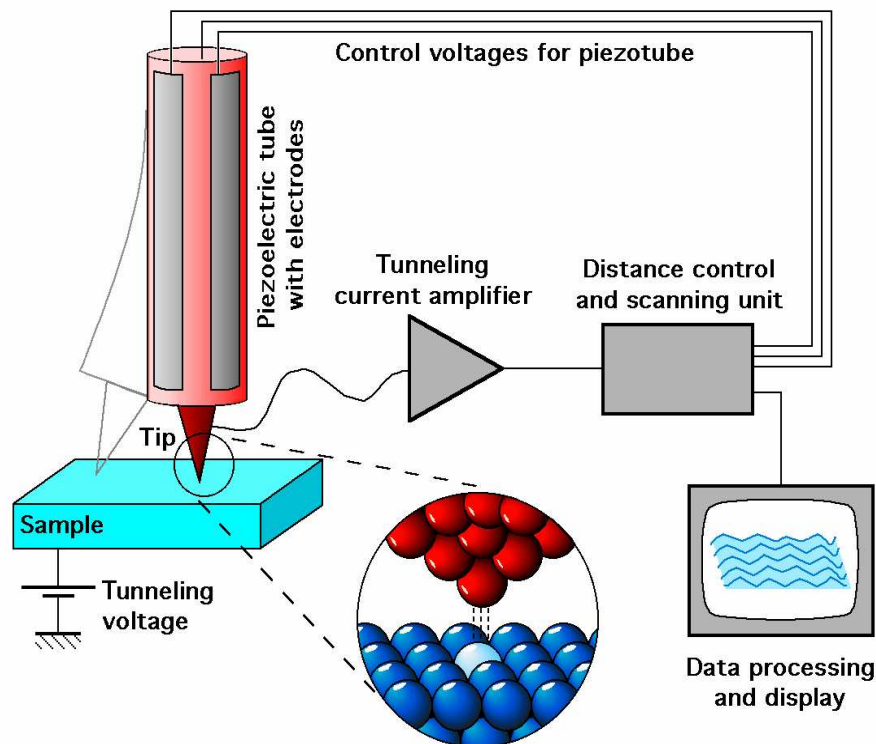


Fig. 2.1.1 STM principle of work [5].

Local proximal probes can be operated in a number of different modes. For STM there are mainly two modes, the constant-current mode and the constant-height mode. These two different operating modes are illustrated in Fig. 2.1.2:

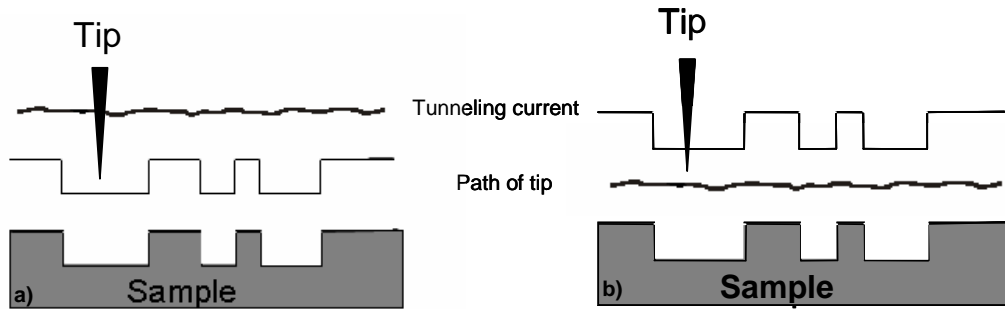


Fig. 2.1.2 Comparison between the two different modes operated STM: a) constant-current mode b) constant-height mode.

The constant-current mode, was introduced by Binnig, Rohrer and coworkers [6]. In this mode, the tip is scanned at a constant tunneling current. The current is maintained constant by continuously adjusting the vertical tip position controlled by a feedback loop. When the system detects a change of tunneling current, it adjusts the voltages by increasing or decreasing the voltage applied to the piezo scanner. The current is kept constant by adjusting the distance between tip and sample. In this mode, topographical height of surface features is obtained. A disadvantage of this method is the relatively low limit for the scanning speed. When the scanning speed is too high, the feedback loop starts to oscillate and both tip and sample can be damaged by contact between surface and tip.

In the constant-height mode, the tip can be scanned rapidly across the surface. The scan is made at nearly constant height and constant voltage. In this case, the tunnelling current is only a function of the distance between sample and STM tip. Due to the atomic roughness of the surface changes the tunnelling current are measured, which allows to obtain an image of the surface: the tunnelling current measured at each point on the sample surface then represents the data set. This is usually used for scanning atomically flat surfaces or very small areas. The scanning speed is limited by the mechanical resonances of the scanner. One of its advantages is that it can be used at high scanning speed. In comparison, the scanning speed in the constant current mode is about one image per second or even per several minutes.

2.1.1. Tunneling effect

George Gamov first proposed the tunneling effect, in 1928. The tunneling is the quantum mechanical process, in which a particle can penetrate a classically forbidden region of space. The phenomenon is called like this because the particle, in travelling from A to B , creates a sort of "tunnel" for itself, bypassing the usual route.

In classical mechanics, for an electron it is impossible to penetrate into the potential wall. In this case, the range of the particle motion is just from A to B as indicated in Fig.2.1.1.1. The situation in quantum mechanics is different in this case: there is a certain probability that the particle will be found inside the potential wall. The range of the particle motion is from A to C .

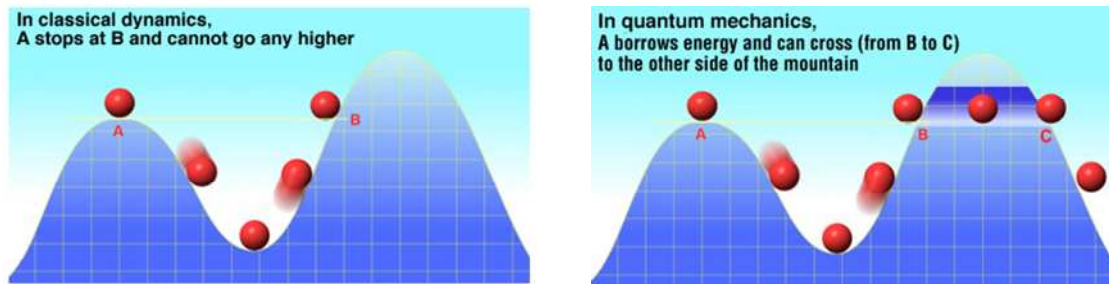


Fig. 2.1.1.1 Difference between classical dynamics and quantum mechanics [7].

In the classical Newtonian mechanics the following equation:

$$H(p, x) = T(p_x) + V(x) = W(\text{const.})$$

describes the total energy W as the sum of the kinetic energy T and the potential energy V . In a Newtonian system with one degree of freedom, consisting of a particle of mass m , restricted to motion along a fixed straight line (the coordinate x) and further described by a potential energy function $V(x)$ throughout the region $-\infty < x < +\infty$, hence to Hamiltonian function $H(p_x, x)$ and to the momentum p_x :

$$H(p_x, x) = \frac{1}{2m} p_x^2 + V(x) = W.$$

For this system, the Schrödinger time equation is closely related to the equation of classical Newtonian mechanics and is assumed to be:

$$-\frac{\hbar^2}{8\pi^2 m} \frac{\partial^2 \Psi(x,t)}{\partial x^2} + V(x) \cdot \Psi(x,t) = -\frac{\hbar}{2\pi i} \frac{\partial \Psi(x,t)}{\partial t}$$

By arbitrarily replacing p_x with the differential operator $\frac{\hbar}{2\pi i} \frac{\partial}{\partial x}$ and W with $-\frac{\hbar^2}{2\pi i} \frac{\partial}{\partial t}$ and introducing the Schrödinger wave function including the time, $\Psi(x,t)$, on which these operators can operate, the Schrödinger equation becomes:

$$H\left(\frac{\hbar}{2\pi i} \frac{\partial}{\partial x}, x\right)\Psi(x,t) = -\frac{\hbar^2}{8\pi^2 m} \frac{\partial^2 \Psi}{\partial x^2} + V\Psi = -\frac{\hbar}{2\pi i} \frac{\partial \Psi}{\partial t}$$

This is conveniently written:

$$H\Psi = W\Psi \quad [8].$$

In classical physics, an electron cannot penetrate into or across a potential barrier if its energy is smaller than the potential within the barrier.

In quantum mechanics, if the potential barrier is not infinitely thick, the result for the single potential barrier problem suggested that the wave function would still have a finite value at the other side of the barrier. This means that the particle should have a chance of passing through. With a potential barrier as shown in Fig.2.1.1.2, the solutions for Ψ in the three indicated regions are:

$$\text{Region 1} \quad \Psi = Ae^{i\alpha x} + Be^{-i\alpha x}$$

$$\text{Region 2} \quad \Psi = Ce^{\beta x} + De^{-\beta x}$$

$$\text{Region 3} \quad \Psi = A'e^{i\alpha x} + B'e^{-i\alpha x}$$

with $\alpha = (2\pi/h)(2mE)^{1/2}$ and $\beta = (2\pi/h)\sqrt{2m(V_0 - E)}$ [9].

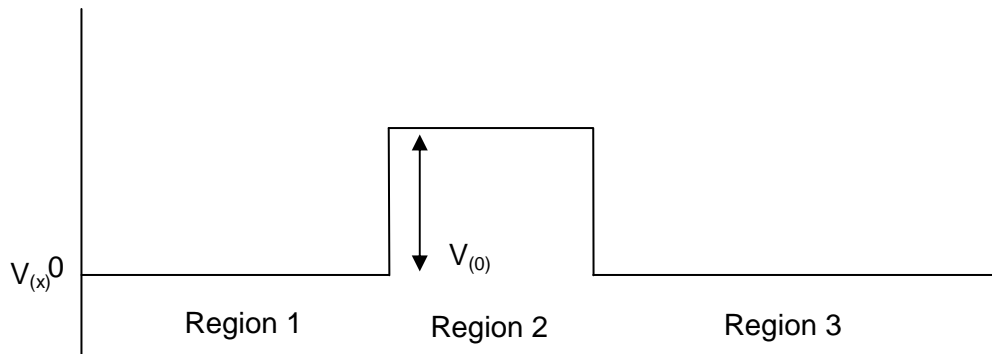


Fig. 2.1.1.2 The potential barrier.

For a rectangular barrier the solution is:

$$\Psi(d) = \Psi(0)e^{-kd}, \text{ where } k = \frac{\sqrt{2m(\Phi - E)}}{\hbar}$$

The probability to find an electron behind the barrier of the width d is

$$W(d) = |\Psi(d)|^2 = |\Psi(0)|^2 e^{-2kd} \quad [10]$$

The operation of a scanning tunneling microscope (STM) is based on the so-called tunneling current, which starts to flow when a sharp tip approaches a conducting surface at a distance of approximately one nanometer. The tip is mounted on a so-called piezoelectric scanner, which allows tiny movements by applying a voltage at its electrodes. Thereby, the electronics of the STM system control the tip position in such a way that the tunneling current and, hence, the tip-surface distance is kept constant (constant current mode), while at the same time scanning a small area of the sample surface. This vertical movement is recorded and can be displayed as an image of the surface topography. Under ideal circumstances, the individual atoms of a surface can be resolved and displayed [5].

In Fig.2.1.1.3, an energy diagram is sketched for the contact between STM tip and sample.

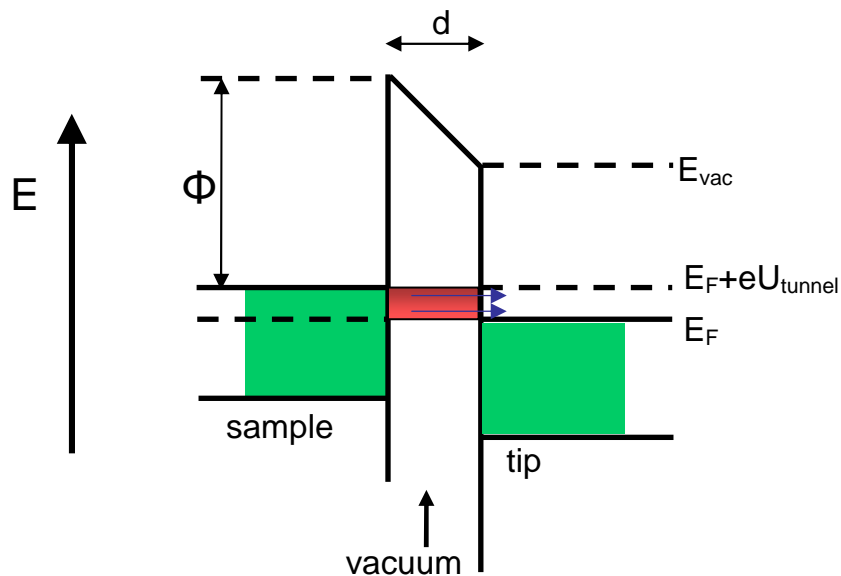


Fig. 2.1.1.3 Scheme for the contact between STM tip and sample.

Applying a voltage U_T (tunnel voltage) between tip and sample causes a difference in the Fermi energies of exactly $e \cdot U_T$. The situation of a positive potential applied to the tip is shown in Fig.2.1.1.3 and hence, electrons would tunnel from the sample to the tip. The work function of the tip and the sample are Φ_{tip} and Φ_{sample} , E_F is the Fermi energy and E_{vac} the vacuum level.

A quantum mechanical treatment of the tunnel process [11, 12] leads to the following expression for the tunneling current I_T :

$$I_T \sim U_T \exp(-A \cdot \sqrt{\Phi_T d}) \quad A = 1.025 \text{eV}^{-1/2} \text{\AA}^{-1}$$

with d being the tip – sample distance.

Typical numbers for the barrier height Φ_T are 3-4 eV for a vacuum gap. If the voltage is much smaller than the work function ($eV \ll \Phi_T$), the inverse decay length for all tunneling electrons can be simplified to

$$k \approx \frac{\sqrt{2m\Phi_T}}{\hbar}, \quad \text{where} \quad \Phi_T = \frac{1}{2}(\Phi_{\text{sample}} + \Phi_{\text{tip}})$$

The current is proportional to the probability of electrons to tunnel through the barrier

$$I \propto \sum_{E_n = E_F - eV} |\Psi_n(0)|^2 e^{-2kd}$$

The resolution of an STM decreases with increasing d , since for a large distance d between tip and surface, the tunnel current I is given by a contribution from a large number of surface atoms whereas in case of small d , I result only from a few atoms.

2.1.2. The Tersoff Hamann model

In 1985, Tersoff and Hamann presented the first theoretical description of the tunneling process in STM. “Here we developed a theory of STM, which is at once sufficiently realistic to permit quantitative comparison with experimental “images”, and sufficiently simple that the implementation is straightforward. The surface is

treated “exactly”, while the tip is modeled as a locally spherical potential well, where it approaches nearest the surface [13].

The tunneling current is found to be proportional to the surface local density of states (LDOS) at the Fermi level at the position of the tip. Keeping the gap distance constant, by measuring the current change depending on the bias voltage, one can probe the LDOS of the sample. Moreover, changing the polarity of bias voltage one can get local occupied and unoccupied states. When the sample is positively biased, electrons tunnel from the occupied states of the tip to the unoccupied states of the sample. If the sample is negatively biased, electrons tunnel from the occupied states of sample to the unoccupied states of the tip.

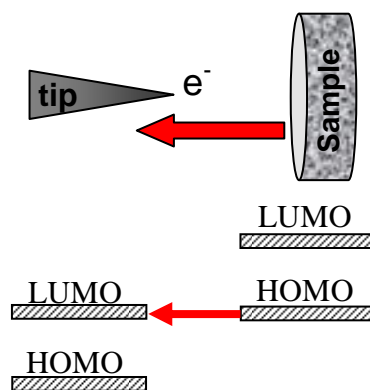


Fig. 2.1.2.1 Scheme for a positively biased sample.

With the help of the time independent perturbation theory, Tersoff and Hamann have established the state distribution for the tip and for the sample:

$$I = \frac{2\pi e}{\hbar} \sum f(E_{\mu}) [1 - f(E_{\nu} + eU)] |M_{\mu\nu}|^2 \delta(E_{\mu} - E_{\nu})$$

where $f(E)$ is the Fermi function, V is the applied voltage, $M_{\mu\nu}$ is the tunneling matrix element between states ψ_{μ} of the tip and ψ_{ν} of the surface, E_i the energy of a state in the absence of tunneling ($i = T, S$), and μ the chemical potential, k_B is the Boltzman constant, T is the temperature. The essential problem was to calculate the matrix element, and the solution is given by the Bardeen theory:

$$M_{\mu\nu} = \frac{\hbar^2}{2m} \int d\vec{S} \cdot (\psi_\mu^* \vec{\nabla} \psi_\nu - \psi_\nu \vec{\nabla} \psi_\mu^*)$$

where the integral is taking over a surface lying entirely within the vacuum barrier region between the tip and the sample and m is the free electron mass.

For small tunneling voltages and low temperature, the state distribution for the tip and for the sample is:

$$I = \frac{2\pi}{\hbar} e^2 V \sum_{TS} |M_{TS}|^2 \cdot \delta(E_T - E_F) \cdot \delta(E_T - E_F)$$

If the tip and sample are identical materials, the wave functions in the vacuum gap can be written as:

$$\psi_S(z) = \psi_S^0 \exp(-Kz)$$

$$\psi_T(z) = \psi_T^0 \exp(-K(d-z))$$

where K is the inverse decay length:

$$K = \frac{\sqrt{2m\Phi}}{\hbar}$$

with Φ , the local barrier height or average work function.

The microscopic structure of the tip is not known, and is assumed as a locally spherical potential well, where it approaches nearest to the surface. This model is presented in Fig.2.1.2.2:

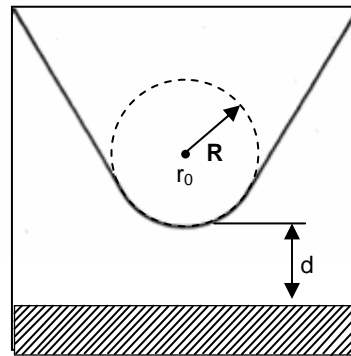


Fig. 2.1.2.2 Schematic picture of tunneling geometry.

The probe tip is assumed locally spherical with the radius of curvature R . The distance of nearest approach is d . The center of curvature of tip is labeled \vec{r}_0 .

In this case, the resulting matrix element is:

$$M_{TS} = -\frac{\hbar^2}{2m} 4\pi \frac{(K \text{Re}^{KR})}{(K\Omega^{1/2})} \psi_S(r_0)$$

where r_0 is the position of the center of the curvature of the tip. The tunneling current is:

$$I = \frac{32\pi^3 e^2 V}{\hbar} \Phi^2 D_T(E_F) R^2 K^{-4} \cdot e^{2Kr} \sum_S |\psi_S(r_0)|^2 \delta(E_S - E_F)$$

where $D_T(E_F)$ is the tip density of states per unit volume.

At low voltages, the tunneling current is proportional with the $\rho(\vec{r}, E_F)$, the local density of states (at E_F) at the point \vec{r} and with the voltage itself. In this case, the Ohm laws are applied and so, when the sample is biased positive, electrons from occupied states of the tip tunnel to the unoccupied states of the sample. The tunneling current I is also proportional with e^{-2Kd} and by differentiating the logarithmic of the tunneling current gives the local barrier height, i.e., Φ becomes:

$$\Phi \propto \left(\frac{\partial \ln I}{\partial d} \right)^2$$

The local barrier height can be directly measured through the d variation (d is the distance between sample and tip) and this is achieved with current modulation.

2.1.3. STM image processing

To control the STM-tip, the electronics and all measurements processes, the “SPM-32” software, version 5.06 from RHK Technology, Inc. was used. The STM data were evaluated with the help of the WSxM (Windows Scanning X (Force, Tunneling, Near Optical, ...) Microscope) which is a powerful and user-friendly Windows application for Data Acquisition and Processing in Scanning Probe Microscopy (SPM)) program developed by Nanotec Electronica SL™ (Nanotec). The WSxM Scanning Probe Microscopy Software is divided into two well defined parts.

The part for data processing is used for data evaluation. The program allows performing very general processes such as 3D rendering, pseudo-color image representation, Fourier and roughness analysis, cross section profiles and many others more. The program supports most of the data files used in SPM (including the *.sm2). The most common files obtained with a SPM program are topography maps. First, there is a smooth filter applied for the topographical images in order to eliminate the high frequency components of the image. Second, an equalize filter is used. This filter allows one to select a range of heights to enhance the contrast of the image. The heights are given along the x- axis, and the numbers of occurrences for each height are given along the y-axis. Another flatten filter is used because the SPM images may contain a low frequency noise. This noise can be observed as an irregular distribution of the scan height along the Y direction. In order to remove this noise a flatten filter is usually the best choice. Flatten works by subtracting a function to each scan in the unprocessed image. The simplest function is a constant: the average of each line. A Fast Fourier Transform is also performed on the images by applying a 2D-FFT Filter.

Depending on the original topographical image, the profile curve (PRF curve) represents the profile of the sample. The PFR curves provide information about a 1D path over the 2D image.

The program offers the possibility to create a new layer on the image, showing a 2D lattice (usually to represent an atomic pattern). There are also presetted lattices. The default lattice is the hexagonal lattice, made up by circles whose centers follow a hexagonal pattern. There is an alternative for the topographical image to display it as a 3D image.

For extra support information, “The Scanning Probe Processor, SPIPTM”, version 3.3.9.2 from 14 April 2005, for the Omicron Matrix SPM Control System developed by Image Metrology and “XPMPPro”, version 1.0.0.0 from RHK Technology was used.

2.2. Quadrupol mass spectrometry (QMS)

As John B. Fenn, the originator of electrospray ionization for biomolecules and Nobel Laureate in Chemistry in 2002, said “Mass spectrometry is the art of “weighing” individual atoms and molecules to determine their masses or molecular weights” [14]. Mass spectrometry is a powerful analytical technique used to describe the structure of an entire molecule, to identify unknown compounds, to quantify known compounds and to elucidate the chemical properties of molecules.

To determine the mass of a molecule, the mass spectrometers measure the mass-to-charge ratio (m/z) of its ion. Ions are generated from a neutral species and are electrostatically directed into a mass analyzer, where they are separated according to m/z and finally detected. The result is a spectrum that provides molecular mass and even structural information.

Mass spectrometry is used to measure the mass-to-charge ratio of ions. The ions are accelerated in an electrostatic field. The mass separations occurred dynamic or static. The principle of a dynamic mass separation is that the speed reached in an electrostatic field is proportional to the ions charge/mass ratio [15]:

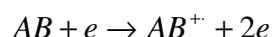
$$v \approx \sqrt{\frac{e}{m}}, \text{ with } e\text{-ion charge and } m\text{-ion mass}$$

This equation expresses that for the same ion charge, the heavy ions are registered later by a recording device. Recorded is a mass spectrum that is representing the masses of sample components.

The device that measures the mass-to-charge ratio of ion is called a mass spectrometer. The measurement is achieved by ionizing the sample molecules and separating ions of differing masses. By measuring the intensity of the ion flux is recorded their relative abundance. A typical mass spectrometer comprises three parts: an ion source, a mass analyzer, and a detector system.

The ion source is the part that ionizes the sample (the material under analysis). Only the charged parts are transported by magnetic or electric fields to the analyzer. One way to create the charged particle is the electron impact ionization. An electron beam bombards the sample molecules. An electron that strikes a molecule may

contain enough energy to remove another electron from that molecule. One molecule would follow the reaction in the ionizing region:



where AB is the sample molecule, and the symbol $^+$ indicates that a radical cation was formed.

The mass analyzer is the second component of a mass spectrometer. Molecular ions and fragment ions are accelerated and thereafter enter the mass spectrometer. A mass analyzer can separate the ion according to their mass-to-charge ratio by a static magnetic field or by an oscillating electrical quadrupole field.

The third part (the final one) of a mass spectrometer is the detector. The detector records the charge induced or current produced when an ion hits its surface.

The mass analyzer sorts the ions according to the mass/charge ratio and the detector records the abundance of each mass/charge ratio, producing a mass spectrum. There are many types of mass spectrometers and one type of mass analyzer is the quadrupole mass spectrometer. Fig 2.2.2 shows the scheme of a quadrupole mass filter.

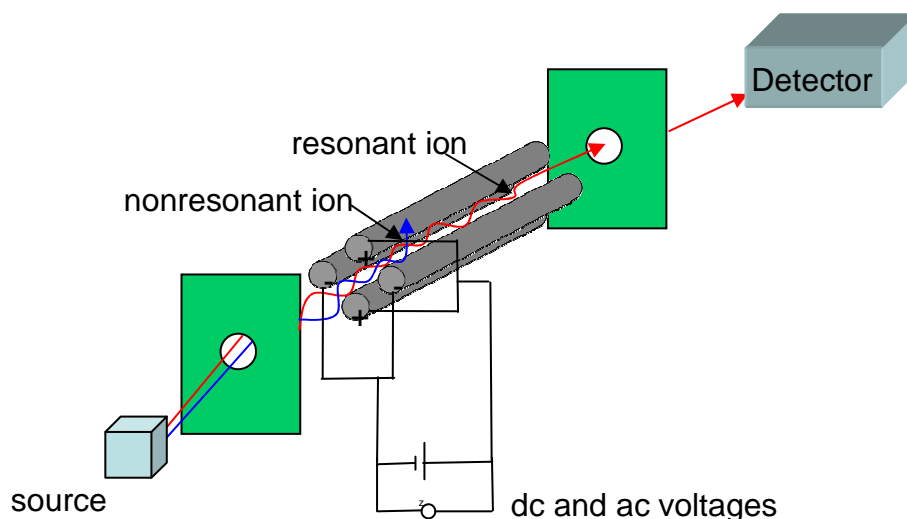


Fig. 2.2.2 Schematic of a quadrupole mass filter.

A quadrupole mass analyzer acts as a mass selective filter. A quadrupole mass filter is made up of four metal rods connected to a DC voltage. Two positive charged rods and two negative charged rods are electrically connected. A radio frequency voltage is applied between these two pairs of rods. A DC voltage is superimposed on the radio frequency voltage. All ions are travelling down the quadrupole in between

the rods, but only the ions of a certain mass / charge ratio, will reach the detector for a given ratio of voltage. Other ions will collide with the rods because they have unstable trajectories.

2.3. Low energy electron diffraction (LEED)

Low energy electron diffraction is a technique to determine the surface structure. The surface crystallographic structure can be determined by bombarding the surface with low energy electrons (approx. 10-200 eV) and by observing diffracted electrons as spots on a phosphor screen. The structural information given by a LEED pattern is deduced from the position and the intensity of the diffraction spots as well as from the spot profiles. The diffraction spots will move as the energy of the incident electrons changes. The intensity of the spots as a function of incident electron energy contains much information about surface structure. The sample must be a single crystal with a well-ordered surface structure in order to generate a back-scattered electron diffraction pattern. The low energy electron diffraction technique can be used in two ways: qualitatively and quantitatively. In Fig. 2.3.1, a typical experimental set-up is shown:

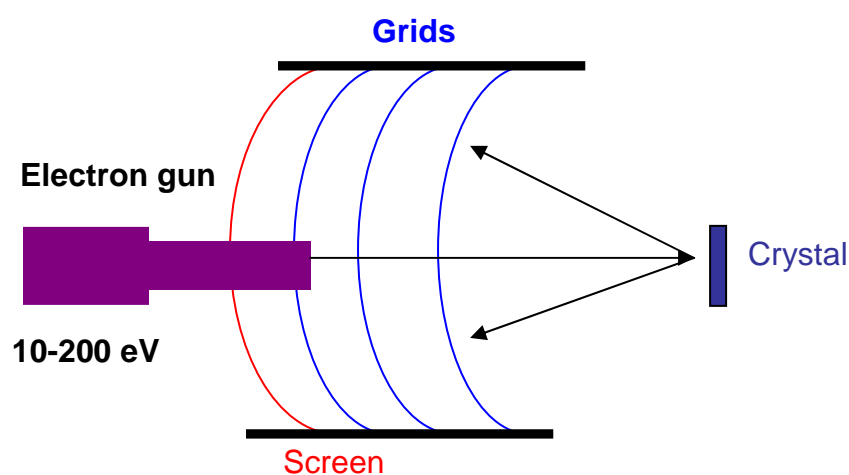


Fig. 2.3.1 Experimental set-up for LEED.

Only the elastic scattered electrons contribute to the diffraction pattern. The secondary electrons, the electrons with lower energy, are removed by energy filtering grids situated in front of a fluorescent screen.

Davisson and Germer [16] published the results of the first LEED experiment in 1927. They studied a Ni single crystal surface. L. de Broglie had postulated the wave nature of matter in 1924. The electron de Broglie wavelength for kinetic energies of around 100 eV fits very well the typical atomic distances in a crystal:

$$\lambda = h / p , \text{ where } p \text{ is the electron momentum,}$$

this is a necessary condition to observe the diffraction effects associated with atomic structure. A simple approach to imagine the scattering of electrons by atoms in the first layer of a solid is to consider a one-dimensional chain of atoms with the electron beam incident at the right angle to the chain. The chain of atoms have an atomic separation a . Fig.2.3.2 would be representing the solid in cross-section with the electron beam incident normal to the surface from the vacuum above:

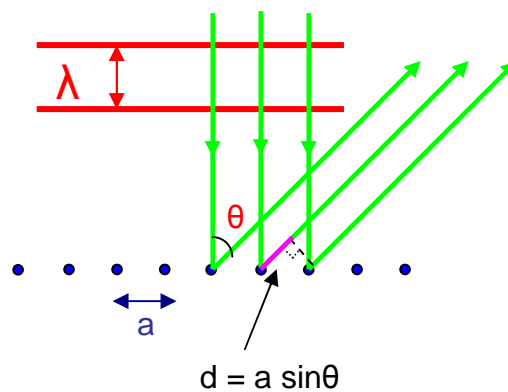


Fig. 2.3.2 The solid in cross-section with the electron beam incident normal to the surface from the vacuum above.

Taking into account the backscattering of a wave front from two adjacent atoms to the surface normal, with a well-defined angle, θ , than there is a difference d in the distance the radiation has to travel from the scattering center to a distant detector. This difference is illustrated in Fig.2.3.2. This difference must be equal to an integral number of wavelengths for constructive interference to occur when the scattered beams eventually meet and interfere at the detector:

$$d = a \sin \theta = n \cdot \lambda$$

where λ - wavelength and n – integer ($\dots-1,0,1,2,\dots$).

The diffracted intensity varies between zero and a maximum value for a periodic array of scatterers. The diffracted intensity is significant only when the condition $a \sin \theta = n \cdot \lambda$ is satisfied exactly.

A periodic two-dimensional surface structure can be classified into lattice types similar to the three-dimensional crystal structure. The surface region has no periodicity in the direction normal to the surface, but the surface presents a finite thickness. The three-dimensional structure presented 14 Bravais lattices. For the two-dimensional surface structure there are five types of Bravais lattices: square, primitive rectangular, centered rectangular, hexagonal, and oblique [17]. Identical lattice positions are connected by translation vectors:

$$\vec{R}_{hk} = h' \cdot \vec{a}_1 + k' \cdot \vec{a}_2 \quad (h', k' = \text{integers}).$$

The periodicity of the surface is related to the substrate lattice. The unit vectors, \vec{a}_1 and \vec{a}_2 , describes the periodicity of the surface. The substrate lattice is defined as that plane parallel to the surface below which the three-dimensional periodicity is found. The surface structure is defined as the region above the substrate surface in which the lateral periodicity is different and/or in which no periodicity normal to surface is found [18]. The index is chosen according to the usual conventions of x-ray crystallography so that $|a_1| \leq |a_2|$. For most clean metal surfaces, the surface structure is identical with the substrate structure. The classification of surface structures mostly follows the nomenclature proposed by Wood [19]. This nomenclature is simple, but it cannot describe all types of periodic structure adequately. Another description, in this case an universal one, has been proposed by Park and Madden [20]. The surface lattice (b_1, b_2) and the unit cell of substrate (a_1, a_2) are related by the transformation:

$$b_1 = m_{11}a_1 + m_{12}a_2$$

$$b_2 = m_{21}a_1 + m_{22}a_2$$

or, in matrix notation: $\mathbf{b} = \mathcal{M} \cdot \mathbf{a}$.

\mathcal{M} is the transformation matrix and has the form:

$$\mathcal{M} = \begin{pmatrix} m_{11} & m_{12} \\ m_{21} & m_{22} \end{pmatrix}$$

The areas for the unit cell of substrate and surface lattice are given by the next equation:

$$A = |a_1 \times a_2|$$

$$B = |b_1 \times b_2|$$

The relationship between A and B is given by:

$$B = (m_{11}m_{22} - m_{12}m_{21}) \cdot A = A \cdot \det \mathcal{M}$$

The periodic surface structure can be divided in three types based on their relation to the corresponding substrate lattice: simple structure, incommensurate with a coincidence lattice and, incoherent structure.

Making an analogy between the three-dimensional and two-dimensional structure, and knowing that the planes within the lattice may be defined by the Miller indices (h', k', l') , the lattice for a two-dimensional structure may be arranged in rows and classified by the (h', k') indices. The diffraction spots of a LEED pattern may be attributed to the scattering at rows, and so the indices can be used to describe a LEED pattern. The distance $d_{h'k'}$ between two neighboring rows of direction $[h' k']$ is given by the relation:

$$\frac{1}{d_{h'k'}^2} = \frac{h'^2}{b_1^2 \sin^2 \gamma} + \frac{k'^2}{b_2^2 \sin^2 \gamma} - \frac{2h'k' \cos \gamma}{b_1 b_2 \sin^2 \gamma}$$

where the γ is the angle between the axes of the unit cell with the base vector lengths b_1 and b_2 . For a rectangular unit cell, the distance becomes:

$$\frac{1}{d_{h'k'}^2} = \left(\frac{h'}{b_1}\right)^2 + \left(\frac{k'}{b_2}\right)^2.$$

2.4. Ultraviolet photoelectron spectroscopy (UPS)

Photoelectron spectroscopy utilizes photo-ionization and energy-dispersive analysis of the emitted photoelectrons to study the composition and electronic state of the surface region of a sample. According to the source of exciting radiation, the technique has been subdivided into X-ray Photoelectron Spectroscopy (using soft x-ray (100-2000 eV) radiation to examine core-levels) and Ultraviolet Photoelectron Spectroscopy, using vacuum UV (10-100 eV) radiation to examine valence levels.

In X-ray Photoelectron Spectroscopy (XPS) the photon is absorbed by an atom in a molecule or solid, leading to ionization and the emission of a core (inner shell) electron. By contrast, in UPS, the photon interacts with valence levels of the molecule or solid, leading to ionization by removal of one of these valence electrons.

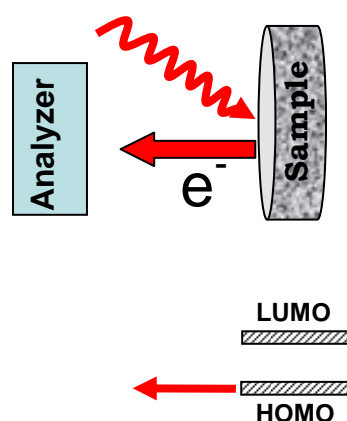


Fig.2.4.1 Scheme for the UPS experiment.

Fig.2.4.1 illustrates the UPS experiment for emission of electrons from the HOMO density of states. In UPS, the source of radiation is normally a noble gas discharge lamp, frequently a He-discharge lamp emitting He-I radiation of energy 21.2 eV. The UV light penetrates several micrometers (1–3 μm) into the sample producing photoelectrons throughout the penetration depth of the X-rays. The energies of the emitted photoelectrons are characteristic of their original electronic states, which include vibrational studies, rotational studies, and molecular orbital studies, bonding state information, configuration interactions and the polarization

effects of the adjacent atoms. Such radiation is only capable of ionizing electrons from the outermost levels of atoms - the valence levels. The advantage of using such UV radiation over x-rays is the very narrow line width of the radiation and the high flux of photons available from simple discharge sources.

3. Experimental set-up

All experiments were performed in UHV chambers with vacuum in the 10^{-10} mbar range. The STM-UHV system consists of two different chambers, preparation chamber and analyzes chamber (or main chamber). The main chamber houses the STM instrument. The STM chamber is connected with a load-lock system that enables the tip and sample transfer. Wobble sticks enable also the tip and sample handling. For sample preparation, an ion gun for Ar^+ sputtering, a metal evaporator, a LEED system for surface structure analysis and a quadrupole mass spectrometer for residual gas analysis are used. There are also facilities for transfer between the two chambers.

3.1. Main chamber

The STM system is a Variable Temperature Ultrahigh Vacuum Scanning Tunneling Microscope from RHK Technology. The system offers the opportunity to use a UHV STM under variable temperature operation. This subsystem takes advantage of the inherent stability of the “Beetle” design [21]. The STM head design had a symmetric and compact structure with a very high resonance frequency and self-compensating thermal properties. The vacuum chamber is designed with multiple ports targeted at the tip/sample interface. The operator has an excellent view of the sample and internal operation. Fig.3.1.1 shows a schematic drawing of the UHV 300 STM system with the chamber partly cut-off for clarification. In the image, the following items can be identified: UHV chamber, scan head manipulator assembly, heating/cooling sample stage, sample holders, tip holders, wobble stick, storage elevator, and a fast entry load-lock. This UHV system utilizes an air leg-supported steel frame and allows the sample holder to be transferred between the chambers via a magnetic transfer arm.

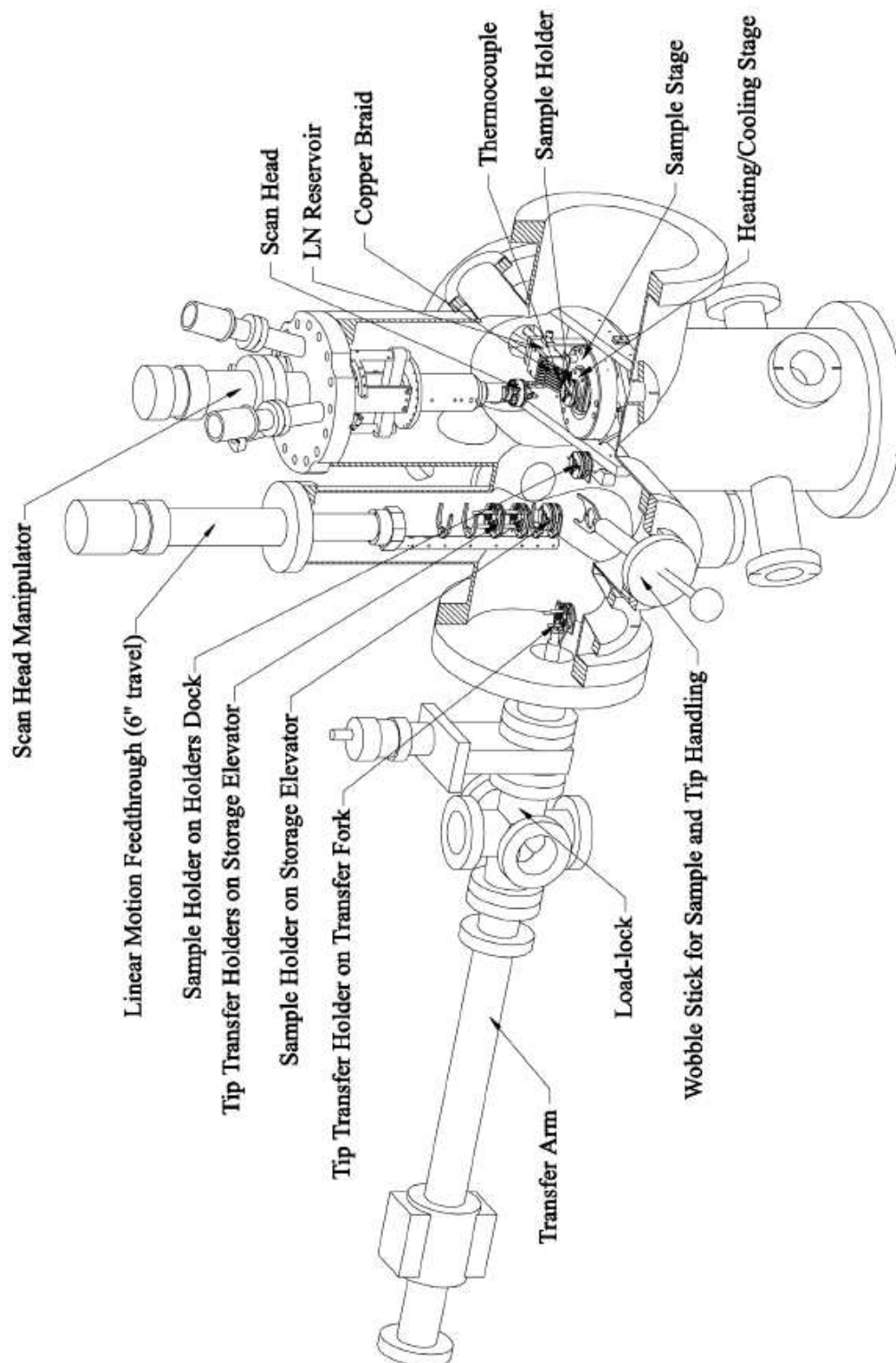


Fig. 3.1.1 Schematic drawing: the UHV 300 STM system [22].

Offering the possibility to view the sample and internal operation, the operator can observe the tip exchange process, the process of taking sample/tip holders in or out of the storage elevator and the possibility to see clearly the storage elevator, the sample/tip transfer fork and the auxiliary heater port.

The STM scan head is based on “Beetle” type scan head design. The STM scan head had modifications made for enhanced stability, and to accommodate the in-situ tip exchange mechanism. The scan head consists of four identical piezoelectric tubes and a “Mexican hat”-shaped body.

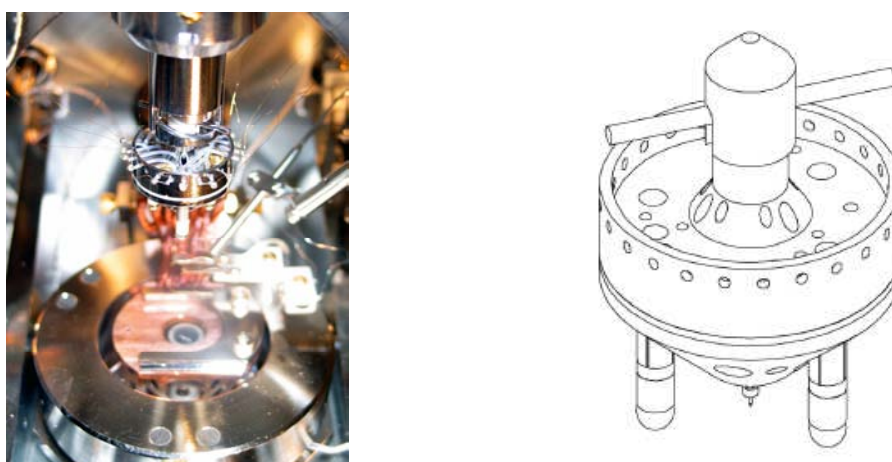


Fig. 3.1.2 Scan head top view (photo and schematic draw [22]).

The “legs” of the scan head are represented in three outer tubes, which are mounted 120 degrees apart on a circle. The scanning tube, the fourth tube, is located in the center of the head. In addition, this tube holds the tip. Sapphire balls are attached to the end of each of the legs with an intermediate ceramic adapter. The scan head is connected to the control electronics by Kapton-insulated copper wires. The wires realized the connection to the piezo tubes.

The sample holder has a double grooved copper body and a helical molybdenum top ramp. The double grooves in the sample holder body are to hold the sample into the sample stage and for transferring the sample holder between the various stages in the STM system. The three legs of the scan head are landing on one of the three segments of the helical ramp when the head is placed down to the sample holder. The motion of the head (rotation or translation) is realized by applying voltages pulses to the four segments of the electrodes on each leg. The voltages pulses

cause the sapphire balls to stick or slip against the ramp surface, generating a motion that causes the approaches or retracts of the tip.

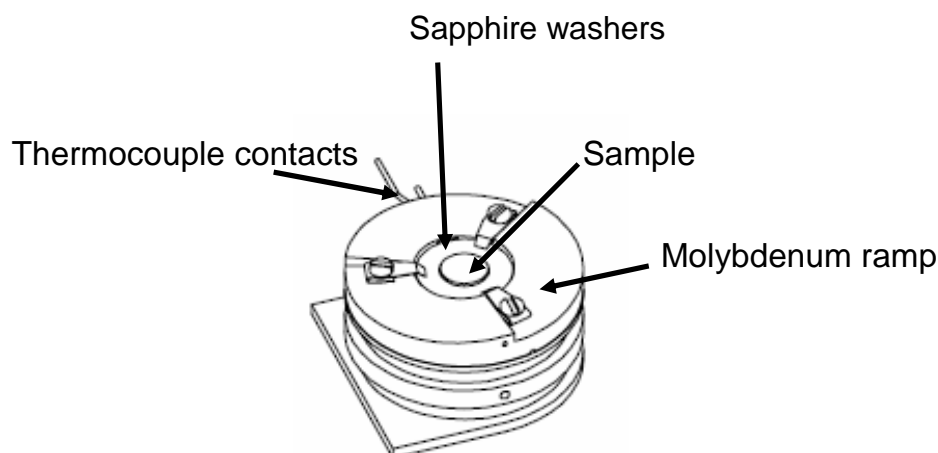


Fig. 3.1.3 Top loading sample holder [22].

The sample is a single crystal disc that can be sandwiched between the two sapphire washers. In this way, the sample can be heated by electron bombardment. The sample holder cannot be heated too much, because of the sapphire washers. The sample holder had also a built-in thermocouple to measure the sample temperature.

The scan head manipulator provides all the necessary mechanical and electrical feedthrough for connection to the scan head. By lowering the head onto the sample holder, the head will be placed in the same position every time. The position with the tip pointing to the center of the sample guarantees that the tip of a correct length will not crash into the sample.

The tip holder is formed up of a small aluminum body with a stainless steel tube press fit into its center. The tip transfer / exchange holder is used to hold / carry the tip holder. With this device, it is possible to exchange the tip in-situ. The body of the tip transfer holder has the same design as the sample holder to assure that it is always placed at the same position and orientation on the sample stage.

The sample stage is a variable temperature stage. It consists of a heavy stainless steel ring with a thermally isolated copper center stage. The sample stage contains the liquid nitrogen feedthrough connected to a flow cryostat and a tungsten filament as a heater located underneath the sample. There are also electrical feedthroughs for the sample heater, thermocouple feedthroughs to measure the

sample, sample stage and cryostat temperature. The stage is also designed with an isolated BNC feedthrough for the sample bias and a rotary motion feedthrough for moving the heater up and down.

To enable in-situ sample and tip exchange the device is scheduled with a storage elevator to store the sample holder and tip transfer holder. In addition, to realize an in-situ sample transfer or a tip change, the wobble stick with a fork is used. Fig.3.1.4 presents our experimental device.

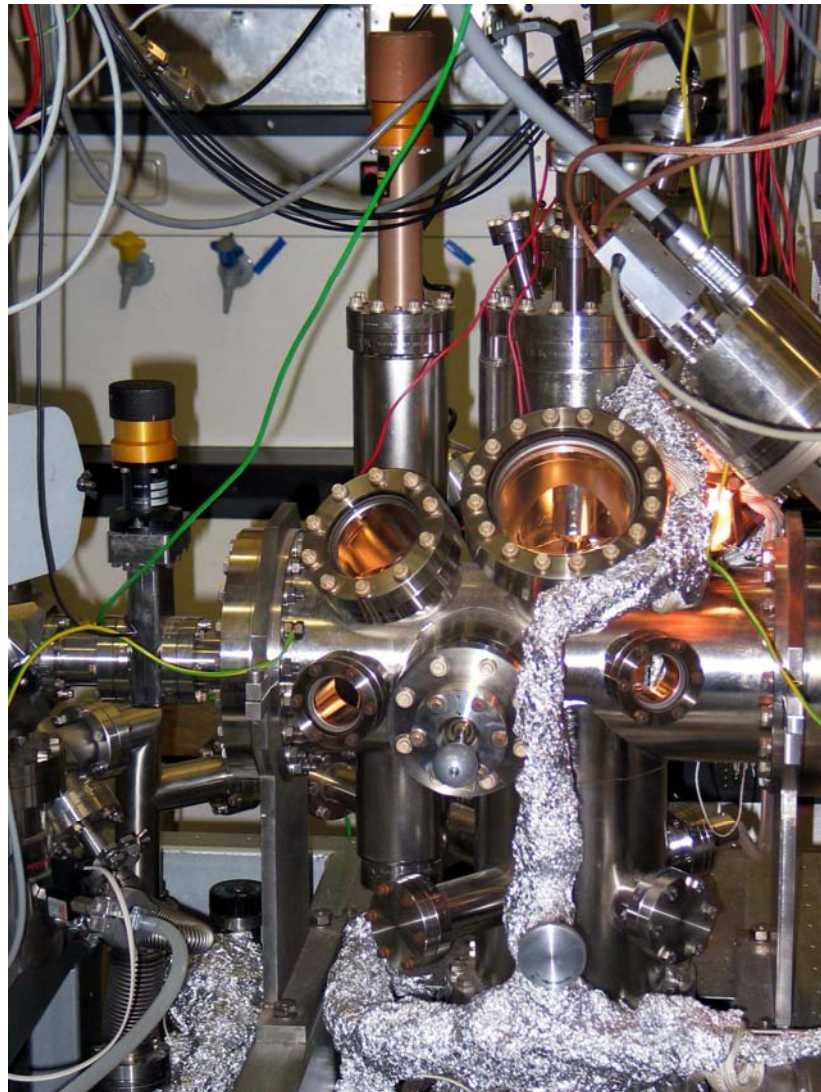


Fig. 3.1.4 *STM chamber.*

3.2. Preparation chamber

The preparation chamber is described within the dissertation of Dr. Reinhard Peter Lindner [23]. This chamber features the necessary equipment to generate and to conserve the UHV. The basic pressure is in the range of 10^{-10} mbar. The preparation chamber is equipped with the following instruments: LEED optics, Quadrupole mass spectrometers, sputter gun, Ti-sublimation pump, and two evaporators. For the metal deposition an Omicrom EFM 3 electron beam evaporator was integrated, and for porphyrins a home-built evaporator. For the sample transfer, the chamber housed a Wobble stick and a transfer arm makes the sample transfer between the STM and preparation chambers. Fig.3.2.1 shows the preparation chamber with all the utilities.

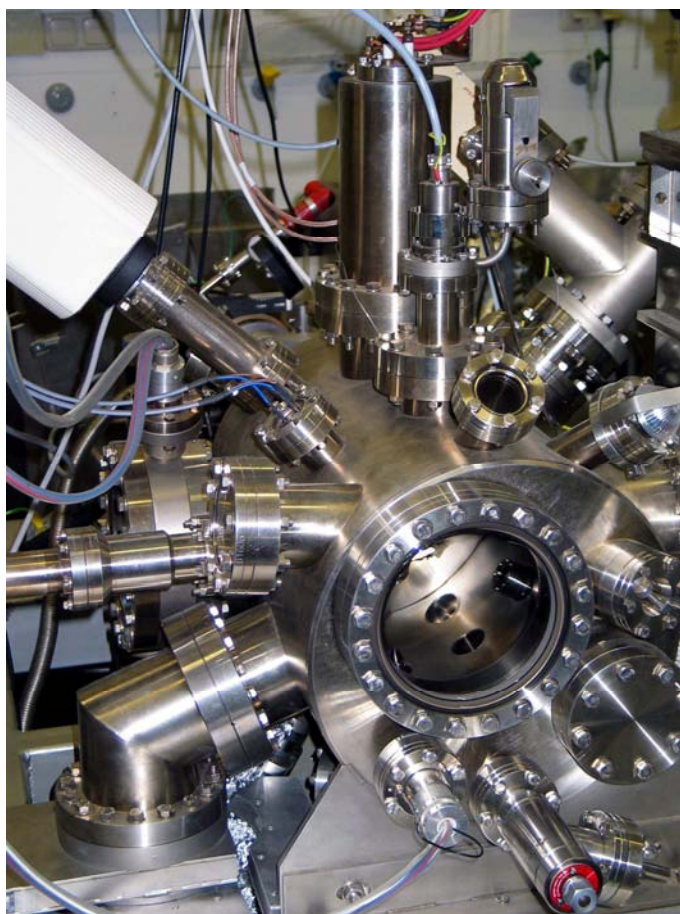


Fig. 3.2.1 Preparation chamber.

For the porphyrin molecules deposition, a home-built Knudsen cell evaporator is used. The evaporator provides a stable high temperature furnace for the controlled

deposition of molecules. This is an ideal tool for reproducibly depositing thin films of material in a controlled manner from submonolayer to monolayer. For the temperature measurements, a type-K thermoelement is mounted. A quartz-glass crucible with the evaporant material is covered by a metallic block, and the heating elements are wound around on the metallic block. The quartz-glass crucible and this metallic block are shielded by another metallic block. The block is protected from a shutter that can be manipulated from a rotary feedthrough. In this way, by opening the shutter the evaporated molecules can reach the sample surface. Fig.3.2.2. shows the home built evaporator.



Fig. 3.2.2 The home-built Knudsen cell evaporator.

3.3. Sample preparation

As substrate the Ag(111) surface was chosen, since for the noble metals with a small density of state near the Fermi edge, no significant chemical bonding of the molecule to the surface can be expected. This bond can allow sufficient lateral mobility for the formation of long-range ordered structures. The self-assembly of organic molecules is interesting for many physical and chemical processes. The assembly processes are determined by the interaction between substrate and adsorbate and intermolecular interaction. The assembly processes are of great relevance towards the fabrication of nanosized structures and the porphyrin molecules are interesting for fundamental science and for applications.

3.3.1. Ag (111) preparation

Prior to the molecule deposition, the sample must be clean. As the substrate, an Ag (111) crystal was used. The crystal was cleaned at room temperature by repeated cycles of sputtering and annealing. The Ar partial pressure was $4 - 5 \times 10^{-5}$ mbar and the energy of the Ar^+ - ions was 500 eV. Typical sputtering times range was from 15 to 45 min. After every sputter cycle, the crystal was heated up to 850 K and kept at this temperature for 10 min. The sample was heated by means of a tungsten filament. The temperature of the system was measured by means of thermocouples. The crystal must cool down to room temperature before the film deposition. The cooling down requires a large time interval (only 40 K / min until 400 K are reached). There are two ways to reach room temperature for the sample:

- cooling down with ice cooled air using the manipulator cooling system.
- letting the sample to cool down without any other external intervention.

The cleaning procedure consists of two cycles of sputtering and annealing. There are also differences between these cycles: the time for the first sputtering is 45 minutes and after annealing the sample must not reach room temperature, and by the second sputtering, the time becomes shorter - only 15 minutes. After the second annealing, it is recommended for the sample to reach the room temperature for a proper film deposition.

3.3.2. Porphyrin deposition

Thermal sublimation in vacuum is one of the applied methods to prepare films from these types of molecules, for both fundamental research and practical applications. The material vapor finally condenses in form of a thin film on the substrate surface. Usually, low pressures are used. With this method, it is possible to obtain films with high purity in a controlled way. This method is also compatible with the techniques used in the Surface Science. As alternative techniques are the liquid phase depositions.

For the deposition, the crystal was cleaned and during evaporation, it had been held at room temperature. The optimum evaporation temperature was determined by QMS measurements. The mass spectra were recorded at different temperatures with a quadrupol mass spectrometer. In Fig.3.3.2.2 an example of a representative mass spectrum for the 2H-TPP is given.

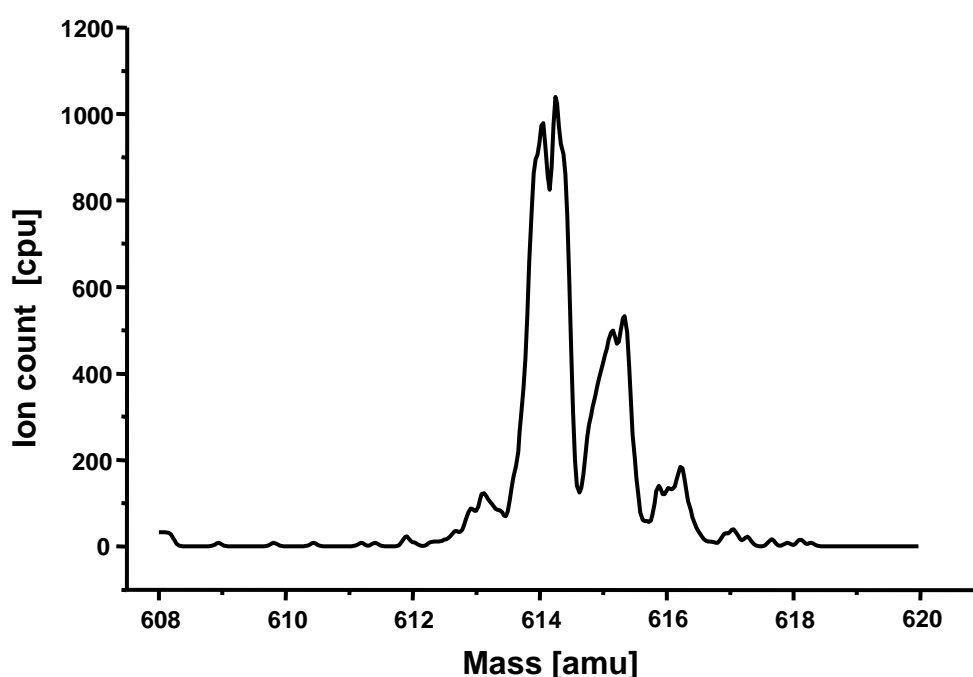


Fig. 3.3.2.2 QMS spectrum for porphyrins compounds.

The most significant peaks corresponding to the mass of the molecules are observed at the parent mass of 614 and 615 amu for 2H-TPP. The first peak corresponds to a signal that can be expected more for the ionized molecule. For the signals with 615 and higher masses, the isotopes effects are responsible. If the ionized molecule contained ^2H -, ^{13}C - or ^{15}N - atoms, the molecule is heavier with equal lasting load [24]. The evaporation temperature was established to 330°C and was then used for all the experiments. The time of deposition had to be about 20 minutes in order to obtain a monolayer. The porphyrins (2H-TPP, Co-TPP and Zn-TPP) are purchased from the Porphyrin System GbR, and used as supplied. Dr. Norbert Jux synthesized the Co-TTBPP. For evaporation, a home-built evaporator with a quartz-glass crucible and K-type thermocouple was used. Before sublimation, the evaporant was out-gassed

at 340° C. The sample was positioned so that the evaporated molecules could reach the sample surface. The molecules were heated by heating the evaporator, using a variable voltage supply (DC power supply). For the temperature measurement, a thermo element was used. Before opening the shutter, the temperature must be constant for two or three minutes. When the temperature remains constant, the shutter can be opened and a certain quantity of molecules can hit the surface.

4. Theoretical background and Literature overview

4.1. Short description of porphyrins

The name “porphyrins” has its origin in the classical Greek language. In the time of ancient Greece, the word “porphura” was used to describe the color purple. This reflects about one remarkable feature of porphyrins: their intense color [25].

In the Oxford English Dictionary [26], the porphyrins are defined as “a large class of deeply coloured red or purple, fluorescent crystalline pigments, of natural or synthetic origin, having in common a substituted aromatic macrocyclic ring consisting of four pyrrole-type residues, linked together by four methane bridging groups”. A new chemical definition is found in the Dictionary of the English language [27] where porphyrins are “Any of various organic compounds containing four pyrrole rings, occurring universally in protoplasm, and functioning as a metal-binding cofactor in hemoglobin, chlorophyll, and certain enzymes”.

Hans Fisher brought up the first system of nomenclature for porphyrins. There are many porphyrins with substituents on all eight positions of the four pyrrole fragments. He called the basic, unsubstituted macrocyclic ring, porphine. Fischer’s semi-trivial nomenclature also included a numbering system for the macrocyclic ring. Each position on the pyrrole fragments where a substituent could link to, was called a β -carbon and was given a number 1 to 8. The pyrrole position next to each nitrogen atom were called α - carbons and remained unnumbered. The bridging carbon atoms were called meso-carbons and were given a Greek lower case letter, α - δ . With the increasing of the complexity of porphyrin derivate, Fischer’s system becomes unwieldy and even contradictory and a new nomenclature is needed.

A more systematic nomenclature, the IUPAC nomenclature, was introduced in 1979 and finalized in 1987. This nomenclature numbered all the atoms (including the nitrogen atoms, see in Fig.4.1.1) in the macrocycle, cut down on the number of trivial names used, and also managed to incorporate structural information into the name. The parent macrocycle is called porphyrin and the numbering of the substituted porphyrin depends on where on the macrocycle the principle groups are present.

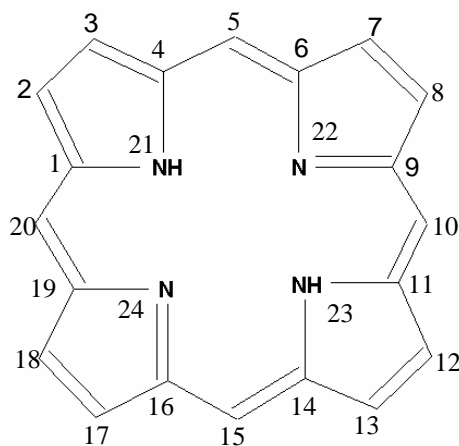


Fig. 4.1.1 All-numbered IUPAC systematic nomenclature on porphyrin macrocycle [25].

Porphyrins are “a large class of deeply coloured red or purple, fluorescent crystalline pigments” [26]. These pigments are based, as it was already said, on a macrocyclic ring of carbon and nitrogen atoms. Two important representatives of this class are the iron-containing porphyrin found as heme (of hemoglobin) and the magnesium-containing reduced porphyrin (or chlorophyll) found in chlorophyll. The iron-containing porphyrin follows the rule that these pigments are red. The hemoglobin is the iron-containing oxygen-transport metalloprotein in the red cells of the blood in mammals and other animals. In contrast, even when they are from the same class of molecules, the magnesium-containing reduced porphyrin is green. Chlorophyll (chloros = green and phyllon = leaf) is a photosynthetic pigment found in most plants, algae, and cyanobacteria. Hence, the green color of chlorophyll-containing tissues like plant leaves is due to the fact that chlorophyll absorbs most in the blue and red and poorly in the green portion of the electromagnetic spectrum.

One of the interesting things about porphyrins is how small variations on the basic structural theme of tetrapyrrolic macrocycle, lead to a wide diversity of biochemical functions. Porphyrins represent an important class of the organic molecules. Organic molecules are the building blocks of living systems and of novel materials and devices. The organization of these molecules on solid surfaces is considered as a key in the realization of molecular device architectures. The molecules lie in the size regime between the small molecules (containing only few

atoms) and the larger biological molecules. The small molecules are the traditional target of surface science studies [28].

Since the porphyrins are of great importance in different research areas they are intensively studied in the last years. For example, porphyrin thin films are applied as conductive gas sensors [29], as photovoltaic cells [30], as organic light emitting diodes [31] or electro-optical data storage [32]. From porphyrin-derived materials there are also designed rigid or semi-rigid molecular wires [33].

Porphyrins with a central metal atom, so called metalloporphyrins, can also act as catalysts. Metalloporphyrins can undergo reversible redox reactions in which the site of electron transfer may be localized on the porphyrin ring, or on the central metal ion. Both reaction types are important in natural processes [34].

The porphyrin molecules investigated in this work are sketched in Fig.4.1.2. The interest was focused on the metal-free porphyrin and on the molecules containing a central Zn and Co atom. Different ligands are used to tune the metal-substrate distance, as shown for the metal porphyrin in Fig.4.1.2 where the distance is tuned by changing the phenyl groups with di-tert-butyl groups.

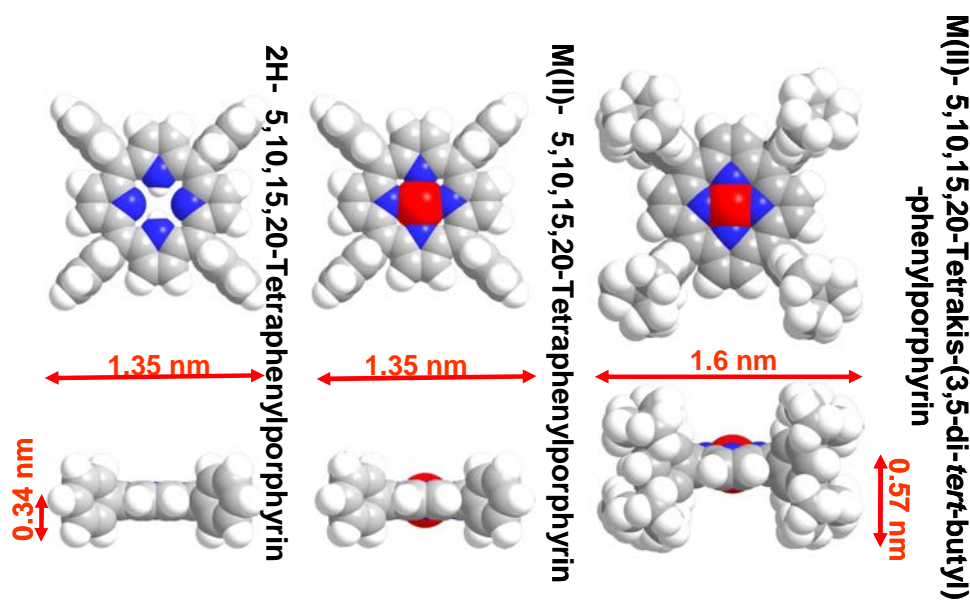


Fig.4.1.2 Sketches for porphyrins with different substituents.

4.2. Porphyrins on surfaces

Scanning tunneling microscopy (STM) has emerged as an extraordinary method to yield a direct three-dimensional real-space image of surfaces with atomic resolution. The surface may be metallic, semiconducting, and eventually covered with adsorbed or chemisorbed atoms and molecules. Formation and characterization of ordered layers of porphyrin deposited on different surfaces are important from a fundamental and technological point of view.

STM has been widely accepted as a tool for studying the layers in solution [35-37], in UHV [38-41], and in air [42]. The deposition and corrosion of metals, the changing and discharging of storage batteries, the wet processing of semiconductor devices, and many others similar processes, involve electrochemical oxidation-reduction reaction that take place at solid-electrolyte interfaces. Until the discovery of STM, only few in situ methods (e.g. Infrared adsorption spectroscopy (IRAS), ultraviolet (UV) - visible reflectance spectroscopy) had been developed for the structural determination of an electrode surface, in solution, at the atomic level. In situ STM makes it possible to monitor, under reaction conditions, a wide variety of electrode processes such as the adsorption of inorganic and organic species, the reconstruction of electrode surfaces, the dissolution and deposition of metals and semiconductors. A focused work on structure of specifically adsorbed anions, under potential deposition, adsorption of organic molecules and electrochemical dissolution of metals and semiconductors had been summarized by Itaya in 1998 [43]. Vacuum sublimation is one of the major methods used for sample preparation in the surface science studies [44, 45]. This technique enables the deposition of high purity materials in a well-controlled way. One disadvantage is to use this technique for molecules that decompose immediately by heating. An alternative method for molecular film preparation is the liquid-phase deposition, in which the molecules are dissolved and then applied to a solid substrate in the form of a liquid drop. There is no advantage of UHV studies, because of the simplicity of sample preparation and the stability of the interface in ambient. STM images of molecular layers are already obtained, which give an identical results in vacuum and in air [46].

Porphyrins are of particularly biological and optical importance because of their characteristic optical and chemical properties. Their properties are strongly affected by peripheral substituents and by the coordinated central metal atom, which is known to cause the conformational change in the porphyrin macrocycle. The porphyrin presented analogies with another class of molecules, the porphyrazine. The analogies are obvious due to their similar chemical structure. The difference comes from the presence of four meso-nitrogen atoms (in porphyrazines), opposed to the four methine groups (in porphyrins) in the central ring. The porphyrazine class of molecules is generally understood to include the tetraazaporphyrin (or porphyrazine) (TAP) and its analogues: the phthalocyanine (Pc), naphthalocyanine (Nc), and anthracyanine (Ac) molecules.

Porphyrins and other molecules with similar chemical structure have been intensively studied. The tendency to form ordered self-organized structures on a variety of substrate makes the study of these compounds important from fundamental and technological viewpoints. As substrates a variety of surfaces are investigated. There are STM investigations of ultrathin (submonolayer) thermally deposited films of Co-TPP and NiTPP on Au(111) [47], and studies of vapor-deposited copper(II) tetrakis(3,5-di-*tert*-butylphenyl) porphyrin (CuTTBPP) on Cu(100) in ultra-high-vacuum (UHV) [1]. Many other researchers have reported on different porphyrins, or porphyrazines deposited on different substrates. The next images, Fig.4.2.1, present a: a) tetrasubstituted porphyrin deposited on a graphite surface [48], b) a STM image at 63 K of Au(111) after the H2-TPP deposition [49] and c) STM topography of Cu-TBP-porphyrin sublimated at a base pressure below 10^{-10} mbar onto Cu(100) sample [50].

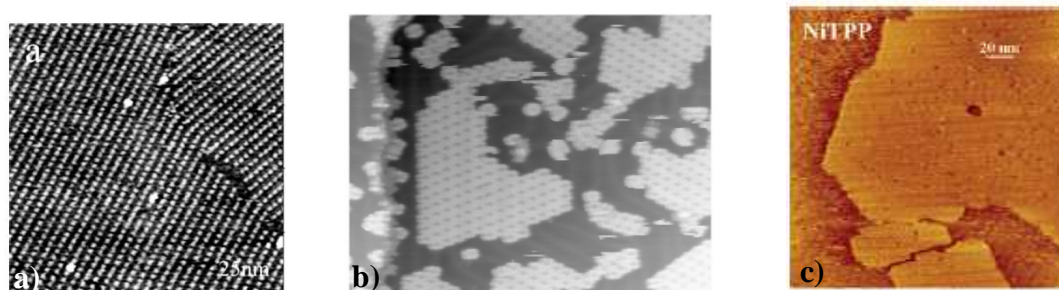


Fig. 4.2.1 a) TPP deposited on graphite; b) a STM image at 63 K of the Au(111) after the H₂-TPP deposition; c) low-resolution images of Ni-TPP absorbed on Au(111) [48-50].

The images show domains of ordered molecules with different orientation. These are examples of different types of porphyrins deposited on different substrate. An uncovered region of metal surfaces is observable between the porphyrins domains. These should demonstrate that molecules could be deposited onto a substrate and investigated by STM. The information, one can obtain from the STM images, is important and there are many questions about molecular structure, substrate influence, molecular orientation that are arising.

It has been already demonstrated that for several porphyrins (TPP, TBPP), the STM images of molecules consist of four bright lobes [50]. For example, for Cu-TBPP (Cu-tetra[3,5 di-*t*-butylphenyl]porphyrin), theoretical STM electron-scattering quantum-chemistry calculations [51-53] confirm that the lobes correspond to the di-*tert*-butylphenyl ligands [50, 54]. From Fig.4.2.1c, one can try to image a molecular arrangement for the molecules. Scudiero and al. [34] are suggesting a model for the arrangement of porphyrin molecules. They report STM images of ultra thin films of Co-TPP and Ni-TPP on Au(111). High-resolution STM data show the individual metallotetraphenylporphyrins (MTPPs) molecules in Fig.4.2.2. To determine the molecular arrangement, the authors create space-filled models of a typical metal (II)-TPP complex drawn to scale and placed by hand onto the STM image.

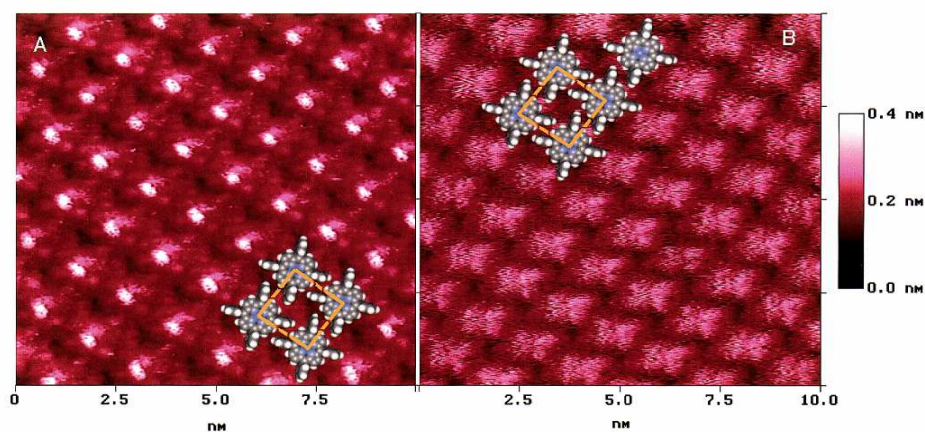


Fig. 4.2.2 High-resolution constant current STM image of a small region of a single molecule thick island of Co-TPP (A), and Ni-TPP (B) on Au(111). Inserted into the data image are spaces filling models of a typical MTPP [34].

The model of Scudiero et al. is based on a square arrangement for the porphyrin molecules, with an approximate lattice constant of about 1.4 nm length. The

bright centers of the Co-TPP molecules appear to be shifted a bit off center in Fig.4.2.2.

Yoshimoto et al. suggested another model for Co-TPP adlayers in solution, formed on the Au (111) surface [55]. The next figure shows a high-resolution STM image. An individual Co-TPP molecule can be recognized in Fig.4.2.3 as a propeller-shape with the brightest spot at the center and four additional bright spots at the corners of each Co-TPP molecule. The brightest spot at the center and the four additional spots of each Co-TPP molecule can be attributed, respectively, to the cobalt ion and the phenyl moieties in the Co-TPP molecule with a flat-lying orientation. The molecular rows consist of flat-lying Co-TPP molecules on the surface. Molecular rows, which are marked by arrows I and II in Fig.4.2.3, cross each other at an angle of approximately 85° .

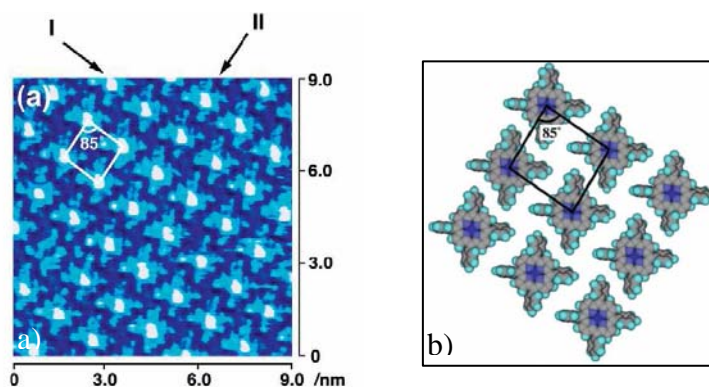


Fig. 4.2.3 a) High resolution STM image ($9 \times 9 \text{ nm}^2$) of Co-TPP and b) Structural model for Co-TPP adlayer [56].

Gimzewski and co-workers found that the packing arrangement of Cu-TBPP depends on the used metal substrate. They found out that changes in the porphyrins conformation occur predominantly by rotations around the bonds to the four tertiary butyl appendages, which differ on different metal substrates. STM images of Cu-TBPP in its adsorbed state consist of four bright lobes [50]. Both their dimensions and theoretical STM electron-scattering quantum-chemistry calculations [51-53] confirm that the lobes correspond to di-*t*-butylphenyl ligands [50]. The porphyrin core does not contribute significantly to the image because it is $\sim 0.7 \text{ nm}$ above the surface and it is consequently electronically decoupled from the substrate. In Fig.4.2.4, the high

resolution STM images of adsorbed Cu-TBPP molecules on Cu(100), Au(110) and Ag(110) substrates are shown [54].

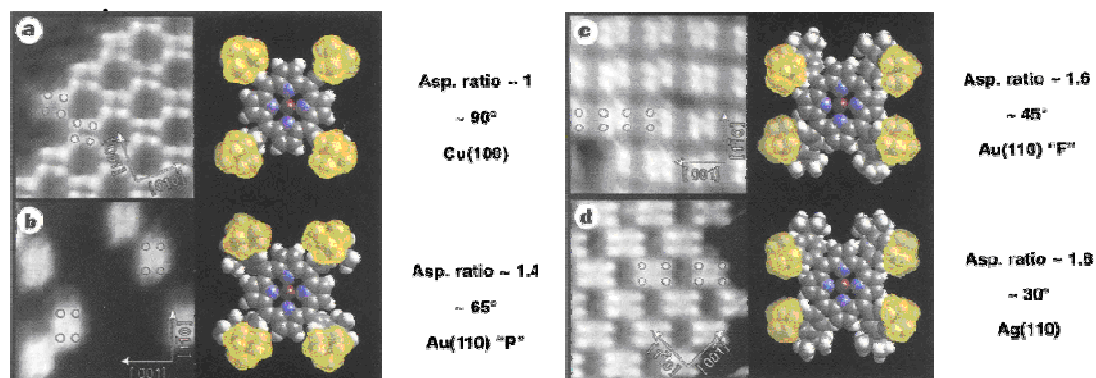


Fig. 4.2.4 Conformational identification of Cu-TBPP molecules [54].

Molecular models were constructed with bond angles chosen to match the experimentally observable dimensions. When adsorbed on a Cu(100) surface, the molecules have all four di-*t*-butylphenyl groups rotated $\sim 90^\circ$ with respect to the porphyrin plane. This leads to a square pattern. It has the same symmetry as the face-centered-cubic (100) substrate, but is rotated 20.5° with respect to the [010] direction. For the Au(110) surface, two distinct rotations were determined. These rotations correspond to an antisymmetric tilt of two opposite side groups by 65° and 45° . The 65° form is predominant after short annealing cycles (<10 min). The 45° form is predominant after longer annealing cycles. They assign the 65° conformation to a metastable precursor state and the 45° form to the thermodynamically stable conformation. The most pronounced conformational change upon adsorption is observed for Cu-TBPP on Ag(110), where the single adsorption state is characterized by a dihedral angle of 30° .

To demonstrate that STM offers the possibility to differentiate between two types of molecules, even when the mixed structures are studied, different experiments were performed. In the work of Scudiero and Hipps [47, 57], the first example of a bimolecular self-assembled 2D structure formed by vapor phase deposition onto a metal surface is presented. The coadsorption of porphyrin and fluorinated phthalocyanine results in a new bimolecular structure that was demonstrated by scanning tunnelling microscopy (STM) under UHV conditions at room temperature.

In Fig.4.2.5 constant current STM images of near monolayer coverage films obtained under UHV conditions at room temperature are shown.

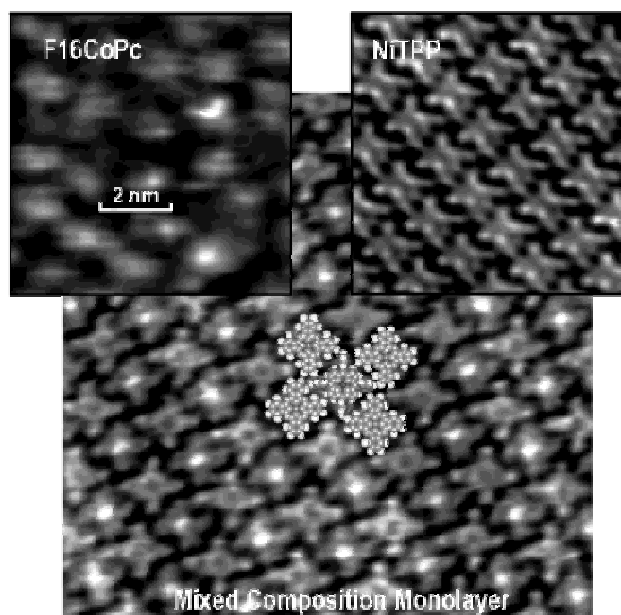


Fig. 4.2.5 Comparison of room-temperature constant current STM images of different organometallics adsorbed on Au(111) imaged under UHV conditions [47].

In Fig.4.2.5, it is shown in the top left image a high-resolution STM image of fluorinated phthalocyanine F16CoPc. It is obvious that the molecule does not form an ordered structure on Au(111). The top right image shows a high-resolution image of Ni-TPP (nickel-(II) 5,10,15,20-tetraphenyl-21*H*,23*H*-porphine, $C_{44}H_{28}N_4Ni$) adsorbed on Au(111). In contrast to F16CoPc, the Ni-TPP molecules form a well-ordered square structure. The main image of Fig.4.2.5 was obtained from a film that result when porphyrins and fluorinated phthalocyanine are co-deposited onto Au(111) at room temperature. In this figure, the F16CoPc are easily distinguished from Ni-TPP molecules by the strong tunneling current. The tunneling current is the result from orbital-mediated tunneling through the half-filled d_{z^2} orbital of the Co^{2+} ion. The molecules appear to have high protrusions in the center. The Ni-TPP molecules showed a depression in the center consistent with the filled d_{z^2} orbital of the Ni^{2+} ion. The contrast in tunneling current caused by the difference in electronic configurations of transition metal ion allows to clearly label molecular species for chemical identification at the molecular level. For the F16CoPc molecule deposited on Au(111)

no submolecular resolution was reported. In the mixture, submolecular resolution was observed, and the orientation of the phenyl groups in Ni-TPP could be determined.

A wide variety of STM studies of different molecules are studied by Scuderio et al. They showed that varying metal ions at the center of metal phthalocyanine complexes produced huge variations in the constant current STM images [38, 58, 59]. This was interpreted as being due to the changes in the tunneling probability associated with occupancy of the d_{z^2} orbital of the transition metal ion in electronic contact with the underlying substrate. In Fig.4.2.6, two islands of mixed composition Ni-TPP and Co-TPP (Ni(II) and Co(II) tetraphenylporphyrin) are shown. The contrast of these images is strongly bias dependent. Studies of metal TPP complexes, with the MTPP invariably appearing either as a dim or bright structureless feature depending upon the bias are reported [60]. This bias dependent variation of tunneling mechanism can be used to chemically distinguish different MTPPs.

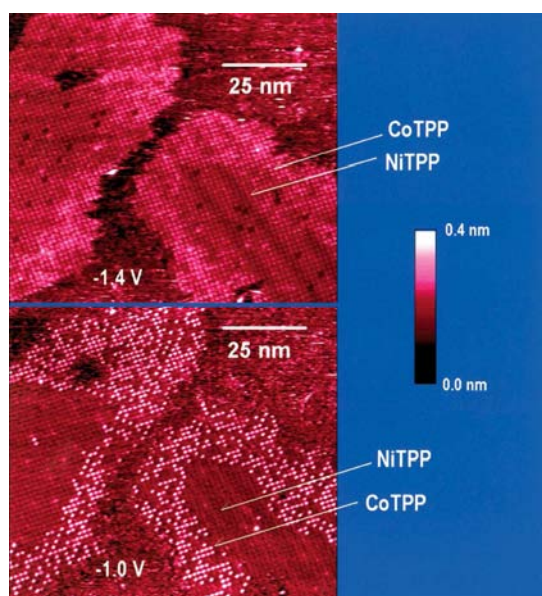


Fig. 4.2.6 Constant current tunneling images of mixed composition islands of Ni-TPP and Co-TPP at different bias voltages [34].

In the upper tile of Fig.4.2.6, it is not possible to distinguish Ni-TPP from Co-TPP at a bias voltage of 1.4 V. The orbital mediated tunneling is via a similar ring orbital on both molecules. The bias dependence of the orbital mediated tunneling through the central metal ion observed in metal tetraphenylporphyrins is also visible for the metal phthalocyanines. If the bias is reduced to -1.0 V, as one can observe in

the lower image from Fig. 4.2.6, the Co-TPP molecules appear much brighter (taller) than the surrounding Ni-TPP. Another explanation for the large orbital mediated tunneling through the Co(II) ion is that the TPP structure is deforming and thereby bringing the Co(II) ion closer to the surface than would be expected from the solid-state structure. However, the electronic properties of organic molecules on different surfaces will be discussed in the next chapter.

4.3. Electronic properties of organic molecules on surfaces

The iron-containing porphyrin is found as *heme* (of hemoglobin) and the magnesium-containing reduced porphyrin (or chlorin) is found in chlorophyll. At a closer side-by-side look, *heme* and chlorophyll can be considered as related molecules. This family shared a common biosynthetic precursor, uroporphyrinogen III, and a relationship between heme, chlorophyll a, and cobyrinic amide, the important tile of vitamin B₁₂ is shown in Fig. 4.3.1.

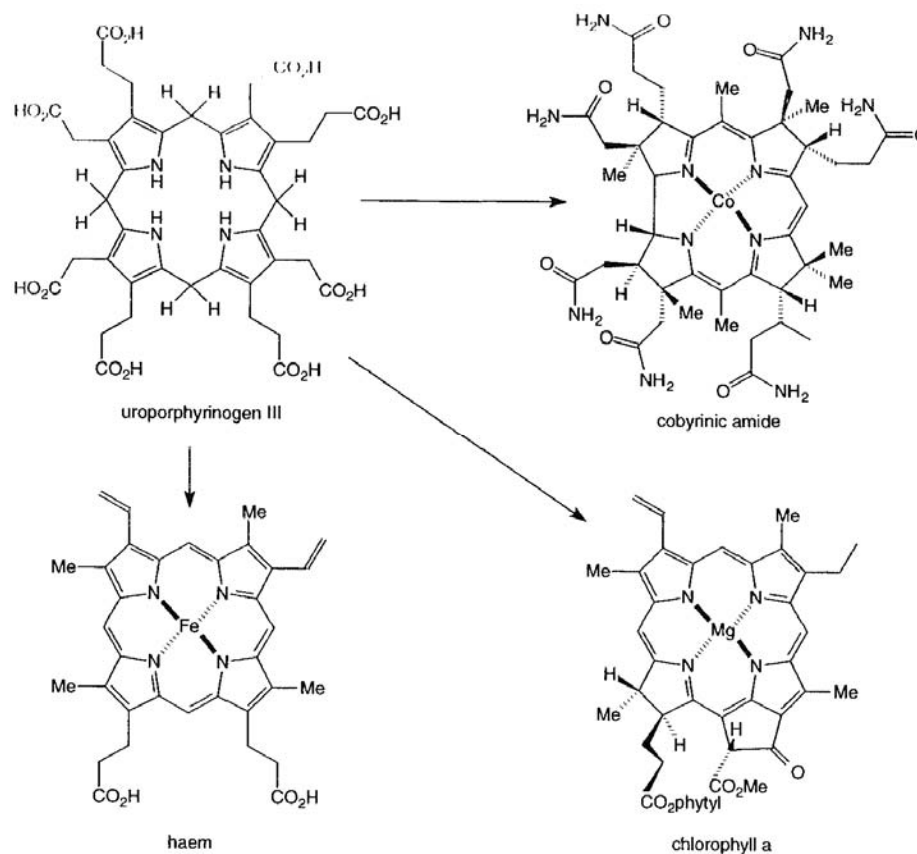


Fig. 4.3.1 Relationship between heme, chlorophyll a, and cobyrinic amide.

A functional building block of chlorophyll is a magnesium coordinating porphyrin. The chlorophyll is involved in photosynthesis. Here, the metal served to modulate the light-absorbing and energy-transfer characteristics of the chlorophyll, because it acts as a center for the binding of water. In *heme*, the complexed metal is iron. These complexes, as hemoglobin and myoglobin, reversibly bind oxygen. The oxygen can be transported around the body (hemoglobin) or stored in muscle tissue (myoglobin). One important aspect for these complexes is that the iron reversibly changes its oxidation state upon binding oxygen [25]. In vitamin B₁₂, the bound metal is cobalt. The vitamin B₁₂ is needed for building proteins in the body, red blood cells and normal function of nervous tissue. As the central metal atom, cobalt plays an important role, and recently, the interest on the research with cobalt porphyrin has been increased. Cobalt belongs to group nine, period four in the periodic system and the electron configuration is [Ar] 3d⁷ 4s². There are different oxidation states for Co (+2, +3). For the elementary bonds, the probability for a 2+ - oxidation state is higher than the 3+ oxidation state. For the complexes bonds the probability is higher for a

Co^{2+} oxidation state. Co^{2+} constructs octahedral, tetrahedral, square planar (rarely), and square pyramidal complexes. Co^{3+} is in complexes widely octahedral. For Co^{2+} the high-spin complexes (octahedral or tetrahedral; three unpaired electrons with a magnetic moment of 4.7-5.2 Bohr's magnetons) and low-spin complexes (octahedral-distorted, square pyramidal, square plane; one unpaired electron with a magnetic moment of about 2.5 Bohr's magnetons) are well known. Co^{3+} constructs especially low-spin complexes (no unpaired electrons).

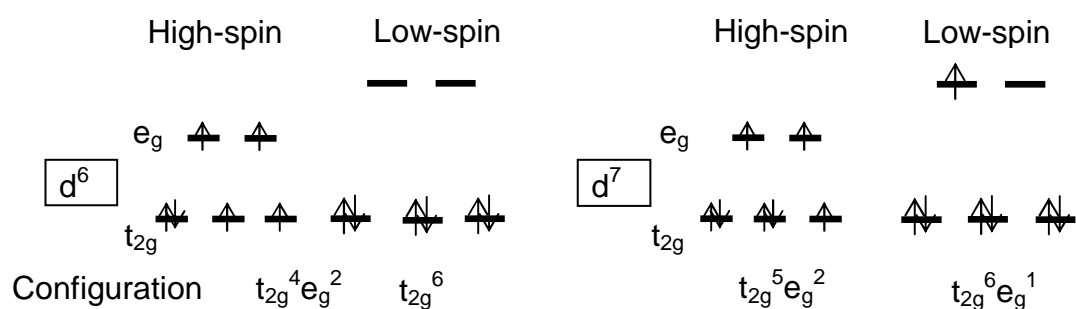


Fig. 4.3.2 High-spin, low-spin schema for Co^{3+} (d^6) and Co^{2+} (d^7) ions.

A particular case is represented by the interaction between the porphyrin ligand and a Co^{2+} ion and creates square-plane complexes. Metalloporphyrins are known to have a high molecular symmetry (square-planar D_{4h}). The same molecular symmetry is also found for Co-porphyrin (for example from Rovira et. al. [61], after calculations performed by means of density-functional theory within the LSD (spin unrestricted) approximations). Analysis of the highest occupied spin orbitals of the ground state displays the cobalt d orbital configuration is $(d_{xy})^2 - (d_{xz})^2 - (d_{yz})^2 - (d_z^2)^1$. The rigid porphyrin ring represents one reason for this symmetry. The porphyrin ring with this π -system has a restricted mobility, and with the four ligands completely border the central metal ion in this plane. In Fig.4.3.3, the orbital splitting energies from an octahedral complex to a square planar complex are described.

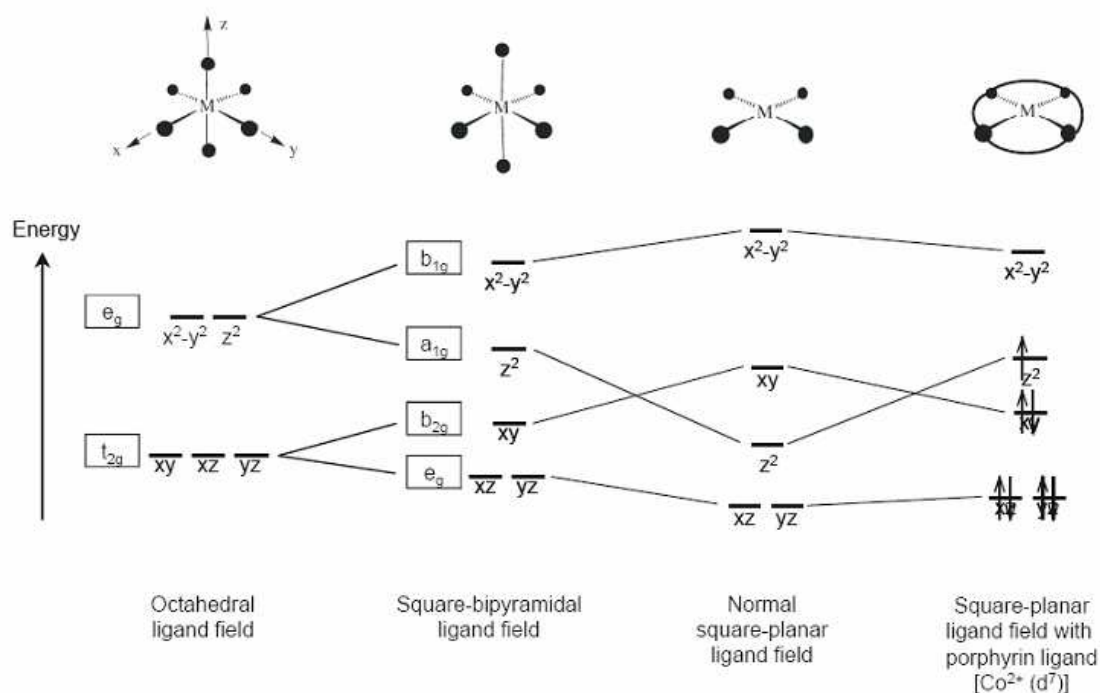


Fig. 4.3.3 Splitting of orbital energies in an octahedral, square-bipyramidal, normal square planar complexes or square planar with porphyrin ligand field [62, 63].

For octahedral complexes, the molecular orbitals can be described as resulting from a combination of central metal atom accepting a pair of electrons from the donor ligands [64]. The $d_{x^2-y^2}$ and d_{z^2} orbitals can form bonding orbitals with the ligand orbitals, but the d_{xy} , d_{xz} and d_{yz} orbitals cannot form bonding orbitals. The $d_{x^2-y^2}$ and d_{z^2} orbitals are energetically raised in the ligands direction because of the spatial orientation. The other orbitals are energetically lowered. The transition from square-bipyramidal ligand field to normal square-planar ligand field is made by increasing the ligand distance on the z-axis. For the square-planar complex, the lower energy is for the d_{xz} and d_{yz} orbitals; an increased energy is presented by d_{z^2} orbitals. The energy series is completed by d_{xy} orbitals and $d_{x^2-y^2}$ orbitals, with the highest energy. In Fig.4.3.3, the splitting of orbital energy is presented, especially for the Co central metal ion case. The splitting energy can be modified by changing the four different ligands with porphyrin ligands. Fig.4.3.3 shows the electron configuration in a square-planar ligand field with porphyrin ligand for Co²⁺ central metal ion. Since this is a

low-spin complex, there is one unpaired electron on d_{z^2} orbital. The $d_{x^2-y^2}$ orbital is unoccupied.

The electronic structure and bonding in metal porphyrin are of a large interest. In addition, the mechanism of electronic conduction in and between molecules is a question of fundamental importance in molecular electronics, electrochemistry, and biochemistry. Different theoretical calculations were made (based on Hückel molecular orbital methods or density functional theory) to determine this structure. Liao et al. [65], with the help of the density functional theory (DFT), made a comparative theoretical study of complexes of porphyrin (P), porphyrazine (Pz), and phtalocyanine (Pc) with metal (M can be Fe, Co, Ni, Cu, and Zn).

It is known that the electron density and the local density of surface near the Fermi energy play an important role in determining the STM images. High-resolution images of planar aromatic molecules exhibit a characteristic intramolecular tunneling current distribution in the STM. Starting from the benzene molecule on the Rh(111) surface [66], an increasing numbers of molecules have been successfully imaged with submolecular resolution. The submolecular resolution is a connection between the molecular orbital density and the STM image contrast.

For the Cu-phtalocyanine adsorbed on Cu(111) [67], a close correlation of the observed image contrast with the calculated HOMO and LUMO densities has been observed. The independence of the observed image pattern from the polarity of the applied tunneling voltage has been attributed for this system to the close similarity of the calculated HOMO and LUMO wavefunctions. The PTCDA molecule presents the first molecular system where the tunneling current distribution was assigned to one of these frontier orbitals in a concrete way [68]. The submolecular image contrast as observed on graphite and MoS₂ shows a characteristic pattern of 10 bright spots which correspond to the tunneling current maxima [69]. With additional information (atomic coordinates, bond lengths and angles known from X-ray structure analysis) and the dimension of the unit cell taken from the STM images, the bright spots can be related to the molecular structure in Fig.4.3.4. The six oxygen atoms are invisible in the STM pattern, because the center of the four brighter spots lie between intramolecular pairs of hydrogen atoms and the six smaller and weaker spots close to the long axis of the molecule are positioned between two carbon atoms each.

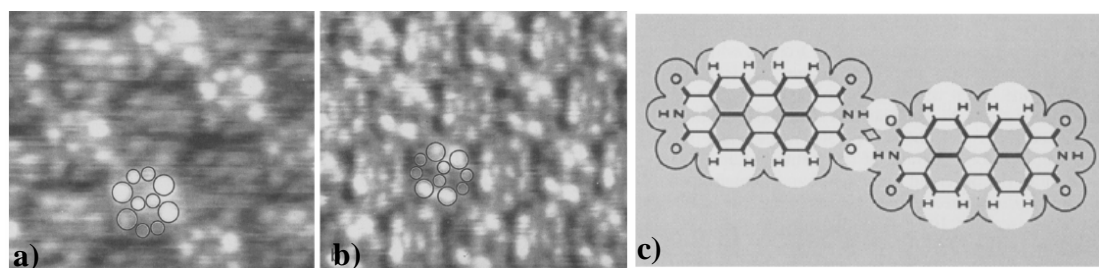


Fig. 4.3.4 Comparison of the submolecular resolved images obtained from the investigated systems. The observed inner structure of the molecules is similar in all cases. a) PTCDA on graphite; b) PTCDA on MoS_2 ; c) Correlation between the observed tunneling current maxima in the high-resolution images and the molecular structure.

The current distribution reveals a close similarity to the wave function of the lowest unoccupied molecular orbital (LUMO) [69, 70]. This current distribution was attributed to the electron acceptor behavior of the PTCDA molecule. In the STM images, the perylene cores of the molecule dominate the image contrast and the electronic structure of this core is nearly undisturbed by the substrate. The four brighter spots are at the positions of the electropositive hydrogen atoms, the six smaller spots correspond to the six longest C-C bonds in the molecule. So, the observed inner structure cannot be explained by the local density of state arguments, because all tunneling current maxima are at the positions with lower electron density. From the Hückel MO-theory it is known that a longer bond and the electropositive character of hydrogen correspond to lower electron densities. In the presented model, the lower electron density is equivalent to an increased pseudo potential at these positions. In the calculated HOMO the maxima do not correspond to the observed tunneling current maxima, which instead coincide with the HOMO wave function minima. Only the observed inner structure corresponds qualitatively to the expected maxima of the single electron pseudo potential.

For a detailed understanding of the contrast mechanism, a comparison with the calculations based on an appropriate theory is necessary. The first theoretical formulation of the STM image contrast has been given by Tersoff and Hamann [12], based on Bardeen's formalism [71]. This theory gives a simple explanation of the tunneling current distribution for small tunneling voltages in terms of the local density of state. The next step towards it is made by Fischer and Blöchl [72]. They calculated the STM images contrast of benzene on graphite and MoS_2 using a first principles molecular dynamic calculation. For small voltages, they calculated an image contrast

dominated by substrate states, which are modulated by the adsorbate. The submolecular image contrast therefore should be strongly dependent on the specific adsorption site. At higher voltages, the image contrast is dominated by the respective occupied and unoccupied molecular states.

The influence of the tip on the image contrast is important, but in many cases this influence was neglected, even so, many authors remarked the influence. Consequently, some groups started to consider the complete system with tip, substrate and molecules in their calculations. Sautet and Joachim examine the molecule as a disturbance of a periodic potential of the bulk crystal [73]. Ou-Yang et al. [74] proposed a formulation where the tunneling tip is modeled by a semi-infinite chain of atoms and the possibility of an electronic coupling between the tip and the sample has been explicitly taken into account. Many parameters concerning the tip conditions during the STM measurement are unknown. For a reliable comparison of experimental and calculated results, high quality images of molecules with a characteristic image pattern are necessary.

Strohmaier et al. [75] present a systematic study of the submolecular image contrast for aromatic molecules. Planar aromatic molecules are used as model systems on weakly interacting substrate. They also compared the submolecular image contrast of the investigated molecules with the shape of their respective HOMO and LUMO orbitals. On graphite, for weakly bonded molecules, the image contrast is dominated by the wavefunction of the specific frontier orbital being closest to the Fermi level of the substrate. For electron acceptor type molecules, this is the lowest unoccupied molecular orbital (LUMO), whereas for electron donor type molecules the highest occupied molecular orbital (HOMO), has been observed. On the stronger binding Ag(111) surface it is found that acceptor type molecules showed an unchanged image contrast compared with graphite. For the donor type molecules, the image contrast changes from HOMO on graphite to LUMO on Ag(111). The next figure presents a frontier orbital model of PTCDA, calculated for a free molecule using the semi-empirical MNDO approximation and STM images of PTCDA on MoS₂ and on Ag(111). Making a comparison between HOMO and LUMO wave functions of PTCDA and STM images is easy to recognize that the image contrast showed a close similarity to the LUMO wave function. The HOMO wave function does not fit in, and the small contribution of the oxygen atoms is invisible in STM images.

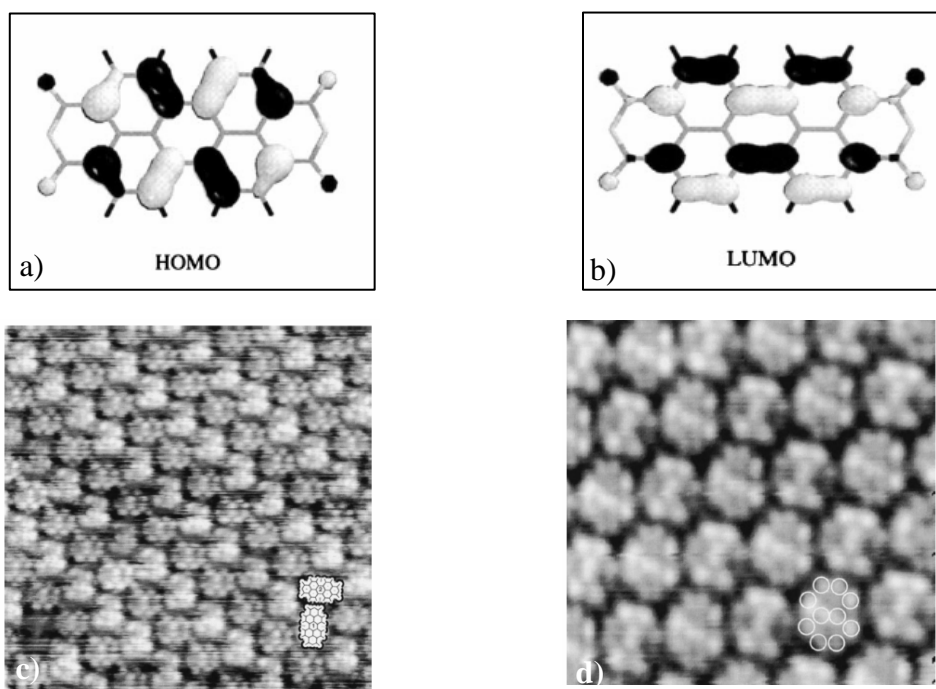


Fig. 4.3.5 *a,b) -Frontier orbitals of PTCDA, calculated for a free molecule using the semi-empirical MNDO approximation; c,d) - submolecular image of PTCDA on MoS₂ and Ag(111).*

The presence of metal, ring and peripheral group centered electron transport processes have made porphyrins and phthalocyanines interesting model systems for scanning tunneling microscopy and orbital-mediated tunneling spectroscopy studies. There are studies made to investigate monolayers and submonolayers in UHV, under an inert atmosphere, or in solution. These studies have produced molecular images and tunneling spectra that show a clear connection between orbital mediated electron transfer processes and the expected HOMO and LUMO energies. It is also known that metalloporphyrins can undergo reversible redox reaction, in which the site of electron transfer is localized on the porphyrin ring or on the central metal atom. Scudiero et al. [76] studied thin film of vapor-deposited Ni(II) and Co(II) complexes of tetraphenylporphyrin (Ni-TPP and Co-TPP) on gold, and they focused on the electronic spectroscopic properties of metallotetraphenylporphyrins. The energies of the highest occupied and lowest unoccupied π orbitals and the highest occupied d metal orbital are determinate by comparing results from STM, tunnel diode, and ultraviolet photoelectron spectroscopy (UPS) measurements, which overlap and are in agreement with their overlapping regions.

4.4. 2D-Chirality on surface

Chirality is the geometric property of a rigid object (or spatial arrangement of points or atoms) of being non-superposable on its mirror image. In chemistry, this is equal to the handedness of an asymmetric molecule. By handedness of molecule one means the existence of left/right opposition. The term “chiral” comes from the Greek name “kheir”, which means “hand”. This term was coined by Lord Kelvin in 1904, in his Baltimore Lecture on Molecular Dynamics and the Wave Theory of Light, in which he stated:

"I call any geometrical figure, or group of points, chiral, and say it has chirality, if its image in a plane mirror, ideally realized, cannot be brought to coincide with itself."

The symmetry of a molecule (or of an object) determines whether the molecule is chiral or not. The enantiomers are non-superimposable mirror images of one another. For a compound to form an enantiomeric pair, it must have chiral molecules. Chiral molecules must not have an internal plane of symmetry, but they must have a stereocenter. One characteristic that enantiomers exhibit is configuration. Configuration is the special way, how non-equivalent groups arrange themselves around a stereocenter carbon. One enantiomer will be configured right handedly (R) and the other will be configured left-handedly (L). In Fig.4.4.1, is shown a chiral molecule with its mirror image.

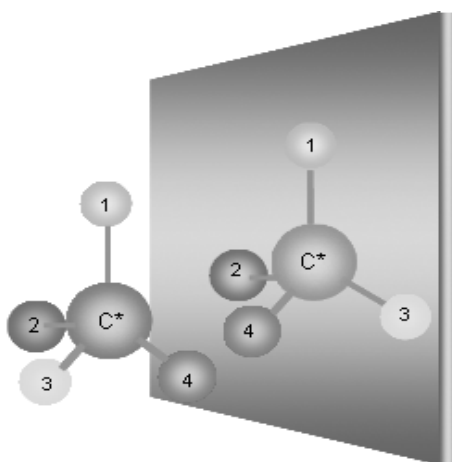


Fig. 4.4.1 A chiral molecule with its mirror image.

It is well recognized that the adsorption of organic molecules on solid surface is one of the fundamental processes for the development of molecular-based nanodevices. The geometric structure of adsorbed molecules and molecules arrangement are responsible for physical and chemical proprieties. Chiral specificity is consequently fundamental in chemical biology and pharmacology. The conformations of adsorbed molecules influence the outcome of surface-catalysed reactions and turned out to be important for recognition processes involved in chemical sensors [77]. Since the STM has been shown previously to be capable of distinguishing between different molecular conformations on a surface [54], it makes also possible to probe chiral phenomena at surfaces at the molecular level.

Molecular surface structures can show important stereochemical effects. For example, excluding the truly chiral molecules, another class of molecules, so-called prochiral molecules becomes chiral once confined on a surface. In addition, there is an associated loss of symmetry.

The conformational changes have implications for the chiral ordering on surface. The images shown in Fig.4.4.2 show molecules that consist of a linear backbone formed from three benzene rings connected by ethynylene spokes, and functionalized at both ends with an aldehyde, a hydroxyl and a bulky *t*-butyl group.

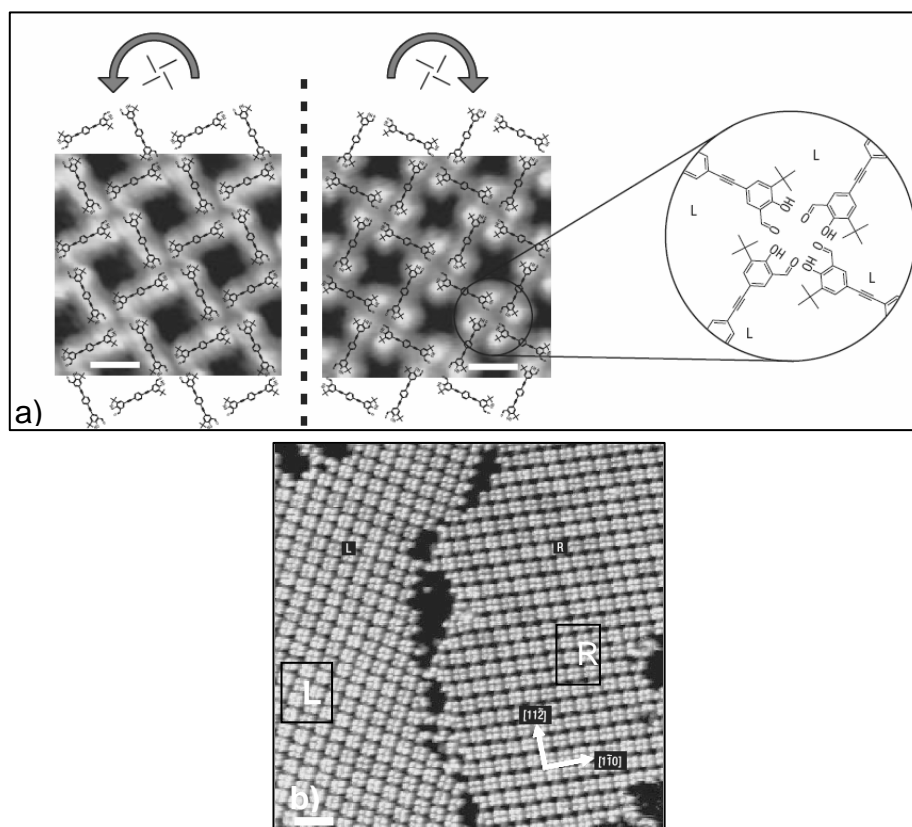


Fig. 4.4.2 a) STM images and schematic model of the network structure (scale bar 2nm); b) Large scale STM showing two homochiral domains [78].

Fig.4.2.2a shows two coexisting phases formed from the molecules. There are two domains of opposite chirality, as seen from the sense of rotation for the chiral windmill motif. The zoom-in on a structural node presents the correlation between the tiling pattern and the molecular chirality. This leads to homochiral domains consisting exclusively of right-right (RR) or left-left (LL) conformers. Fig.4.2.2.b is showing two homochiral domains of opposite chirality. The ability to switch chirality by performing one or more conformational changes enables the molecules to accommodate to the chiral template found at the edge of an island and to incorporate themselves into homochiral domains.

Also for porphyrins, chiral conformations are observed. STM images of a porphyrin molecule with four *tert*-butyl-phenyl groups (H2-TBPP) form square superstructure domains of chiral conformations on Cu(100)[79]. In Fig.4.4.3, the two square domains, notated α and β , are shown, the clean substrate Cu(100) is also shown in the upper-right inset.

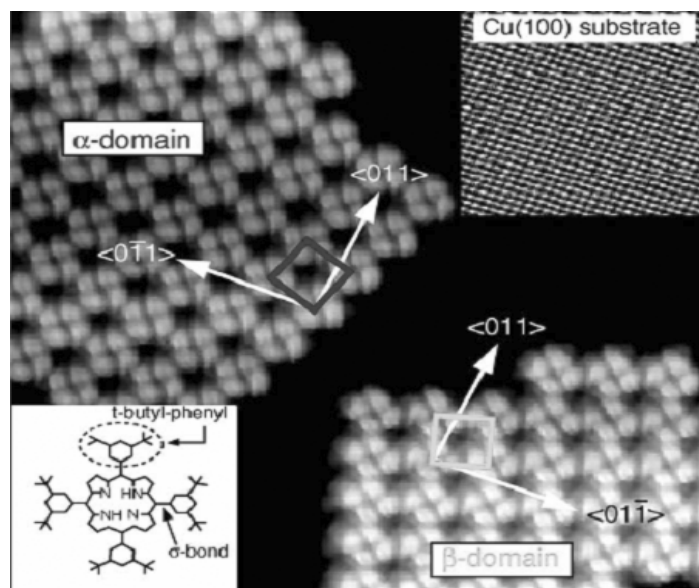


Fig. 4.4.3 STM images of the twin domains of H₂-TBPP on Cu(100) surface, with the upper inset-Cu(100) substrate and the lower inset: H₂-TBPP structure [79].

For these molecules, it is demonstrated that the deformation of H₂-TBPP forms a pair of chiral conformations. The ideal conformation is the result of several types of deformations. In this case, the twisting rotation of the phenyl rings around the σ -bonds between the phenyl rings and the porphyrin macrocycle and the tilting of the phenyl rings with respect to the porphyrin macrocycle lead to the formation of the chiral conformations. The conformation determines which of the twin domains is formed. The images of H₂-TBPP in Fig.4.4.3 show that the molecular orientation does not coincide opposite with the substrate orientation. The molecules in the α -domain are rotated clockwise and those from β -domains are rotated counterclockwise. A domain is entirely composed of a single chiral conformer absorbed to identical sites.

High-resolution scanning tunneling microscopy data has revealed how the symmetry information of molecular building blocks is readily expressed in the resulting chiral or nonchiral supramolecular networks [80].

5. Results

After a short introduction of the Ag(111) substrate and the presentation of the corresponding STM images with atomic resolution, first results of the self-assembly of TPP or TTBPP molecules on Ag(111) are given.

5.1. Atomic resolution on Ag(111)

As a first step, the clean substrate was investigated. Silver has a face-centered-cubic structure. The most stable surface for silver is the (111) surface, which is a hexagonal close-packed plane of silver atoms [81]. Fig.5.1.1 shows: a) the silver cubic face centered structure and b) a top view of the (111) surface.

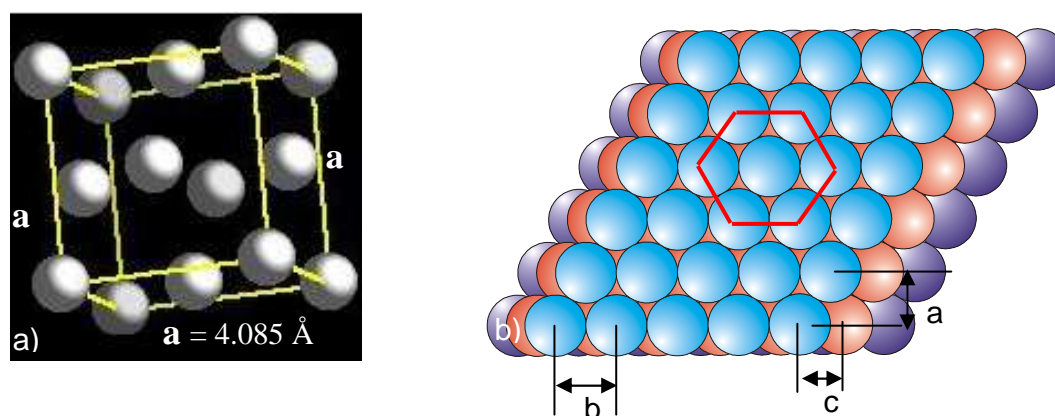


Fig. 5.1.1 a) The cubic face centered silver structure and b) the top view of the (111) surface.

In Fig.5.1.1b, two terraces are observable and the important distances are marked with a, b, c. The next neighbor distance is indicated by “b” and has a value of 2.889 \AA . The distance between atoms in densely packed rows is marked with “a” and

has a value of 2.502 \AA . The “c” represents the distance between the layers from (111) structure and has a value of 2.359 \AA . The silver atoms form a closed packed hexagonal pattern with a lattice constant of 2.889 \AA . This hexagonal lattice is marked by the red hexagon in Fig. 5.1.1b.

The Ag single crystal with the (111) orientation was at first prepared by means of several cleaning cycles before the STM investigation (Ag(111) preparation described in Chapter 3). Fig.5.1.2 represents a typical STM image of the clean Ag surface, showing the coexistence of adatom islands and vacancy islands. The coexistence of monolayer-high adatom islands and vacancy islands was reported by J.T. Li and W.D. Schneider [82].

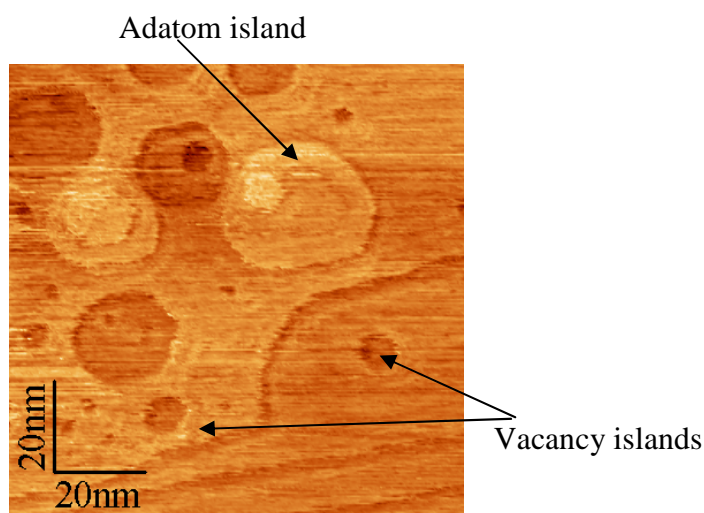


Fig. 5.1.2 STM constant current topography of Ag adatom islands and vacancy islands on Ag(111). The image was taken under scanning conditions of $I_{set} = 2.6 \text{ nA}$ and $U_{gap} = -0.3 \text{ V}$ at room temperature.

For the Ag(111) sample, the surface atom mobility is high at room temperature. The dynamics of the surface structures are captured by continuous imaging of a specific area. Fig.5.1.3 shows a series of images recorded on the clean silver surface structure, in a time scale of minutes.

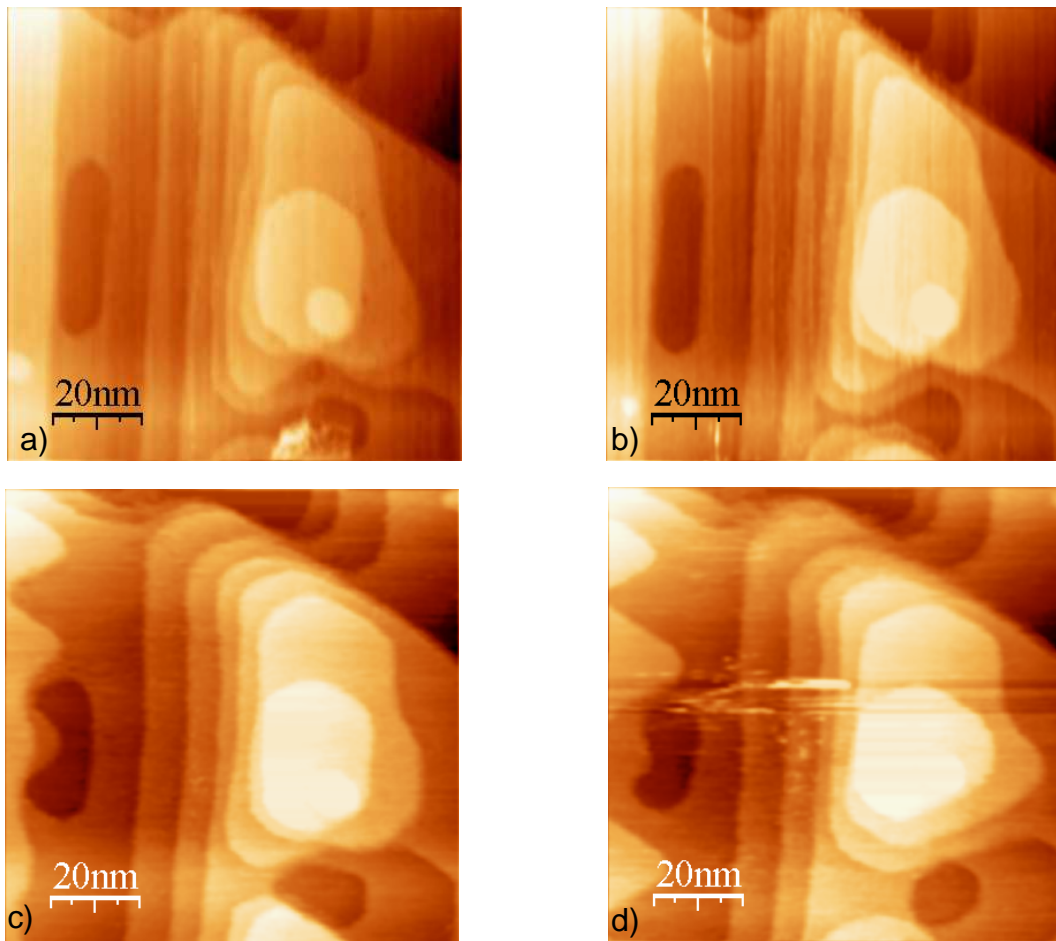


Fig. 5.1.3 Time evolution of the surface structure from a to d. The tunneling parameters were set as $I_{set} = 1$ nA and $U_{gap} = -0.3$ V. The time interval between first and the last image is $t \approx 4$ min.

For the first two images, the scan direction is horizontal, and for the next, the scan direction is vertical. This configuration is kept for minutes, so that the image sequence of the relaxing step is well resolved in time and shows smooth and dynamically varying structures. These images demonstrate the mobility of the surface atoms and the influence of the tip. The tip influences are better observable in the last STM image. Similar thermal equilibrium fluctuations of monoatomic surface steps and island structures on Ag surfaces were investigated by N. Quaas et al. [83].

Fig.5.1.4 shows a silver surface with terraces. Here terraces with a height from approximately 0.15 nm (1.445 Å is the atom radius in crystal) to values of 0.35 nm are measured.

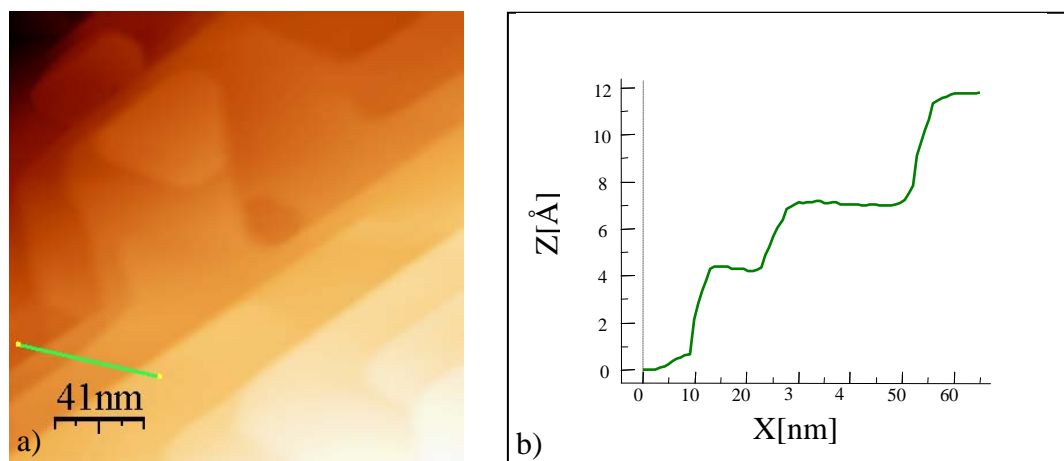


Fig. 5.1.4 STM topograph of Ag crystal and the profile from this image. The tunneling current is $I_{set} = 1$ nA by a bias voltage of $U_{gap} = -0.43$ V. The scan areas are 2.63×2.63 nm² for the a) image and 5.0×5.0 nm² for the b) image.

Fig.5.1.5 displays atomically resolved STM images from the clean Ag(111) surface. In these STM images, the Ag atoms appear as protrusions. The distances between the protrusions of these patterns should be in good agreement with the lattice spacing of Ag(111) surface. For Ag(111) the lattice spacing is 2.88 Å.

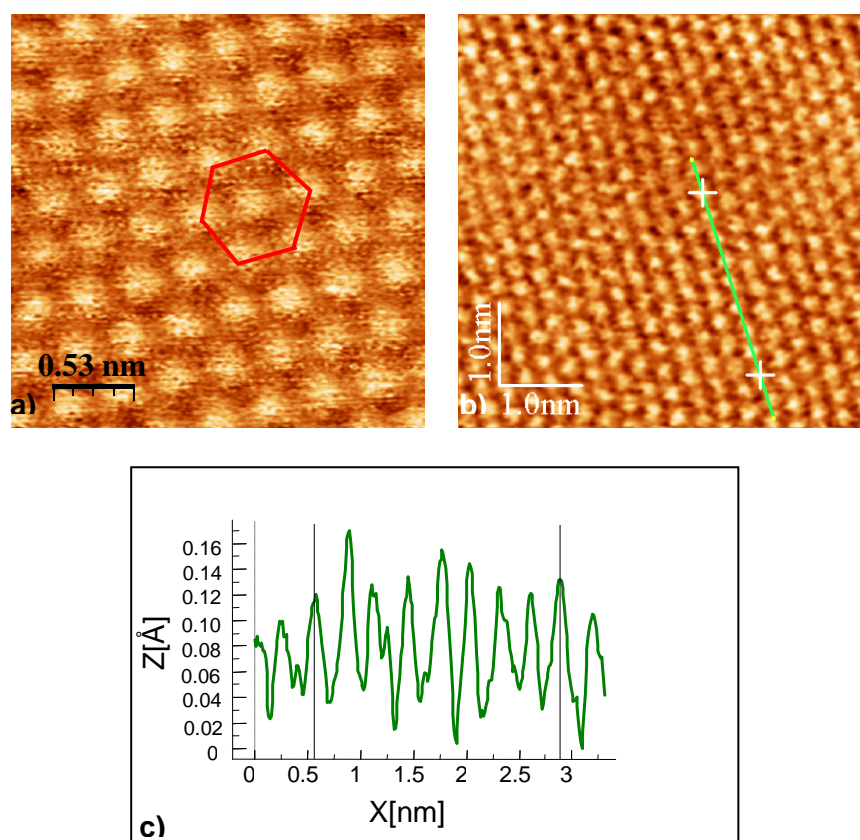


Fig. 5.1.5 a), b) High resolution STM imaging for Ag(111) ($U_{gap} = -0.04$ V and $I_{set} = 0.8$ nA) and c) the profile line for measuring the lattice spacing.

Fig.5.1.5c shows a profile line applied to measure the lattice spacing. Here the next neighbor distance is determined of 3.0 \AA , a value that it is in good agreement with the expected value of 2.88 \AA . The hexagonal arrangement, marked by the red hexagon, can be clearly seen in the Fig. 5.1.5a. The atomically resolved image of the clean surface was scanned at room temperature

Another method applied to obtain more information about the clean silver surface was LEED (method described in the Chapter 2.3). Fig.5.1.7 shows an example of a LEED pattern for the first order spots and a two-dimensional Fourier transformation (FT) of a STM image of the atomically resolved silver surface. The densely packed Ag(111) surface shows a hexagonal LEED pattern. The same hexagonal pattern is showed by the FFT image. The middle line from the FFT image represents an artifact from the scanning procedure.

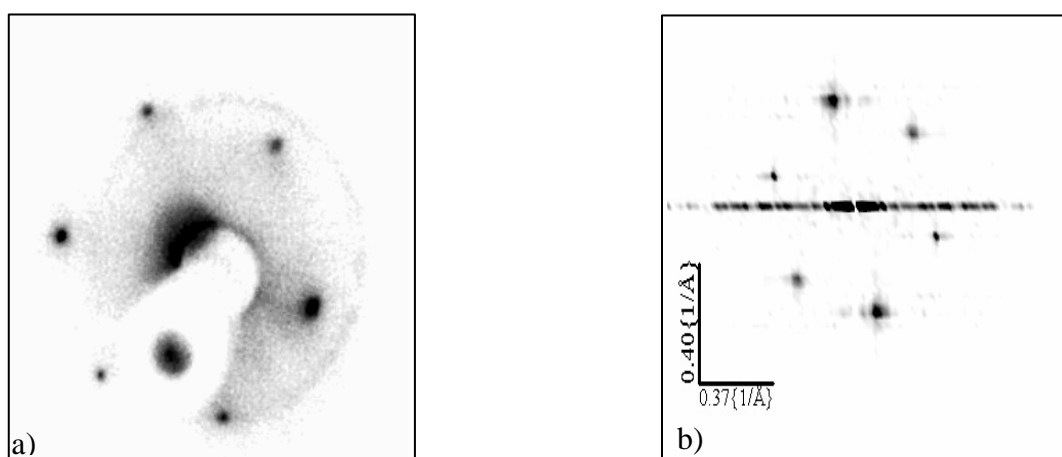


Fig.5.1.6 a) (1x1) LEED pattern compared with b) FT-STM imaging atomic resolution on Ag(111) surface. The LEED image was obtained at the acceleration voltage of 113 eV.

The presented results show that the preparation procedure of the crystal is sufficient to achieve the well known features for clean Ag(111) surfaces.

5.2. Arrangements of TPP molecules

Formation and characterization of ordered layers of porphyrins is important from the fundamental and technological point of view. The understanding of the adsorbate/substrate and adsorbate/adsorbate interactions is an important issue in the development of ultrathin 2D structures. To understand the formation and possibly the involved interactions of porphyrins on the Ag(111) surface, porphyrin layers with different coverage were prepared on the Ag(111) surface by varying the deposition time. Fig.5.2.1 shows sub-monolayers of Co-TPP molecules deposited on Ag(111).

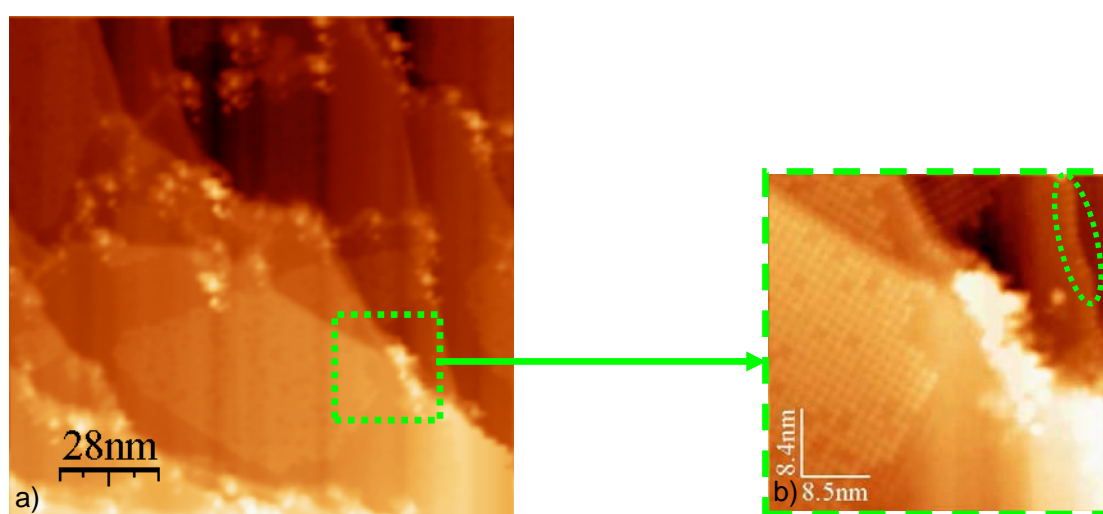


Fig.5.2.1 STM images of the deposited Co-TPP molecules on a Ag(111) surface. The image a) was scanned with a 0.7 nA tunneling current and a negative bias voltage of 0.7 V and b) with a 0.3 nA tunneling current and a negative bias voltage of 1.2 V. The scan area for Fig.5.2.1a is 139nm x 139 nm and the speed was 300 ms/line.

The Fig.5.2.1b represents a zoom in from the larger area in Fig.5.2.1a. In the left part of Fig.5.2.1a ordered domains of Co-TPP can be observed. Each protrusion corresponds to a single molecule. In the upper right corner of Fig. 5.2.1b, a “chain” of molecules is visible. The green landmark marks the “chain” position. The position of this feature coincides with a silver step edge. This decoration of silver steps by Co-TPP can be interpreted as due to an energetically favorable adsorption site of the porphyrins at the step edge. Similar observations were also reported by Kamikado et al. [84] and Barlow et al. [85]. Summing up the tendency to form islands with ordered molecular arrangements and the decoration of silver steps was observed for Co-TPP

on Ag(111). The region between the islands appear to be the uncovered Ag(111) surface. Analysis of many images taken from several experiments indicates that separated islands of molecules with different azimuthal orientation are observed.

The images in Fig.5.2.2 show a monolayer of Zn-TPP. The overview image in Fig. 5.2.2a shows three different silver terraces with different domains of highly ordered Zn-TPP. The domains exhibit different orientations and within the domains, the single molecules can again be identified as protrusions. The tendency to exhibit a different azimuthal orientation was also reported by Yoshimoto et al. [56]. For the presented examples of two different metalloporphyrins, the tunneling parameters were similar.

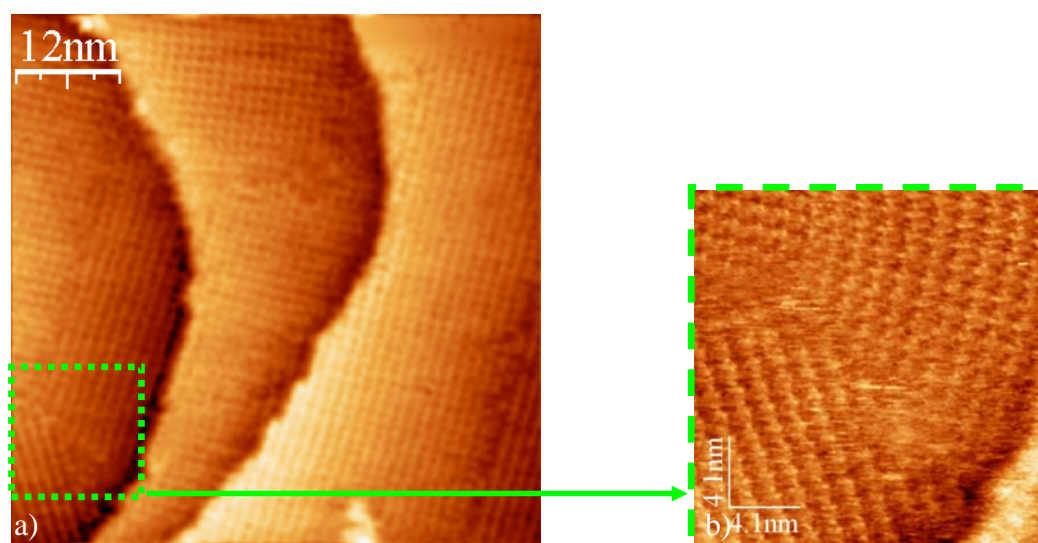


Fig.5.2.2 Zn-TPP molecules imaged by STM measurements. The Zn-TPP images were scanned with a current of 0.7 nA and a bias voltage of -0.87 V by a scan speed of 200 ms/line. For Fig.5.2.2a, the scan area is 62.5 nm x 62.5 nm and for the b) images the area of 20.3 nm x 20.3 nm.

The Zn-TPP image in Fig. 5.2.2b, which was acquired at the indicated position in Fig.5.2.2a with higher magnification, illustrates that ordered domains of porphyrins exhibits different orientations. In Fig.5.2.2b, three domains of porphyrin molecules can be identified. A region of disorder, where no single molecule can be identified, is seen in the center of this image, where the three domains meet. This can be attributed to a higher degree of mobility in this region [58], or to the molecular disorder. The Ag(111) sample has a 3-fold symmetry. If the porphyrin domains would be commensurate with the surface one would expect that orientations of the domains would reflect the symmetry of the surface, e.g., multiples of 120°. However, no

obvious connection between the directions of the domains and the substrate geometry could be observed. Therefore, the molecule-molecule interactions are assumed to dominate in the ordering process. Weak molecule-substrate interactions often lead to epitaxial growth of molecular films, with small distortions of the symmetry from the bulk crystals. For strong molecule-substrate interactions, the symmetry of the substrate is known generally to affect the symmetry of the epitaxial organic film. The domains of Co-TPP and Zn-TPP observed so far obviously exhibit a square order whereas the underlying silver substrate has a hexagonal symmetry. For the Zn-TPP preparation on Au(111), there are indications that the formation of the adlayer structures is independent of the surface and that suggest that the interaction between Zn-TPP molecules is stronger than that between molecule and substrate [55].

Another aspect was the stability of the monolayer. The next series of STM images showed in Fig.5.2.3 indicate how stable the monolayer is. The tunneling parameters for the STM images are already indicated in Fig.5.2.2a, since the micrograph represented one image of these series. The imaged area is not the same. There are small variations due to thermal drift. To identify the same region the green landmark was introduced. The images are recorded in a time interval of 25 minutes. The loss of image quality in the very upper part of Fig.5.2.3d may be due to a changed tip. The porphyrin adlayer appears to be generally stable. The observed changes occur mostly at the domain boundaries preferably if there is some surface area which is molecule depleted, as indicated by the white arrows in Fig.5.2.3a and b. In these images, one can also observe that the domain indicated with **B** is growing at the expense of the domain indicated with **A**. It should be noted, that changes in ordered molecular structures of tetraphenylporphyrins were never observed while imaging a confined area without domain boundaries or depleted areas (e.g. Fig. 5.2.4). This indicates that a molecule in the middle of a ordered phase is highly stabilized by its neighbouring molecules. A molecule in the domain boundary in comparison is lacking in neighbouring molecules and is consequently destabilized. Therefore these less stable molecules are able to diffuse and possibly join an other domain.

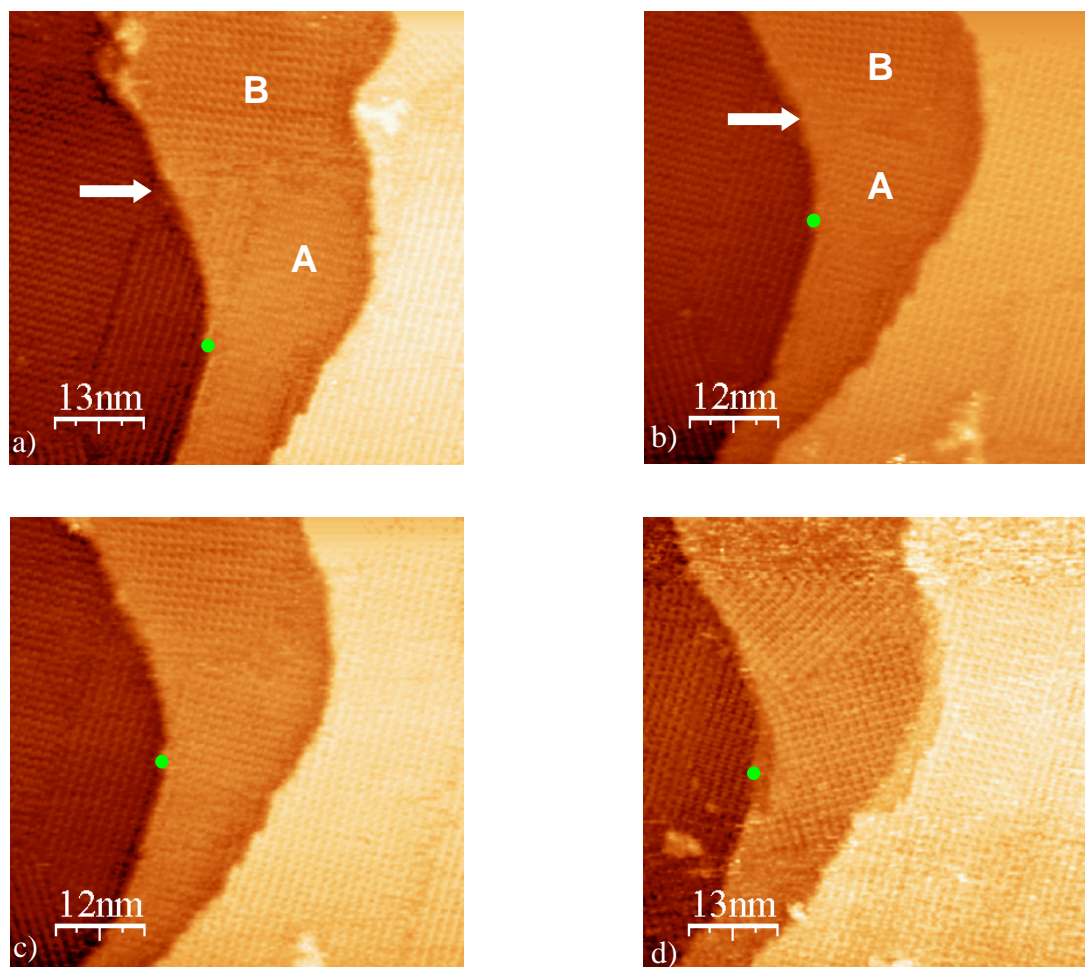


Fig. 5.2.3 Series of Zn-TPP images. The Zn-TPP images were scanned with a current of 0.7 nA and a bias voltage of -0.87 V by a scan speed of 200 ms/line. The scan area is 62.5 nm x 62.5 nm.

To clarify the structural details of the porphyrin layers, high-resolution STM images were recorded. Fig.5.2.4 shows typical STM images of Zn and Co-TPP, revealing the molecular arrangement. Each porphyrin molecule can be clearly recognized as a bright spot. The porphyrin molecules are adsorbed flat-lying on the Ag surface. As it can be discerned in this figure, the well-ordered bright spots present a square arrangement. The molecular adlayers are two-dimensionally well organized. A unit cell is superimposed in Fig.5.2.4. The structure of Zn-TPP and Co-TPP is the same on this substrate: a square arrangement with the lattice arrangement of 1.4 nm and an angle of 90°. For the Zn-TPP, in Fig.5.2.4a, a slight dislocation due to the thermal drift of the STM can be observed. The same arrangements were also reported for Co-TPP on Au(111) [55]. This corroborates the assumption that intermolecular interactions are the driving force for the particular ordering.

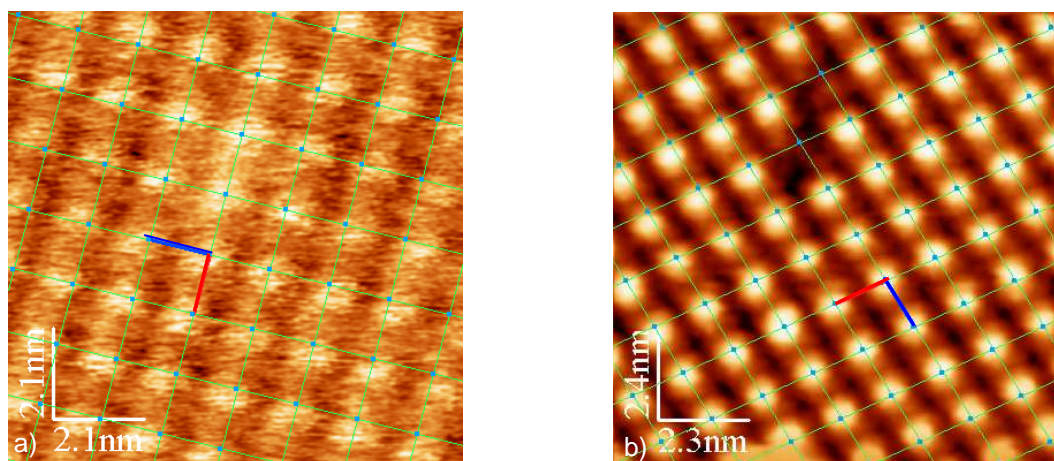


Fig. 5.2.4 Molecular resolution for the Zn (left) and Co (right) porphyrin molecules. The bias voltage is the same for the two STM images, with a value of -1.2 V, and the tunneling current 0.2 nA for the Zn-TPP and 0.3 nA for Co-TPP.

Even though the ordering behavior of Co-TPP and Zn-TPP was found to be exactly the same, the appearance of the two molecules in STM differs, i.e., the center of Co-TPP is brighter as the center of Zn-TPP, as observable in Fig.5.2.4. Fig.5.2.5 shows profile lines where the differences for the Z values are observable.

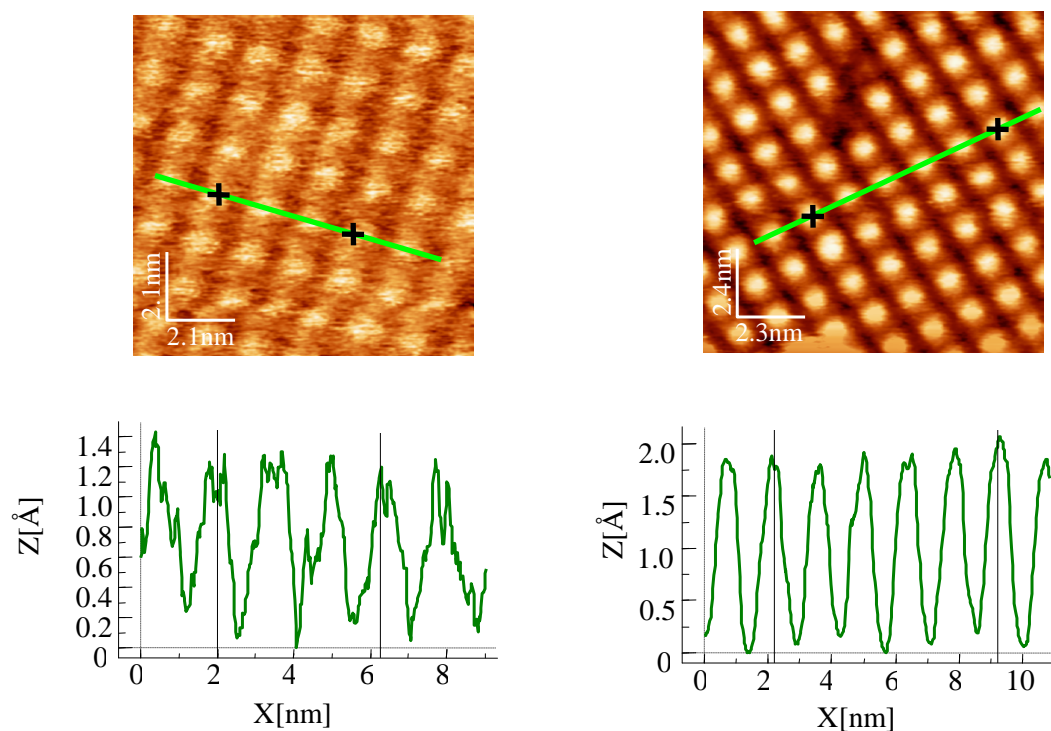


Fig. 5.2.5 Differences in profile height for the two different porphyrin molecules.

In Fig.5.2.6 space filled models of a typical metal(II)-porphyrin complex drawn to scale and place by hand over the STM image were shown. The value of 1.4 nm for the approximate lattice constant has been obtained based on this procedure. The different contrast observed in Fig.5.2.6a as compared to the previous images is due to the changed bias polarity. By positive bias, it is expected that the molecule to be imaged by STM as four lobes, corresponding to the four phenyl groups, which determine the shape of the molecule.

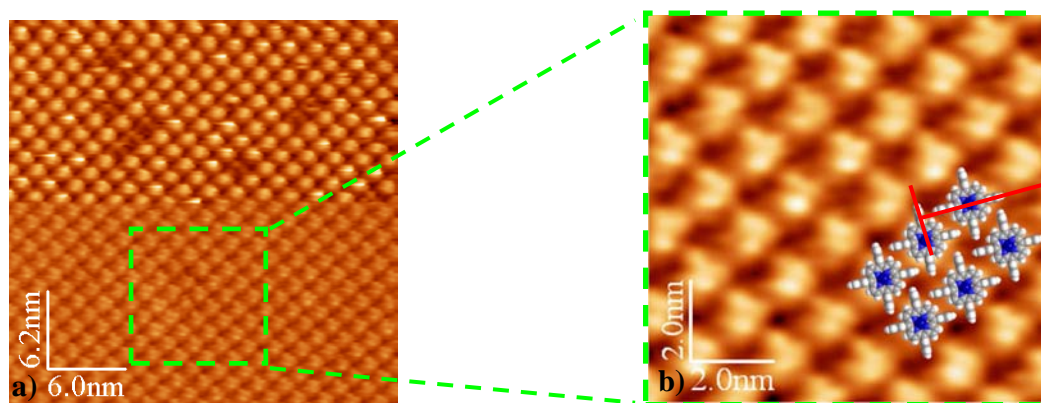


Fig.5.2.6 a) STM topography of Co-TPP molecules and b) model of metaloporphyrin molecules inserted into STM image. The tunneling parameters were 0.3 nA and a voltage of 1.2 V (the contrast from Fig.5.4.6 a) is the result of the changed polarity for bias).

The pattern of the four lobes allows the determination of the molecular arrangement. The intermolecular interaction involving the aromatic phenyl rings are a key to understand the molecular arrangement. The review article by E. Meyer et al. [86] combined and summarized the knowledge gained from different approaches—biological studies, molecular recognition studies with artificial receptors, crystallographic database mining, gas-phase studies, and theoretical calculations. The arrangements for the aromatic rings are for example the parallel-displaced (stacking) or edge-to-face (T-type). In the parallel alignment, two aromatic partners, one bearing strong electron-donor and the other strong electron-acceptor groups, form parallel stacking complexes. The edge-to-face aromatic interaction is an interaction, in which the partial positive charge on the ring hydrogen of the upper (edge) tetra phenyl interacts favorably with the partial negative charge above the aromatic ring of the lower (face) tetra phenyl. The molecular models have been used to develop a simple

unit cell for the highly ordered porphyrin monolayer. This arrangement of porphyrins shows a square arrangement. As indicated by the red lines in Fig. 5.6.2b the interaction for the proposed model is of T-type.

As discussed above, the assembly structure is dominated by intermolecular T-type interactions. It is known that the growth of organic molecules on a solid substrate is determined by molecule–molecule and molecule–substrate interactions. Weak molecule–substrate interactions often lead to epitaxial growth of molecular films, with less distortion of the symmetry from the bulk crystals. As for strong molecule–substrate interactions, the symmetry of the substrate is known generally to affect the symmetry of the epitaxial organic film, leading to distortion of the molecular lattice to achieve optimal alignment or commensurability with the substrate lattice.

For all TPP molecules, the same long-range molecular order could be observed: a square lattice with a molecule-molecule distance of 1.4 nm. Therefore, the observed square symmetry is a strong indication of relatively weak molecule–substrate interaction.

5.3. Arrangement of TTBPP molecules

One possibility to modify the porphyrin macrocycle/metal-substrate distance is to use molecules with different substituents. A porphyrin derivate, which apparently exhibits a larger porphyrin macrocycle/metal-substrate distance, is the cobalt-di-tert-butyl-phenyl porphyrin (Co-TTBPP). This is realized by the attachment of two tert-butyl (TB) groups to the 3 and 5 positions of the phenyl rings of the Co-TPP. Consequently the electronic interaction of the porphyrin system with the substrate is sterically decoupled by the di-butylphenyl (DBP) substituents [1]. As described in detail in chapter 4.1, the TTBPP molecule in its adsorbed state, as observed by STM, is mostly characterized by four protrusions in a rectangular arrangement corresponding to the four upper TB groups. For the internal conformation of TTBPP, the rotation angle around each of the four phenyl-porphyrin bonds is the predominant conformational factor. The porphyrin-phenyl bond of the TTBPP is a single (σ) bond

that does not participate in the conjugated electron system, owing to the weak overlap of the π levels [50].

Depending on the substrate, different molecular arrangements and intramolecular conformations can be found for Me-TTBPP [54].

The standard thermal sublimation (as described in chapter 3.3.2) was applied to prepare the Co-TTBPP in the monolayer regime. Fig.5.3.1 shows a STM image of a porphyrin layer prepared in such a way.

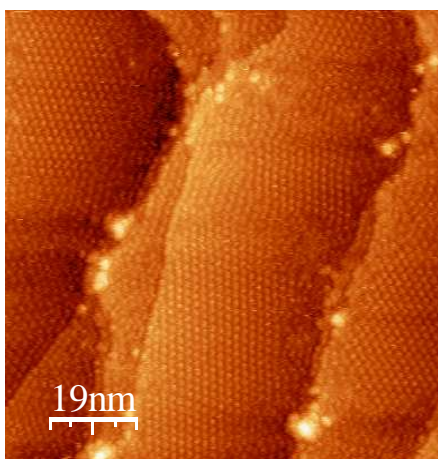


Fig.5.3.1 STM topography of a self-assembled Co-TTBPP film on Ag(111) (tunneling parameters $I_{set} = 0.8$ nA, $U_{gap} = -0.7$ V; scan range: 95 nm x 95 nm).

The image shows domains of ordered porphyrin molecules on silver terraces. Apparently the arrangement of the molecules is hexagonal, in contrast to the known square arrangement for the smaller Me-TPP molecules.

The STM images in Fig.5.3.2 exhibit altogether three different arrangements for the molecules as indicated by the labels Hex A, Hex B and Square.

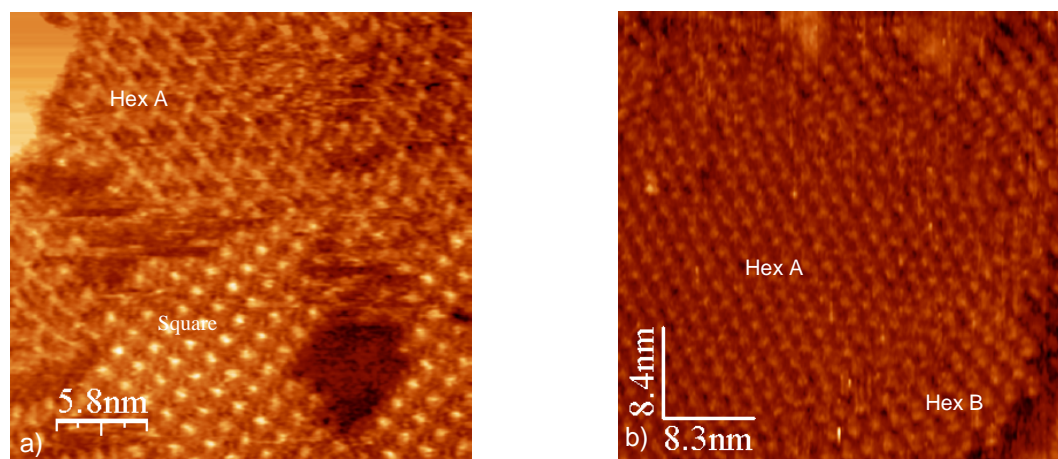


Fig.5.3.2 Topography of Co-TTBPP molecules showing the coexistence of the three different molecular arrangements.

This is again in contrast to the Co-TPP molecules, where only the square configuration have been observed. In the framework of the work at hand, three different molecular arrangements were found for the Co-TTBPP: a square and two hexagonal phases, designated as hex A and hex B. The image in Fig.5.3.2a is showing the corresponding domains with different conformations inside the Co-TTBPP film.

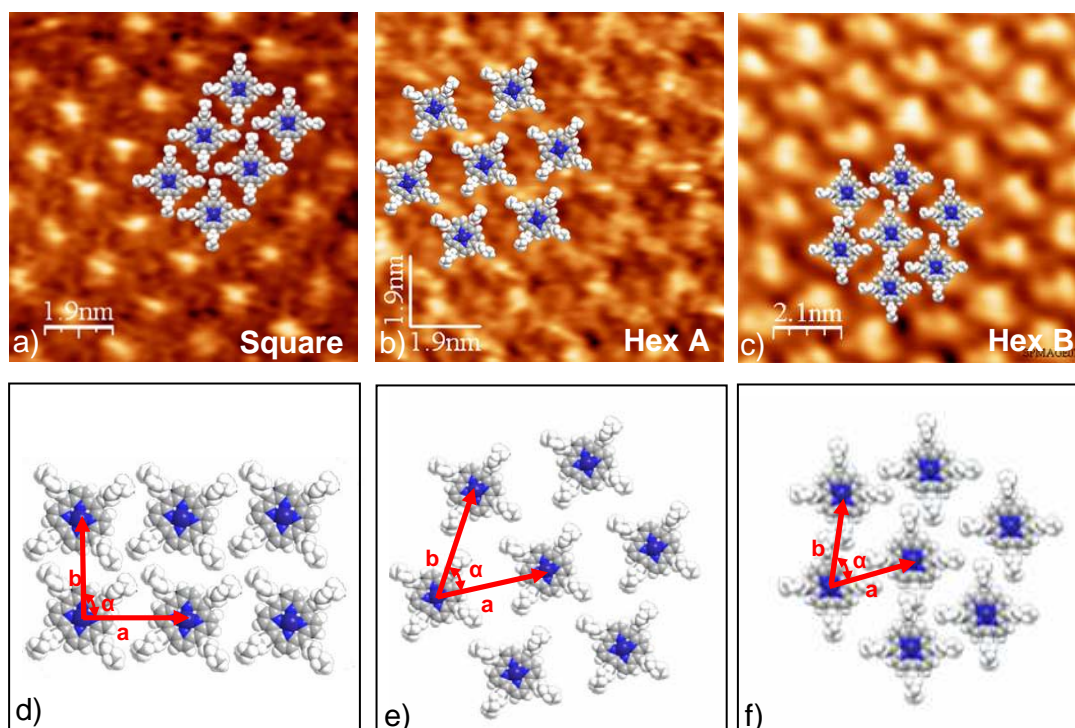


Fig.5.3.3 Square, Hex A and Hex B arrangements for porphyrin molecules and the proposed models drawn to scale and placed by hand over the corresponding STM images.

In Fig.5.3.3 zoom-ins of STM images of the above described three phases are shown with the corresponding suggested molecular models. In the STM images, a bright spot is identified at the center of the molecule. The contrast can possibly be attributed to the half filled d_z^2 orbital of Co(II). The d_z^2 orbital has the main contribution to the tunneling process.

The Square phase as shown in Fig.5.3.3a is characterized as follows: both lattice vectors are 1.6 nm with an angle of 90° between the two vectors.

For the image in Fig.5.3.3b, the molecular arrangement is **hex A**, with an average length of approximately 2.2 nm for both adsorbate lattice vectors. The angle between lattice vectors is of 60° . The **hex B** molecular arrangement shows an average length of 1.9 nm for both lattice vectors, also with an angle of 60° .

At negative bias, where the central metal atom is observed as a main feature (instead of the four lobes for the side groups), it is difficult to deduce exact models for the molecular arrangements. Due to this basic uncertainty, no intramolecular deformations and rotational motion of the upper TB groups could be taken into account for the proposed models. In Fig.5.3.3d-f, the corresponding molecular models are shown.

In a follow up investigation by Florian Buchner et al. (article in preparation) [87], the existence of the four clearly distinguishable ordered monolayer phases of Co-TTBPP will be reported. In this study, the changes in the internal conformation are taken into account. Two categories of the deformations from the ideal conformation have been proposed. The twisting rotation of the phenyl rings around the σ -bonds between the phenyl rings and the porphyrin macrocycle is one deformation. The other is tilting of the phenyl rings with the respect to the porphyrin macrocycle. Both tilting and twisting of the phenyl rings is required to get a good correlation between the shape formed by the centres of the tert-butyl groups inside the model and the intensity maxima of the four bright lobes per molecule inside the STM topography. The high-resolution STM images obtained by a positive bias offer enough information to fit these deformations to the experimental data. It is also observed that for the **hex A** structure the unit cell is characterized by the two lattice constants $a = 2.30 \pm 0.5$ nm and $b = 2.07 \pm 0.10$ nm, with an enclosed angle $\alpha = 65^\circ$ and a 2D molecular density of $\rho = 0.24$. For the **hex B**, which is a clear-cut closed packed hexagonal structure, the unit cell parameters are $a = b = 1.89 \pm 0.05$ nm, $\alpha =$

60° and $\rho = 0.31$ molecules/nm². The Square phase has an average length of the lattice vectors of 1.60 ± 0.06 nm and an angle of $90 \pm 3^\circ$, with a molecular density of $\rho = 0.39$ molecules/nm². The fourth arrangement described for the molecules is the herringbone structure. The parameters for the unit cell are the same as for the hex B structure. The molecules inside this herringbone structure exhibits in addition to the four bright lobes four additional slightly dimmer protrusions.

The twist angle (dihedral) and the tilt angle thus represent a set of parameters used to describe the conformation of the single molecules associated with the different long range orders. Using these parameter models are purposed for this three molecular arrangements.

The three conformations found for the Co-TTBPP show significant mobility. In some STM images, an exchange of molecules between the three conformations was recognized. Such a transition of molecules from a conformation to another was studied in the following by imaging the same area. Fig.5.3.4 shows two subsequent images where one can observe an increasing number of molecules that arranges gradually in the square phase.

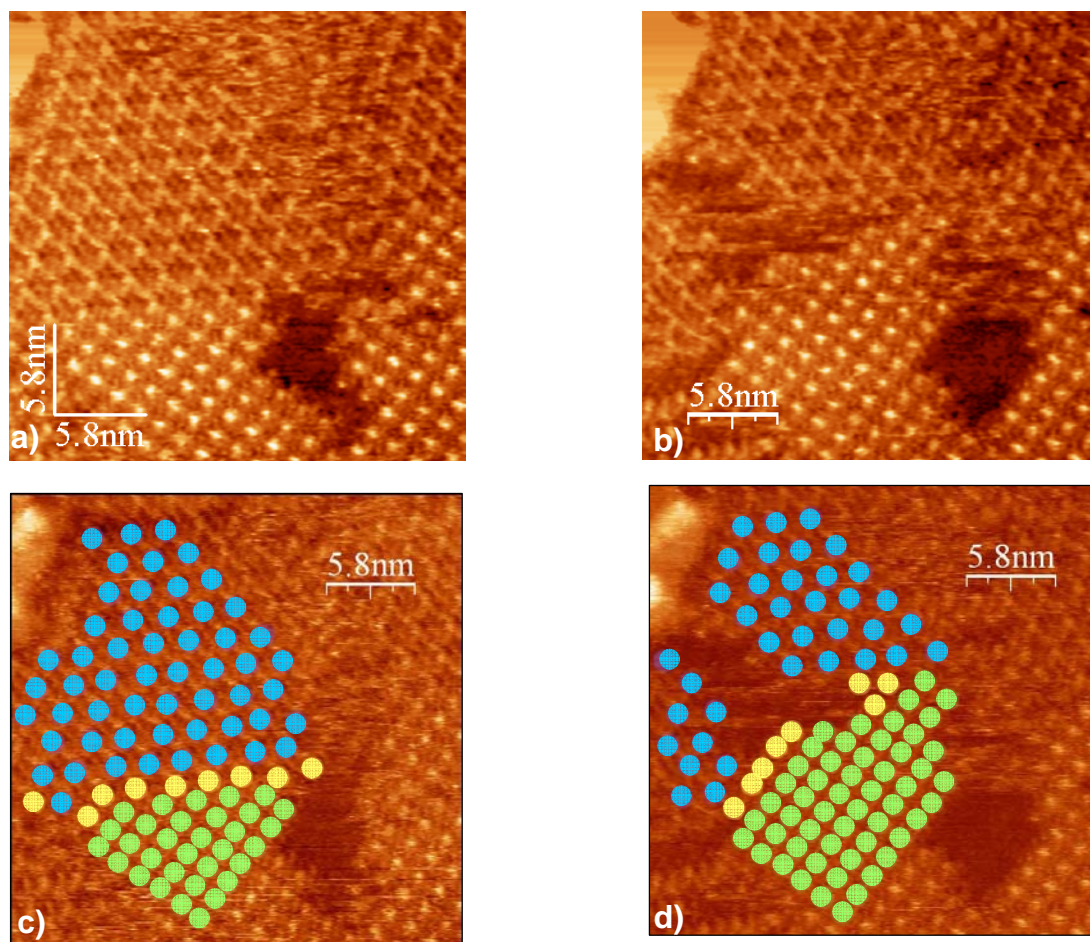


Fig.5.3.4 (a), (b) STM images of Co-TTBPP on Ag(111) imaging the transition of structure in a confined area.(scan range 25 nm x 25 nm, $I_{set}=0.3\text{nA}$, $U_{gap}=-1.2\text{V}$) and (c), (d) same images illustrating the different type of structure.

In Fig.5.3.4a-c, the square and the hex A structure are delimited by a grain boundary. The STM images were acquired again at a negative bias voltage. Therefore, the bright spots are interpreted as the centers of the molecules. The molecules are counted and marked in a confined area with different colors. The color code is as follows: blue for hex A arrangement, green for the Square arrangement and yellow for the molecules with no definite assignment. The sum of the molecules is the same for the two examples: 99 molecules. In Fig.5.3.4c, the number of molecules assigned to the Square conformation is 32, for the hex A structure 58 molecules are counted and there are nine molecules with no definite assignment. In Fig.5.3.4d the number of molecules in the Square arrangement is increased to 54 (22 molecules more) and the number of molecules in the hexagonal arrangement is decreased to 37 (21 molecules

less). The number of the molecules with no definite assignment is changed to eight. The time sequence in this particular case demonstrated that an increasing number of molecules are arranged gradually in the square phase.

As shown in Fig.5.3.5, the individual molecules can be also imaged as four lobes. Fig.5.3.5a shows the topography of an island, where the conformational identification of the Co-TTBPP is observable. Fig.5.3.5b shows a zoom in Fig.5.3.5a. In Fig.5.3.5b, marked with the green circle, the four di-tert-butyl phenyl groups are indicated. The four lobes of each molecule in the STM images should correspond to the four upper tert-butyls and they are arranged in a square.

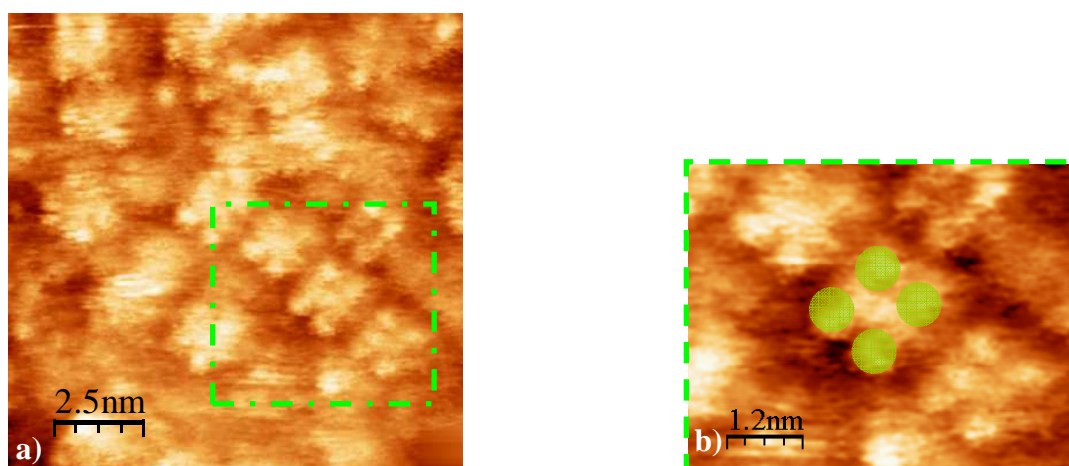


Fig. 5.3.5 Imaging single Co-TTBPP molecule ($12,5 \times 12,5 \text{ nm}^2$, -1.2 V and 0.3 nA).

The molecular arrangement and the conformation of Co-TTBPP on Ag(111) were shown.

5.4. Identification of distinct features in Co-porphyrin layers

For the Co-porphyrin layers deposited on Ag(111), certain features are observed in the STM images. A significant portion of an ordered monolayer of the commercial available Co-porphyrins appear as depressions or “pits” at negative bias voltages around -1 V , as can be seen, e.g., in Fig.5.4.1. Similar features are also

occasionally reported in the literature and interpreted as missing molecules or impurity molecules. Scuderio et al. [76], consider these pits as impurity molecules and speculate that these features are 2H-TPP molecules. These pits are also considered as missing molecules from Yoshimoto et al. [55]. Hereby, adlayers of Co-TPP and Cu-TPP formed on a Au(111) electrode by immersion into a benzene solution containing either Co-TPP or Cu-TPP were investigated in 0.1 M HClO₄ by cyclic voltammetry and in situ scanning tunneling microscope. The mentioned interpretations for the observation of depressions within ordered molecular layers are candidates to explain the observation of pits in Co-TPP on Ag(111). In the work at hand, this issue was targeted experimentally with different methods to find the evidence that will lead to a consistent picture of the nature of these pits.

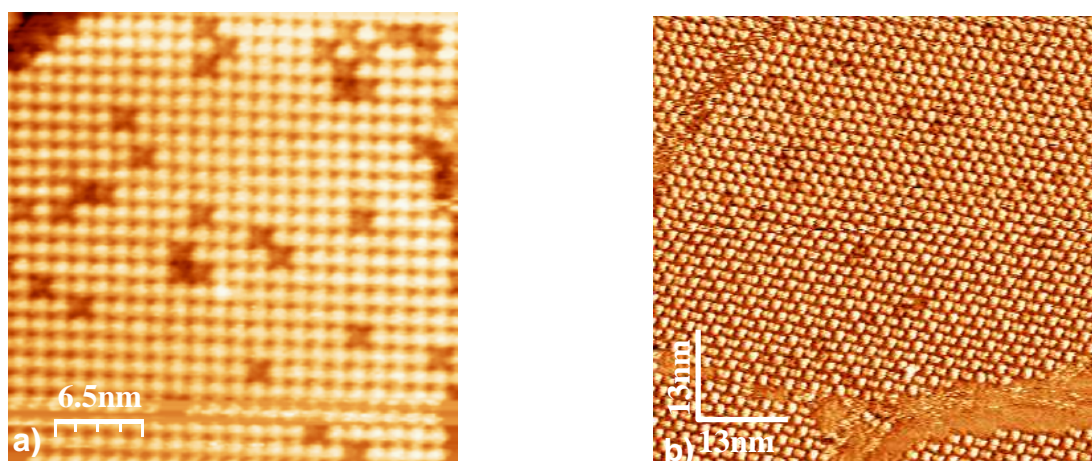


Fig.5.4.1 STM images of Co-TPP in a) and Co-TTBPP in b). The images were taken under scanning condition of $U_{gap} = -1.2V$ and $I_{set} = 0.3nA$. The scan ranges are $32.7 nm \times 32.7 nm$ for a) and $67 nm \times 67 nm$ for b).

The STM images in Fig. 5.4.1 show Co-TPP respective Co-TTBPP on Ag(111) in their well ordered molecular arrangements. In different positions, the pits can be identified as the darker spots in the STM images.

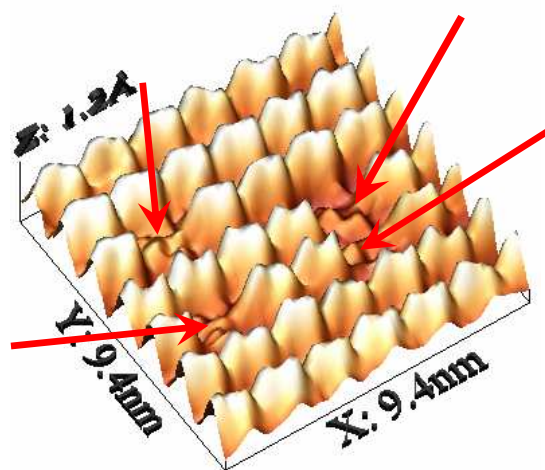


Fig. 5.4.2. STM 3D plot of Co-TPP molecules with pits. The arrows indicate the position of the pits.

In the 3D plot shown in Fig.5.4.2, the existence of the pits is even more apparent. All the STM images shown so far were scanned with the tunneling parameters $I_{\text{set}} = 0.3 \text{ nA}$ and $U_{\text{gap}} = -1.2 \text{ V}$. For these STM settings, the pits were always observed. After a statistical analysis the percentage of the pits was estimated to be 7-10 % in Co-TPP and $< 5\%$ in the case of Co-TTBPP on Ag(111). This difference is apparent in Fig.5.4.1 where topographies of the two different porphyrins are shown.

Fig.5.4.3 shows the same region of the sample, imaged with different bias voltages in STM. The dark spots on the left image identified as pits are observable at a voltage of -1.2 V , but are not seen at -0.1 V .

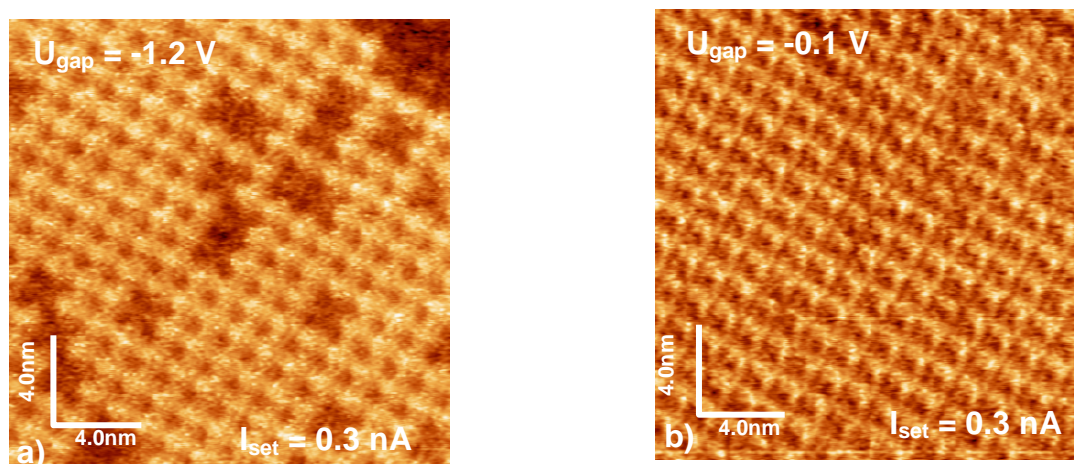


Fig.5.4.3 Two STM micrographs imaging the same area of an ordered layer of Co-TPP with different bias voltages.

Comparing the STM images acquired at the same region with the usual bias voltage of -1.2 V with a decreased voltage set point of -0.1 V reveal that the contrast of the pits vanished and the molecular arrangement seems to be defect-free at the lower bias voltage. Therefore, the possibility of missing molecules is ruled out.

Since the observed pits are apparently no missing molecules, additional investigation of the electronic structure, in particular of the density of state of Co- and 2H- porphyrin layers by means of ultraviolet photoelectron spectroscopy (UPS) were conducted in our group by M. Gottfried and coworkers.

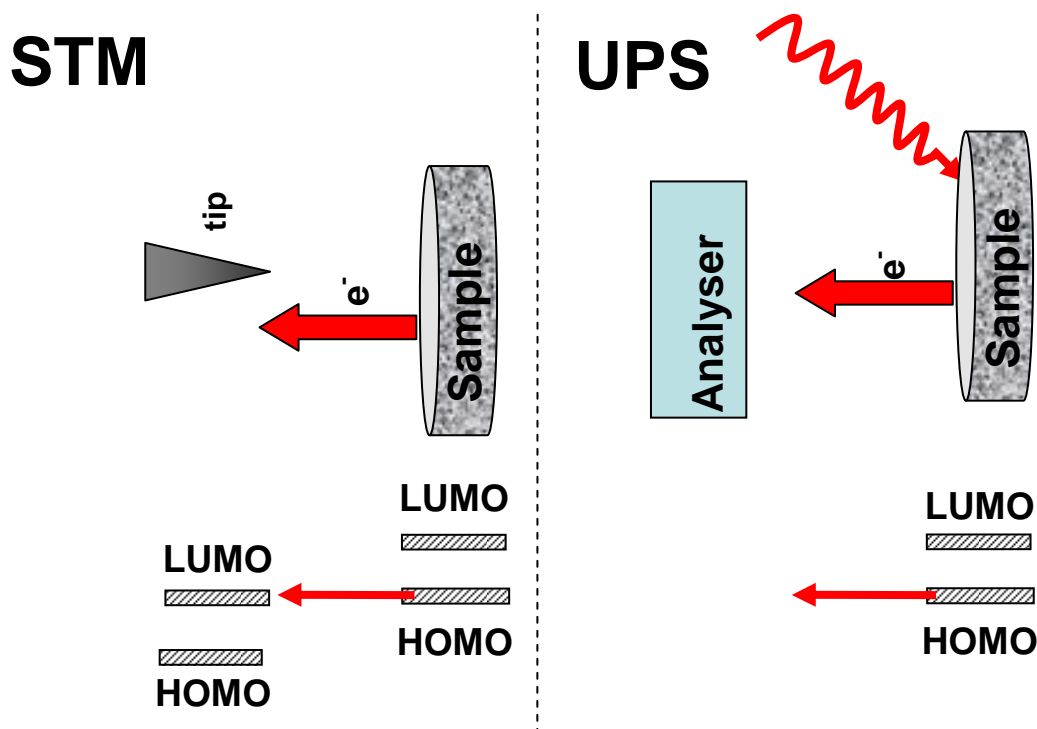


Fig.5.4.4 Scheme for STM and UPS.

In Fig.5.4.4, the interrelationship of the STM and the UPS experiment is sketched. Both schemes were already presented in the Experimental section, chapter 2.1.1 and 2.4. In both cases, electrons from the HOMO states are emitted from the sample. In UPS, the kinetic energy of the emitted electrons close to the Fermi edge is analyzed thus giving direct access to the density of states (DOS) of these electrons. The DOS on the other hand can reflect the electronic and chemical interaction between the molecules and the substrate. In respect to the observation of the pits, special attention has to be paid to the UPS signals near the Fermi edge, because this region is also accessible with STM. In the STM, the tunneling current is determined by integration over all DOS inside an energy interval opened by the applied bias voltage.

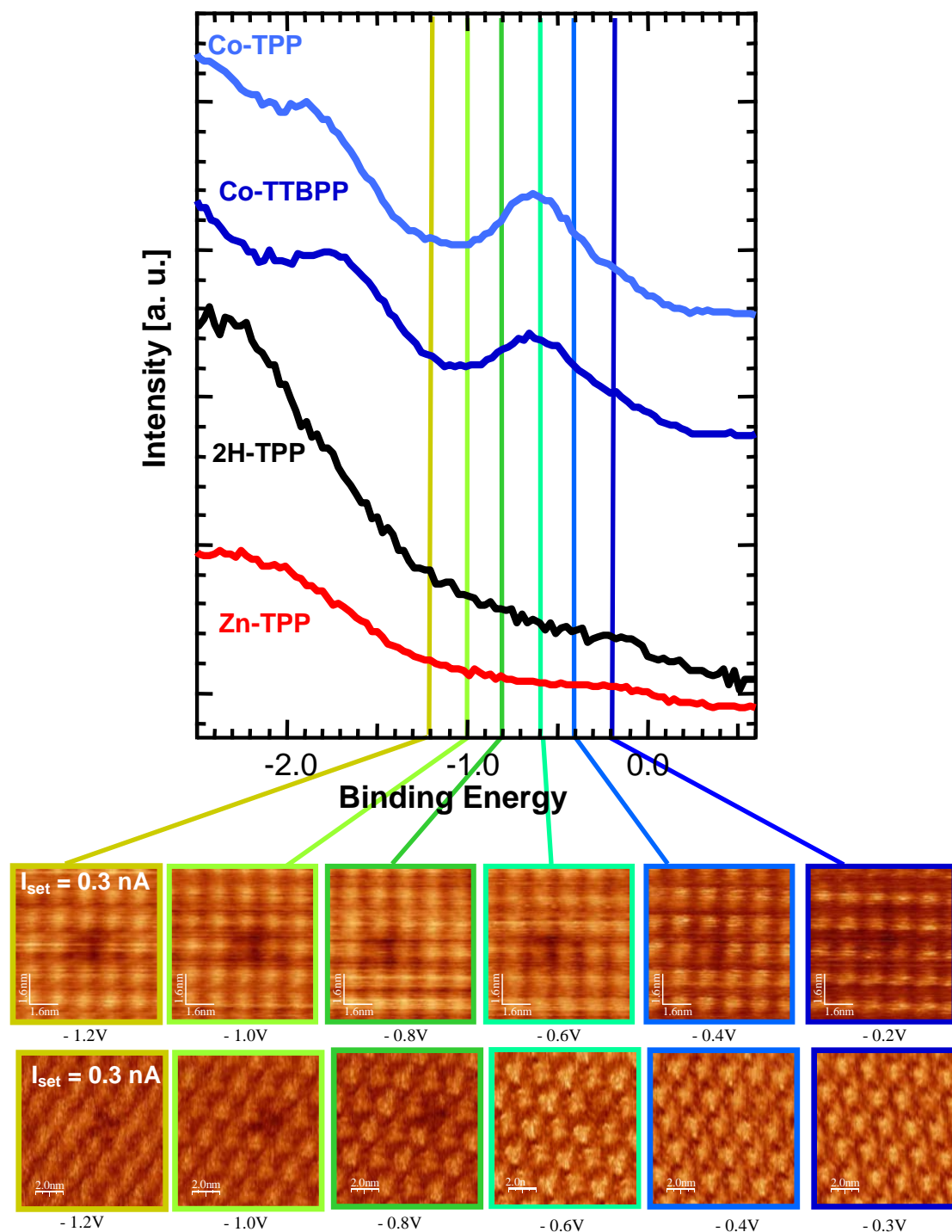


Fig. 5.4.5 Comparison between UPS and STM measurements. Upper bias series of STM images show Co-TPP and bottom series Co-TTBPP molecules in their corresponding ordered molecular arrangements. The respective bias voltage position in the UP spectra are indicated with the colored vertical lines.

Fig.5.4.5 shows a comparison between the STM and the UPS measurements. The contrast of the pits is vanishing by varying the bias from $U=-1.2\text{V}$ to $U=-0.1\text{V}$.

For the STM images, always the same region was scanned, with the same speed of 100ms/line.

The UPS data shown in the work at hand were acquired by Thomas Lukasczyk et al. [88]. In Fig.5.4.5, UP spectra for Co-TPP, Co-TTBPP, Zn-TPP and 2H-TPP are shown in the energy range of -0.6 eV to -2.5 eV e.g. near the Fermi edge. The monolayer UP spectra of Zn-TPP and 2H-TPP are basically featureless near the Fermi edge. For the Co-TPP, the monolayer spectrum in the shown energy range is dominated by a signal located at a -0.6 eV below E_F . The peak can be attributed to the electronic interaction of the coordinated Co ion in the metalloporphyrin with the Ag surface [88]. For the Co-TTBPP monolayers an analogous signal was observed. The peak is located at a -0.7 eV below E_F . The difference of 0.1 eV for the peak positions of the two Co-porphyrins is small, but significant and reproducible. The monolayer UP spectrum of 2H-TPP shows no additional features around -0.6 eV . This one evidence for the peak at -0.6 eV (Co-TPP) respective -0.7 eV (Co-TTBPP) are due to the metal-surface interaction. The possibility that the Co-TPP molecules partly decompose on the surface and the Co atoms adsorb directly on the Ag surface and caused the peak at -0.6 eV was excluded in the work of Lukasczyk et al. [88].

In Fig.5.4.5, it is apparent that the contrast of the pits as observed in the STM images starts to fade at bias energies round -0.6 eV . This effect can be understood by identifying the pits as 2H-TPP. The contrast in STM is determined by the integration of all DOS and in the UP spectra by the integration right from the corresponding marked bias voltage. In the STM, for energies more negative than -0.7 eV the peaks of the metal ion-substrate interactions contribute fully, thus enhancing the contrast of Co-porphyrins and 2H-porphyrins. At energies, where these peaks do not contribute to the integration, e.g., at 0.1 eV the contrast consequently vanishes, since the integrals over the DOS for Co-TPP/Co-TTBPP and 2H-TPP/2H-TTBPP obviously converge.

To test the hypothesis that the observed pits are due to 2H-porphyrins, a mixture of roughly 50 % Co-TPP and 50 % 2H-TPP was prepared by Dr. Norbert Jux. A layer of this material was then prepared in the same way (thermal sublimation) as the “pure” compounds. Fig.5.4.7 shows two STM images of a layer of the described porphyrin mixture. On the first glance, it becomes clear that the number of pits increased dramatically in the mixture layer compared to the Co-TPP layer. A statistical analysis reveals an increase of the pits from 7-10 % in the Co-TPP layer to 40-55% in the mixture layer. These values obviously fit very well to the picture

established so far, thus supporting the hypothesis that the pits can be identified with 2H-TPP.

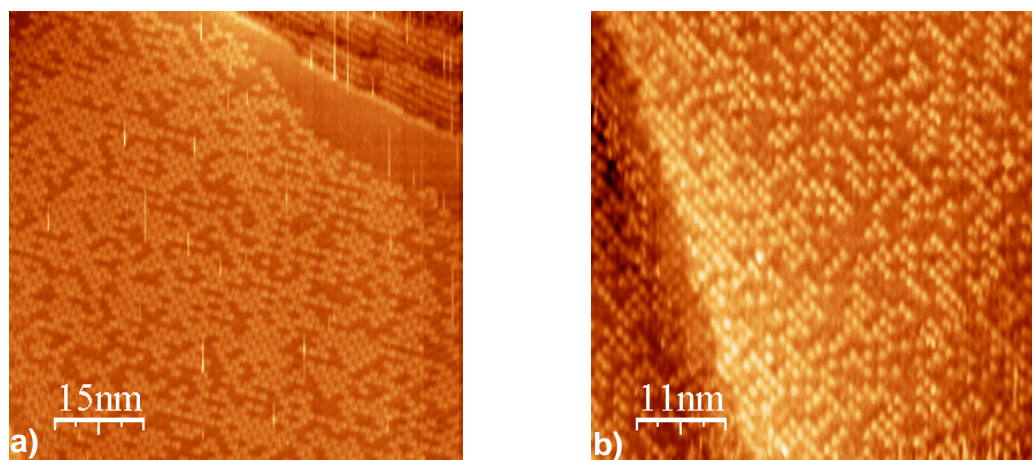


Fig. 5.4.6 STM topography of 2H-TPP and Co-TPP mixture. (Scan ranges a) 76.6 nm x 76.6 nm; b) 47.8 nm x 47.8 nm; c) 57.2 nm x 57.2 nm and tunneling parameters: bias voltages -1.2 V for a and -1.0 V for b, c; tunneling current 0.3 nA).

Additional evidence could be given by high-resolution imaging of a corresponding area of the 2H-TPP and Co-TPP mixture. The image in Fig.5.4.7 is a high-resolution STM image obtained for the porphyrin mixture. Again, the Co-TPP molecules appear as the bright spots in the topography whereas the pits appear as a central cavity with a surrounding of four bright spots. These bright spots can be identified with the four phenyl rings attached to the porphyrin macrocycle in the case of a TPP. The central depression indicates the absence of the central metal ion thus the whole feature (central cavity plus four protrusions) can be identified with a 2H-TPP.

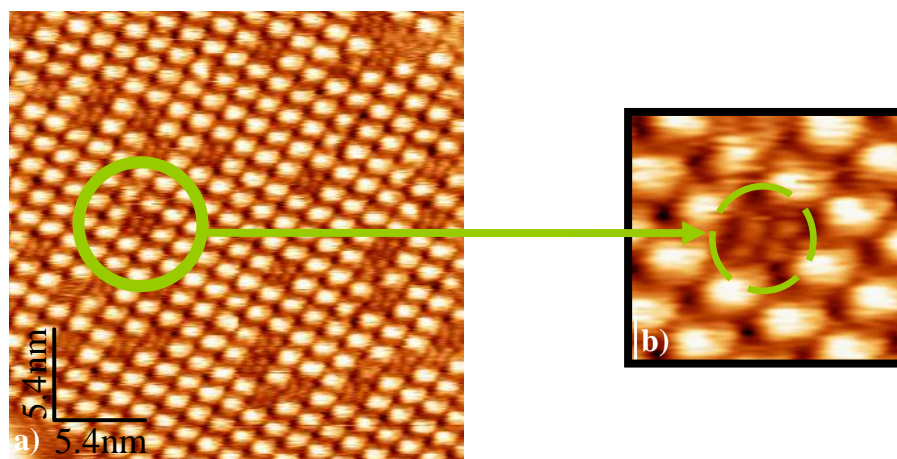


Fig. 5.4.7 High resolution image of 2H-TPP and Co-TPP mixture. The zoom image shows the 2H-TPP molecule. ($I_{set} = 0.4$ nA, $U_{gap} = -1.1$ V; scan range 26.8nm x 26.8 nm).

Summarizing the compelling evidence obtained by STM and UPS, it can be concluded that the features denoted as pits within Co-porphyrin layers are 2H-porphyrins. Additional information, in this case Nuclear Magnetic Resonance (NMR), obtained by Dr. Norbert Jux confirms that the commercially available Co-TPP (with a specified purity of 98%) is contaminated with 2H-TPP in the range of 10 %, which is in good agreement with the STM experiment, where a percentage of 7 % of 2H-TPP was observed. This finding evidences that the observed 2H-TPP (pits) in the Co-TPP layer originate from the purchased material itself.

Interestingly the observed layers of Zn-TPP never exhibit features comparable with the pits in e.g. Co-TPP. If one assumes the likely case that the Zn-TPP also contains some portion of 2H-TPP this would possibly not have a strong contrast in a STM image since the shape of the DOS as observed in UPS (Fig. 5.4.5) is very similar to the one of 2H-TPP. Especially the UP spectra for Zn-TPP exhibit no peak close to the Fermi edge.

Summing up, a consistent picture of the contrast mechanisms for different porphyrins in STM could be established which also allowed the identification of certain features namely pits in Co-porphyrin layers as 2H-porphyrins.

5.5. 2D-Chirality of non-chiral molecules

Chirality is a very important phenomenon in nature. The chemical and biological properties of molecules depend not only of the nature of their constituent atoms but also on the space orientation of the atoms. Advances in scanning probe microscopies make it possible to probe chiral phenomena at surfaces at the molecular level. These methods have been used to determine the chirality of adsorbed molecules [89, 90], and to provide direct evidence for chiral discrimination of adsorbates into extended enantiomerically pure overlayers [89, 91].

Chirality phenomena associated with molecular species and arrangements in low-dimensional systems have attracted strong interest over the past years [77, 92]. Moreover, molecules that are achiral in three dimensions may become chiral upon adsorption due to the reduced symmetry. It is a challenging task to determine the structure or elucidate the formation of low-dimensional chiral species. Molecular surface structures often show important stereochemical effects as, aside from truly chiral molecules, a large class of so-called prochiral molecules becomes chiral once confined on a surface with an associated loss of symmetry.

In the present work, STM measurements revealed chiral properties in the case of Co-TTP molecules.

After deposition, the molecules assemble readily into well-ordered 2-D supramolecular networks with square unit cells of comparable size, where these effects have been observed (see chapter 5.2). Fig.5.5.1 shows molecules of Co-TPP deposited on the silver surface.

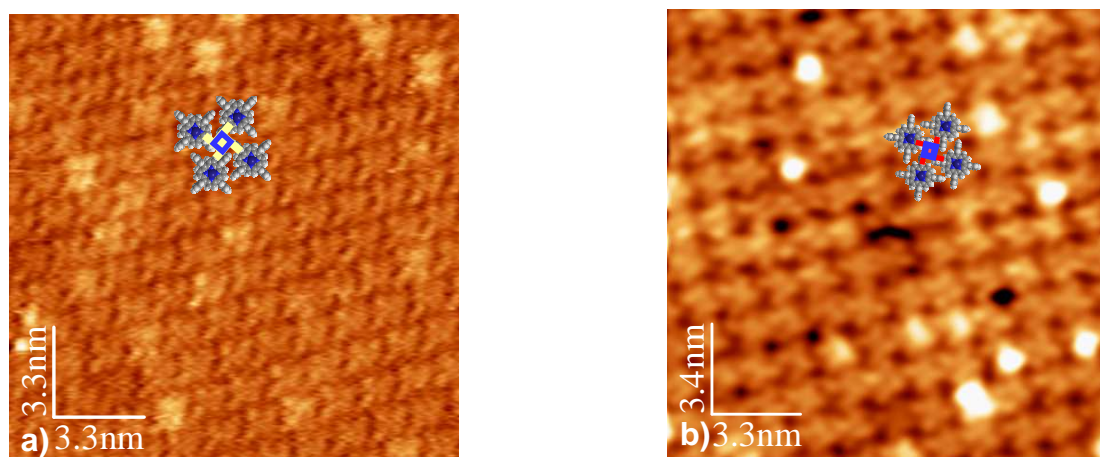


Fig. 5.5.1 High resolution STM images of ordered Co-TPP molecules. Windmill model that fit in the case for Co-TPP (tunneling current constant for the two images at 0.3 nA with the corresponding bias voltages: a - $U_{gap} = 0.34$ V and b - $U_{gap} = 0.62$ V).

In contrast to most of the previously shown STM images in this work, the images in Fig. 5.5.1 are scanned with a positive bias voltage. This results in an altered contrast, where the porphyrin molecules appear as four lobes to be identified with the phenyl groups. Because both the position and the orientation of these groups can be seen, the exact configuration of the molecules can be determined. The dominating motive is considered a windmill-like arrangement of four molecules. This windmill motif can be constructed in two mirror-image forms with an opposite sense of rotation.

The windmill models in Fig. 5.5.1 indicate two different molecular assemblies with distinguishable 2D chirality. The molecules in Fig. 5.5.1 a are arranged in a way that the corresponding windmill shape exhibits a kind of clockwise sense of rotation, which is denoted as left-handed. The opposite observation, e.g., counterclockwise orientation can be made in Fig. 5.5.1 b and is consequently denoted as right-handed. The colors code is yellow for left-handed and red for right-handed. Thus, the images in Fig. 5.5.1 evidence the existence of domains with opposite 2D-chirality.

5.6. Investigating the multilayer regime

To investigate the multilayer regime, different experiments were performed. There are experiments realized on the Ag single crystal with different orientation (100 and 111) and with different porphyrins molecules.

The first experiment to be described is the investigation of a Ag(100) surface with multilayers of free base tetraphenyl porphyrin (2H-TPP) by means of QMS and LEED; it was conducted in advance of the STM measurements to test some fundamental aspects of the preparation and investigation of porphyrin films in UHV. This experiment was performed in a different UHV chamber equipped with a SPECTALEED optics - a precision instrument providing $> 250 \text{ \AA}$ transfer width (at 100 eV), and particularly bright LEED patterns, a QMS and a home-built evaporator, which has the same construction principle as the one used for the previously described experiments. With this equipment, QMS measurements were made to determine the evaporation temperature of the porphyrin molecules. The evaporation temperature was established to be 350° C after the QMS experiments.

Here, the first LEED experiments and the reflexes for multilayer (a) and monolayer (b) of porphyrin deposited on Ag(100) are shown in Fig. 5.6.1.

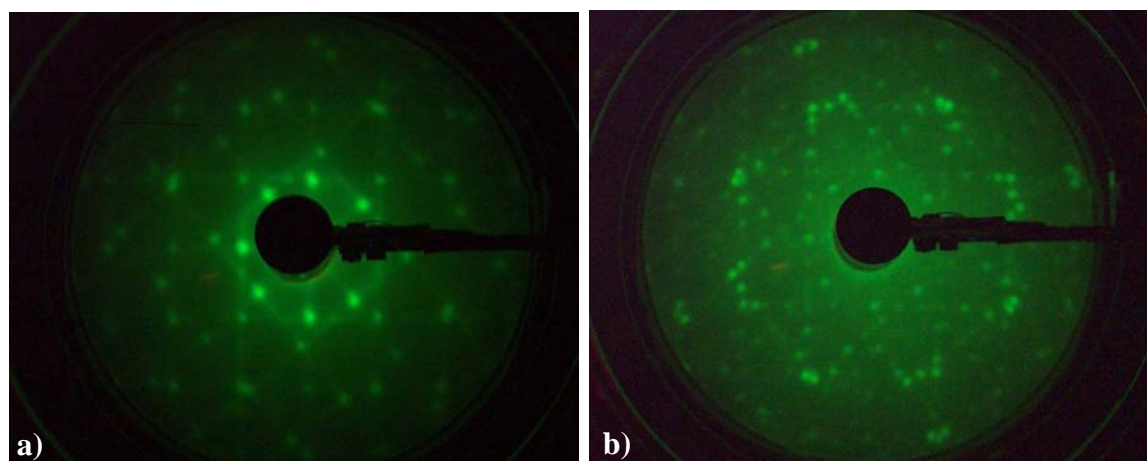


Fig. 5.6.1 LEED patterns for porphyrin molecules for the multilayers regime (a) and monolayers regime (b). The beam voltages were around 18.7 eV; the sample temperature was 370 K for the multilayer pattern and 87 K for the monolayer pattern.

This set of experiments, QMS combined with LEED, offered the first information about the temperature range, where the porphyrin molecules can be evaporated. The LEED images in Fig. 5.6.1 evidence long range order in the porphyrin films. Therefore, it has demonstrated that silver is a suitable support for the porphyrin molecules to form ordered phases. The experiments were stopped, after LEED patterns for the monolayers regime were obtained.

In the next experiments porphyrins on the Ag(111) sample were investigated by STM. The experiments were conducted after different exposure times and with different evaporation temperatures of the Knudsen cell. After each deposition, the sample was transferred from the preparation chamber to the main chamber for STM studies. The STM images in Fig.5.6.1 show the surface of the Ag(111) crystal after 10 min deposition of 2H-TPP molecules with the evaporator at 330°C . The STM data was recorded with different scan directions as indicated by the arrows in the corresponding images in Fig. 5.6.2.

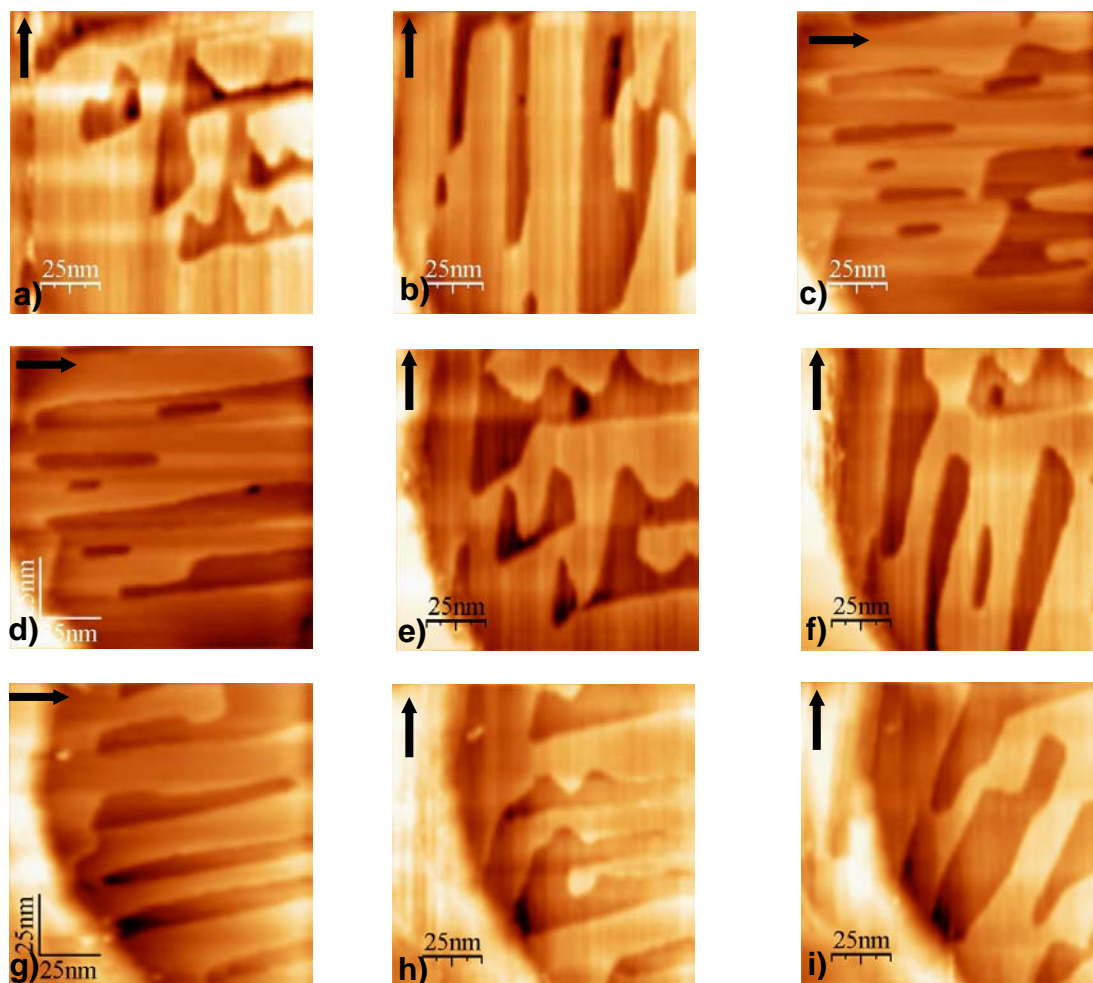


Fig. 5.6.2 Series of topographic images acquired in a time total interval of 37 minutes. The scan area for all the images is $124 \times 124 \text{ nm}^2$. The tunneling parameters were also kept constant at: $I_{\text{set}} = 0.3 \text{ nA}$ and $U_{\text{gap}} = -1.2 \text{ V}$.

One observes the formation of stripy features parallel to the scan direction of the STM. The features were not observed on the clean Ag(111) and must consequently be due to the deposited porphyrins. Obviously, the porphyrins enhance tip induced changes of the apparent surface topography. In the images from Fig.5.6.2, more than two different layers are distinguishable. Measuring the height of the layers, the obtained information can clarify whether these features are terraces or steps of silver or are directly related to deposited porphyrins. Fig.5.6.3 shows a profile extracted from the image in Fig 5.6.2c.

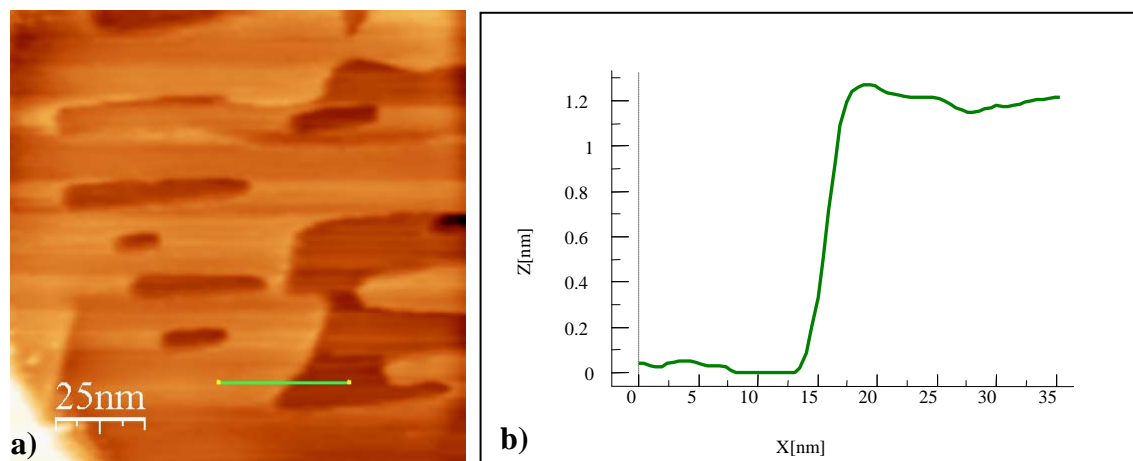


Fig. 5.6.3 A profile line that shows the terrace height in the STM topography.

The measured height is roughly 1.1 nm, a value that is much higher than the measured (see chapter 5.1) step height for the silver crystal. Together with the high mobility (as evidenced by the tip induced changes) it is fair to assume that the observed features are due to porphyrin multilayers.

The absence of molecular resolution for the porphyrin molecules was interpreted as due to the higher mobility of the individual molecules in the multilayer regime. This mobility is interpreted as a result of the comparable low interaction in between the porphyrin layers in comparison to the porphyrin-substrate interaction.

The experiments were continued using the metalloporphyrin molecules as evaporant. Co-TPP was chosen as a candidate for the next depositions. Ten minutes was deposition time for the multilayers regime for 2H-TPP. For the Co-TPP experiment, the deposition time has been doubled, ensuring a multilayer deposition. The next series of images shows a selection of eight STM images taken from a series of 65 successive micrographs, obtained after the corresponding Co-TPP deposition on Ag(111). The time passed between Fig.5.6.4a and Fig.5.6.4h is five hours and fifteen minutes.

The tunneling parameters are constant in the first 60 images. The scan direction was horizontal. Again, stripy features can be observed in the images. Interestingly, in this case the stripy features imaged in STM are perpendicular to the scan direction. These features are possibly a result of the tip influence, therefore the tunneling parameter might play an important role. Taking a closer look, to the parameters, there are partial differences between the used parameters for 2H-TPP

and for the Co-TPP. For the last series of images, (61-65) two sets of tunneling parameters were used, and there was no significant difference between the observed features. The last set of tunneling parameters for Co-TPP ($I_{\text{set}} = 0.5\text{nA}$ and $U_{\text{gap}} = -0.9\text{ V}$) is comparable with the ones for the 2H-TPP ($I_{\text{set}} = 0.3\text{ nA}$ and $U_{\text{gap}} = -1.2\text{ V}$). However, also at the indicated comparable conditions, no qualitative change in the observed features (perpendicular to scan direction) in the Co-TPP film could be observed.

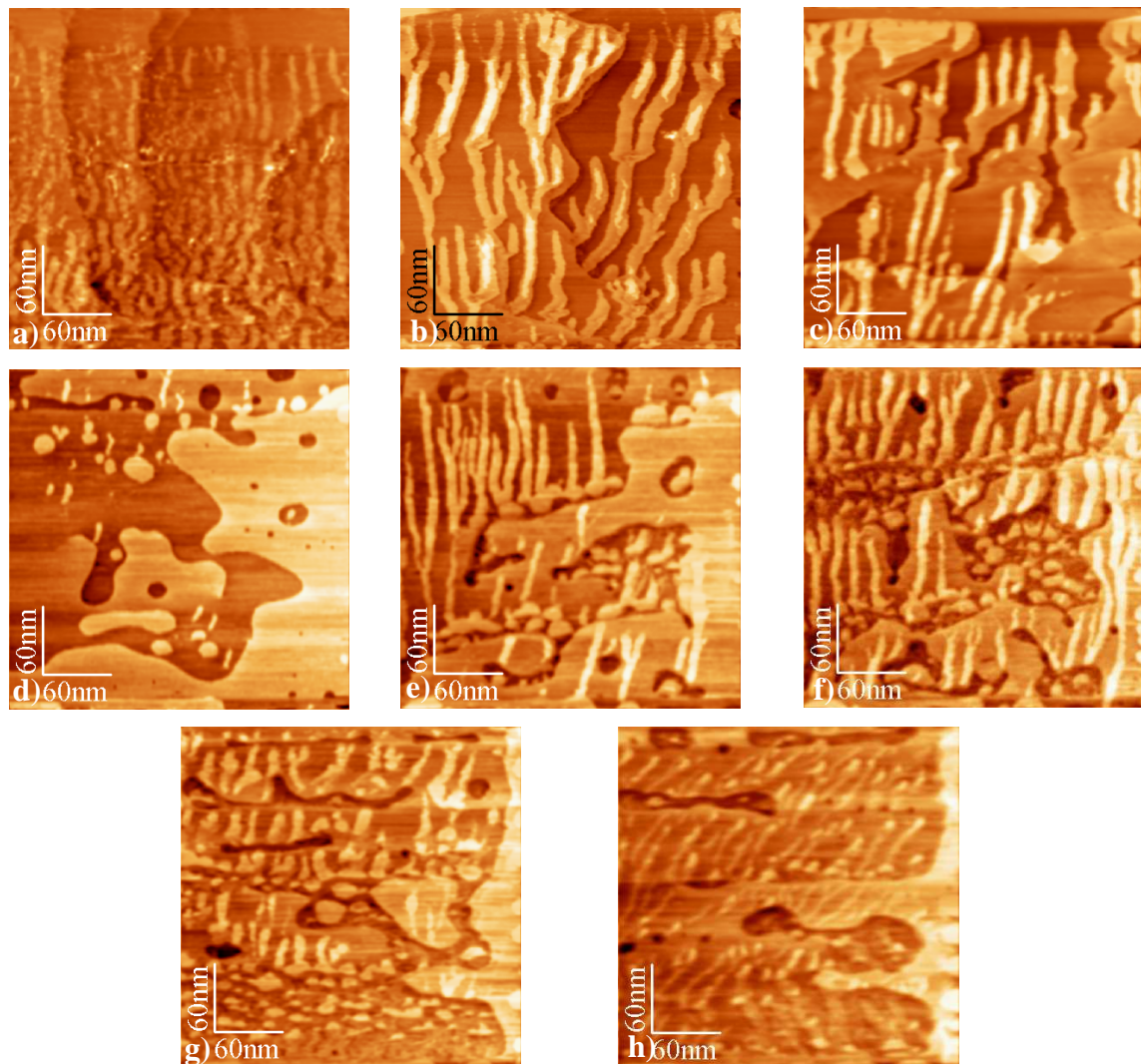


Fig. 5.6.4 STM images from multilayers of Co-TPP. For all the images, the scan range is $300\text{ nm} \times 300\text{ nm}$. The area was scanned with a 1 nA current and a negative bias voltage of -0.6 V . For the last images, the current was 0.5 nA and the negative bias was of -0.9 V .

Another factor that can influence the profile of the images is the scan speed. The scan speed was for the first sixty images of 1 nm/ms which compares quite well

to the value of 0.62 nm/ms and for the 2H-TPP preparation; thus it can be ruled out as the origin of the very different behavior of the prepared Co-TPP and the 2H-TPP film. The last difference left standing is the evaporation time and therewith the film thickness. Another possibility is that the observed differences in the appearance of the stripy features are due to the properties of the different porphyrins or a combination of the film thickness and the latter. At this point, it is not possible to clarify these interesting phenomena, but it should be noted that there is room for further investigations.

The presented results also show that the deposition time, 10 minutes for 2H-TPP and 20 minutes for Co-TPP with the evaporator at 330° C, was sufficient for multilayer deposition.

5.7. Temperature stability of porphyrin layers

After studying the porphyrins at room temperature, it should be evaluated how stable the porphyrin monolayers are after a thermal treatment. In order to elucidate the thermal stability of the adsorbed porphyrin, the STM results are compared with XPS measurements conducted by Thomas Lukascyk in the group of Michael Gottfried [63]. The XPS temperature series experiments were accomplished with a commercial X-ray photoelectron spectrometer (Scienta ESCA-200) equipped with an Al-K α -X-ray source (1486.6 eV) with monochromator and a hemispherical energy analyzer (SES-200) for more details see reference [63].

Fig.5.7.1 displays the C-1s spectra of 10 layers Co-TPP after each temperature interval. Information about the thickness modification and thermal decomposition were obtained by studying the changes in intensity and for the C 1s-signal. The deposition of porphyrins on the silver surface was different for the two experiments. The Co-TPP was evaporated 300 seconds at 673 K. For the XPS temperature series on Co-TPP/Ag(111), the porphyrin was subsequently heated to the indicated temperatures for 30 seconds. All the XPS measurements were performed with the sample at room temperature.

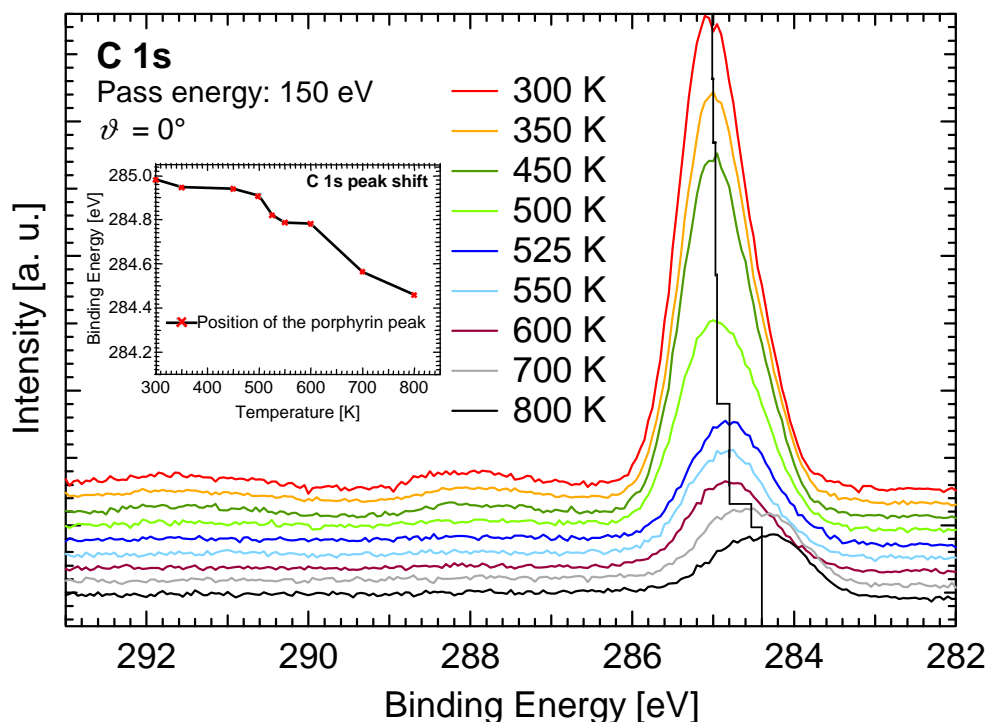


Fig. 5.7.1 XPS- temperature series for Co-TPP/Ag(111), C1s-region. The experiments were realized in a successive way. The inset shows the C 1s-signal position for the temperature series as temperature function [63].

The main signal loses intensity with increasing temperature. This is observable in Fig.5.7.1. This decrease is correlated with the shift of C 1s peak to smaller binding energies. The inset image displays the position of the porphyrin peak. The shift is small until 500 K and this indicates that only the porphyrin molecules from the multilayers are desorbed. The main signal loses intensity and shifts slightly (0.2 eV) towards lower binding energies between 500 K and 525 K. This indicates the multilayer desorption in this temperature range. The intensity of the signal shows no changes until 600 K. To conclude, the temperature does not influence the monolayer in this interval (room temperature to 600 K). Increasing the temperature to 700 K, a peak shift of 0.25 eV is observable. This shift is attributed to porphyrin decomposition. The peak shows another significant shift at 800 K.

These results indicate that above 600 K the decomposition of the monolayer is starting. The results were compared with the STM measurements. Fig.5.7.2 shows STM images of Co-TPP molecules after 30 seconds heating at different temperatures.

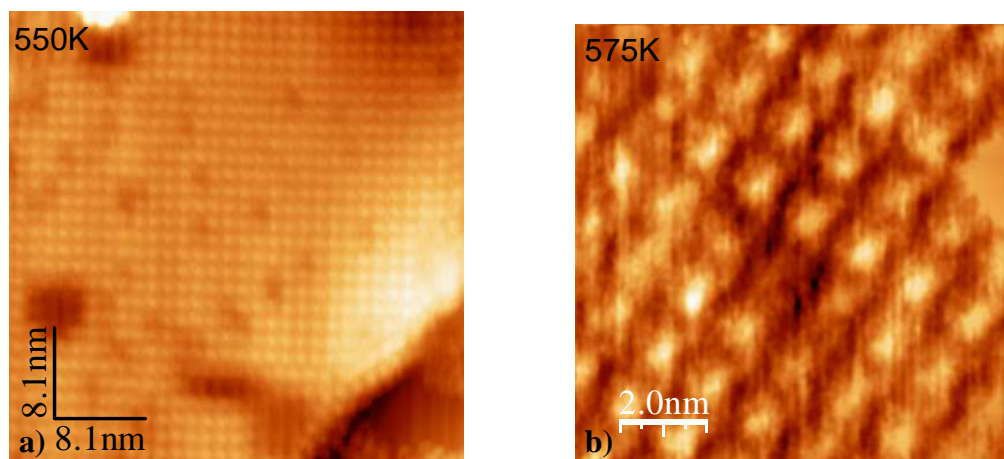


Fig. 5.7.2 STM topographical images of Co-TPP after heating at a) 550 K and b) 575 K. The images were scanned with $I_{set}=0.3\text{ nA}$ and $U_{gap} = -1.2\text{ V}$.

The STM measurements were performed at room temperature. The square arrangement of the molecules is still apparent after heating the sample in the temperature interval from 550 K to 575 K. The measurements show that the molecular arrangement is not disturbed at these temperatures and therefore the corresponding monolayer with the individual molecules appears to be still intact.

Increasing the temperature to 590 K and subsequently acquiring STM data, different phenomena could be tracked. Fig 5.7.3 shows STM images after heating the sample to 590 K.

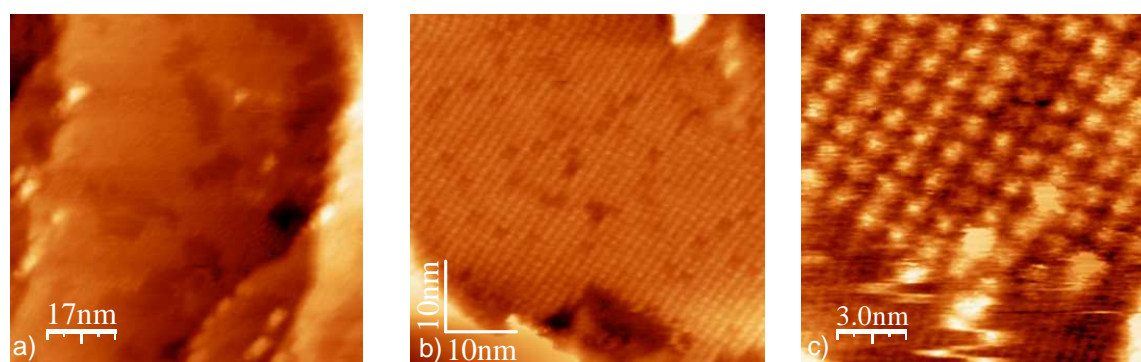


Fig. 5.7.3 STM images of porphyrin molecules after heating at 590 K. (a, b: scan range $50\text{ nm} \times 50\text{ nm}$, $I_{set}=0.3\text{ nA}$, $U_{gap}=-1.2\text{ V}$; c: scan range $15\text{ nm} \times 15\text{ nm}$, $I_{set}=0.3\text{ nA}$, $U_{gap}=-0.1\text{ V}$).

In the STM images, there are presented different regions (b and c) where the porphyrin monolayer is intact and no changes are present in the molecular structure. Fig.5.7.3a shows only a part of the sample where an instable equilibrium between 2D grows and 2D gas phase is observable. In Fig.5.7.3c, the square arrangement with the same lattice vector is observable. Tip induced changes are also observed in the bottom part of Fig.5.8.3c.

After the porphyrin molecules have been heated for 30 seconds at 600 K, the STM images shown in Fig. 5.7.4 were acquired.

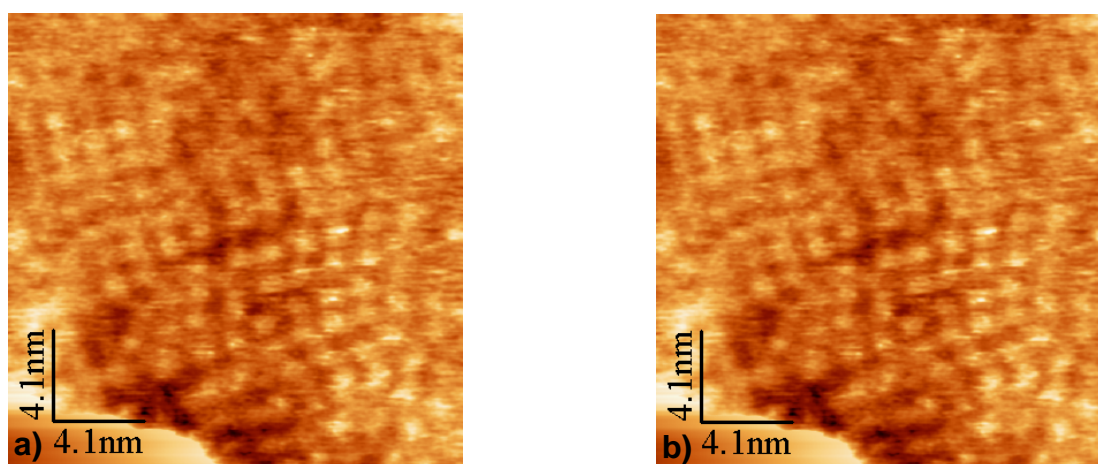


Fig. 5.7.4 Porphyrin molecules after 600 K heating. (Scan range 20.6 nm x 20.6 nm; tunneling current 0.3 nA and a variable bias voltage of a -1.1V and b -1.2V).

The 600 K represented a critical temperature for the porphyrin molecules. Starting from this temperature, in the STM images, there is no regular molecular arrangement observed. No square or no other molecular arrangements have been found for the porphyrin molecules. The results are in agreement with the XPS measurement. It was confirmed that the stability of a monolayer is not essentially influenced by the temperature below 600 K. 600 K is the critical temperature for STM measurements, since only individual molecules can be imaged and no regular molecular arrangement can be found.

6. Summary

In the work at hand a detailed scanning tunneling microscopy study of films of different porphyrin derivatives on a Ag(111) surface has been performed under ultra high vacuum conditions at room temperature. The key focus was put on the porphyrin monolayer regime, the corresponding self-assembled phases and their electronic structure.

Thermal sublimation in vacuum was the applied method to prepare films of various porphyrin molecules. With this method, it was possible to obtain films with high purity in a controlled manner.

The molecular arrangements of the porphyrin molecules on the Ag(111) surface could be determined in detail. All investigated porphyrins in the monolayer regime were found to adsorb with the macrocycle flat-lying on the Ag surface. Two basic types of porphyrin molecules were studied: the “smaller” tetraphenylporphyrins (TPP) as there are 2H-TPP, Zn-TPP and Co-TPP and the more bulky Co-TTBPP. For all TPP molecules, the same long-range molecular order could be observed: a square lattice with a molecule-molecule distance of 1.4 nm. High-resolution STM images revealed the position of the phenyl ligands and therefore allowed also determining the azimuthal orientation of the individual TPPs within the square lattice. These results also enabled to identify T-type interactions between the phenyl ligands as the dominating factor for the stability and the assembly of the observed molecular arrangement. In addition, domains with opposite senses of rotation, thus exhibiting 2D chirality, could be observed.

A particular interesting feature was the bias voltage dependent observation of depressions or “pits” in the monolayers of Co-TPP and Co-TTBPP. These pits could be identified with 2H-TPP and 2H-TTBPP that were present as a contaminant in the purchased Co-TPP and Co-TTBPP powders, respectively. The underlying electronic effects could be explained in detail combining the STM results with UPS measurements.

The temperature stability of the TPP porphyrins could be studied by STM and complementary XPS measurements. It was found that the stability of a monolayer was not essentially influenced by the sample temperature. Starting at 600 K, a gradual

decay of the square arrangement could be observed in STM with increasing temperature. This is in line with the appearance of new features in the corresponding XP spectra, which are indicating the decomposition of the TPP molecules.

STM investigations of TPP molecules in the multilayer regime showed dominant stripy features. The orientation of these features was changing respectively directly correlated with the corresponding scan direction of the STM (in scan direction for 2HTPP, perpendicular to scan direction for Co-TPP).

When studying the adsorption of Co-TTBPP in the monolayer regime, surprisingly, three different molecular arrangements were found: a Square and two hexagonal phases, designated as **hex A** and **hex B**. It could be shown that an exchange of single molecules between the different phases can occur, e.g., from **hex A** to the **square** phase.

8. Zusammenfassung

Im Rahmen der vorliegenden Arbeit wurden verschiedene Metalloporphyrinschichten im Ultrahochvakuum auf Ag(111) untersucht. Das Ultrahochvakuum eröffnet die Möglichkeit die Eigenschaften und Anordnung der Porphyrine im lösungsmittelfreien Zustand auf einer Silberoberfläche zu charakterisieren. Der Schwerpunkt lag auf der Präparation von Porphyrin-Schichten im Bereich einer Monolage, der Untersuchung der molekularen Anordnung sowie der elektronischen Struktur.

Dünne Filme dieser Moleküle wurden durch thermische Sublimation im Vakuum erzeugt. Mit dieser Methode war es möglich, Filme mit hohem Reinheitsgrad in einer kontrollierten Weise zu erhalten.

Die Anordnung der Porphyrin-Moleküle auf der Ag(111)-Oberfläche konnte im Detail aufgeklärt werden. Alle untersuchten Porphyrine adsorbierten dabei planar auf der Silberoberfläche. Zwei grundlegende Arten von Porphyrin-Moleküle wurden verwendet: die „kleineren“ Tetraphenylporphyrine (TTP) (d.h. 2H-TPP, Zn-TPP und Co-TPP), und die größeren Co-TTBPP. Für alle TPP Moleküle konnte eine über große Bereiche geordnete Monolage gefunden werden - ein quadratisches Gitter mit einem Molekül-Molekül-Abstand von 1.4 nm. Hochaufgelöste STM-Bilder zeigten deutlich die Position der Phenylliganden und erlaubten die Bestimmung der azimuthalen Lage der einzelnen TPPs innerhalb des quadratischen Gitters. Dies ermöglichte es auch den Wechselwirkungsmechanismus zwischen den Phenylringen mehrerer Moleküle aufzuklären, der sog. „T-Type“ Wechselwirkung. Diese ist der bestimmende Faktor für die Stabilität und den Zusammenhalt der beobachteten molekularen Anordnung. Zusätzlich konnten Domänen mit unterschiedlicher 2D-Chiralität beobachtet werden.

Eine weitere interessante Beobachtung war das spannungsabhängige Erscheinen von Kavitäten oder „Pits“ in den STM-Aufnahmen einer Monolage von Co-TPP. Diese „Pits“ konnten als 2H-TPP identifiziert werden, da die gekauften Co-TPP Moleküle in Pulverform mit 2H-TPP Molekülen versetzt waren. Die zugrunde liegenden elektronischen Effekte konnten mittels Kombination von UPS- und STM-Messungen aufgeklärt werden.

Die Temperaturbeständigkeit der TPP-Porphyrine wurde durch STM- und ergänzende XPS-Messungen untersucht. Es wurde festgestellt, dass die Stabilität einer Monolage im Wesentlichen nicht durch die Proben temperatur beeinflusst wird. Beginnend bei Temperaturen von 600 K konnte ein stufenweiser Zerfall der quadratischen Anordnung im STM beobachtet werden. Dieses zeigte sich auch in den entsprechenden XP-Spektren, und spricht somit für eine Zersetzung der TPP-Moleküle. STM-Untersuchungen der TPP-Moleküle im Multilagenbereich zeigten hauptsächlich eine typische Streifenform im STM-Bild. Bei der Untersuchung von Co-TTBPP in Monolagenbereich wurden überraschenderweise drei verschiedene molekulare Anordnungen für Co-TTBPP entdeckt: eine quadratische und zwei hexagonale Phasen, gekennzeichnet als Square, hex A und hex B. Es konnte gezeigt werden, dass einzelne Moleküle z.B. von hex A zur quadratischen Phase übergehen können.

List of figures

<i>Fig.1.1 Sketches for the core porphyrin and a typical metalloporphyrin.</i>	5
<i>Fig. 2.1.1 STM principle of work [5].</i>	7
<i>Fig. 2.1.1.1 Difference between classical dynamics and quantum mechanics [7].</i>	9
<i>Fig. 2.1.1.2 The potential barrier.</i>	10
<i>Fig. 2.1.1.3 Scheme for the contact between STM tip and sample.</i>	11
<i>Fig. 2.1.2.1 Scheme for a positively biased sample.</i>	13
<i>Fig. 2.1.2.2 Schematic picture of tunneling geometry.</i>	14
<i>Fig. 2.2.2 Schematic of a quadrupole mass filter.</i>	18
<i>Fig. 2.3.1 Experimental set-up for LEED.</i>	19
<i>Fig. 2.3.2 The solid in cross-section with the electron beam incident normal to the surface from the vacuum above.</i>	20
<i>Fig.2.4.1 Scheme for the UPS experiment.</i>	23
<i>Fig. 3.1.1 Schematic drawing: the UHV 300 STM system [22].</i>	26
<i>Fig. 3.1.2 Scan head top view (photo and schematic draw [22]).</i>	27
<i>Fig. 3.1.3 Top loading sample holder [22].</i>	28
<i>Fig. 3.1.4 STM chamber.</i>	29
<i>Fig. 3.2.1 Preparation chamber.</i>	30
<i>Fig. 3.2.2 The home-built Knudsen cell evaporator.</i>	31
<i>Fig. 3.3.2.2 QMS spectrum for porphyrins compounds.</i>	33
<i>Fig. 4.1.1 All-numbered IUPAC systematic nomenclature on porphyrin macrocycle [24].</i>	36
<i>Fig.4.1.2 Sketches for porphyrins with different substituents.</i>	37
<i>Fig. 4.2.1 a) TTPP deposited on graphite; b) a STM image at 63 K of the Au(111) after the H₂-TPP deposition; c) low-resolution images of Ni-TPP absorbed on Au(111) [47-49].</i>	39

- Fig. 4.2.2** High-resolution constant current STM image of a small region of a single molecule thick island of Co-TPP (A), and Ni-TPP (B) on Au(111). Inserted into the data image are spaces filling models of a typical MTPP [33]. 40
- Fig. 4.2.3** a) High resolution STM image (9x9nm²) of Co-TPP and b) Structural model for Co-TPP adlayer [55]. 41
- Fig. 4.2.4** Conformational identification of Cu-TBPP molecules [53]. 42
- Fig. 4.2.5** Comparison of room-temperature constant current STM images of different organometallics adsorbed on Au(111) imaged under UHV conditions [46]. 43
- Fig. 4.2.6** Constant current tunneling images of mixed composition islands of Ni-TPP and Co-TPP at different bias voltages [33]. 44
- Fig. 4.3.1** Relationship between heme, chlorophyll a, and cobyrinic amide. 46
- Fig. 4.3.2** High-spin, low-spin schema for Co³⁺ (d⁶) and Co²⁺ (d⁷) ions. 47
- Fig. 4.3.3** Splitting of orbital energies in an octahedral, square-bipyramidal, normal square planar complexes or square planar with porphyrin ligand field [61, 62]. 48
- Fig. 4.3.4** Comparison of the submolecular resolved images obtained from the investigated systems. The observed inner structure of the molecules is similar in all cases. a) PTCDA on graphite; b) PTCDA on MoS₂; c) Correlation between the observed tunneling current maxima in the high-resolution images and the molecular structure. 50
- Fig. 4.3.5** a,b) -Frontier orbitals of PTCDA, calculated for a free molecule using the semi-empirical MNDO approximation; c,d) - submolecular image of PTCDA on MoS₂ and Ag(111). 52
- Fig. 4.4.1** A chiral molecule with its mirror image. 53
- Fig. 4.4.2** a) STM images and schematic model of the network structure (scale bar 2nm); b) Large scale STM showing two homochiral domains [77]. 55
- Fig. 4.4.3** STM images of the twin domains of H₂-TBPP on Cu(100) surface, with the upper inset-Cu(100) substrate and the lower inset: H₂-TBPP structure [78]. 56
- Fig. 5.1.1** a) The cubic face centered silver structure and b) the top view of the (111) surface. 57
- Fig. 5.1.2** STM constant current topography of Ag adatom islands and vacancy islands on Ag(111). The image was taken under scanning conditions of $I_{set} = 2.6$ nA and $U_{gap} = -0.3$ V at room temperature. 58
- Fig. 5.1.3** Time evolution of the surface structure from a to d. The tunneling parameters were set as $I_{set} = 1$ nA and $U_{gap} = -0.3$ V. The time interval between first and the last image $t \approx 4$ min. 59

- Fig. 5.1.4** STM topograph of Ag crystal and the profile from this image. The tunneling current is $I_{set} = 1$ nA by a bias voltage of $U_{gap} = -0.43$ V. The scan areas are 2.63×2.63 nm² for the a) image and 5.0×5.0 nm² for the b) image. 60
- Fig. 5.1.5** a), b) High resolution STM imaging for Ag(111) ($U_{gap} = -0.04$ V and $I_{set} = 0.8$ nA) and c) the profile line for measuring the lattice spacing. 60
- Fig. 5.2.1** STM images of the deposited Co-TPP molecules on a Ag(111) surface. The image a) was scanned with a 0.7 nA tunneling current and a negative bias voltage of 0.7 V and b) with a 0.3 nA tunneling current and a negative bias voltage of 1.2 V 62
- Fig. 5.2.3** Series of Zn-TPP images. The Zn-TPP images were scanned with a current of 0.7 nA and a bias voltage of -0.87 V by a scan speed of 200 ms/line. The scan area is 62.5 nm x 62.5 nm. 65
- Fig. 5.2.4** Molecular resolution for the Zn (left) and Co (right) porphyrin molecules. The bias voltage is the same for the two STM images, with a value of -1.2 V, and the tunneling current 0.2 nA for the Zn-TPP and 0.3 nA for Co-TPP. 66
- Fig. 5.2.5** Differences in profile height for the two different porphyrin molecules. 66
- Fig. 5.2.6** a) STM topography of Co-TPP molecules and b) model of metalloporphyrin molecules inserted into STM image. The tunneling parameters were 0.3 nA and a voltage of 1.2 V (the contrast from Fig. 5.4.6 a) is the result of the changed polarity for bias). 67
- Fig. 5.3.1** STM topography of a self-assembled Co-TTBPP film on Ag(111) (tunneling parameters $I_{set} = 0.8$ nA, $U_{gap} = -0.7$ V; scan range: 95 nm x 95 nm). 69
- Fig. 5.3.2** Topography of Co-TTBPP molecules showing the coexistence of the three different molecular arrangements. 70
- Fig. 5.3.4** (a), (b) STM images of Co-TTBPP on Ag(111) imaging the transition of structure in a confident area. (scan range 25 nm x 25 nm, $I_{set} = 0.3$ nA, $U_{gap} = -1.2$ V) and (c), (d) same images illustrating the different type of structure. 73
- Fig. 5.3.5** Imaging single Co-TTBPP molecule ($12,5 \times 12,5$ nm², -1.2 V and 0.3 nA). 74
- Fig. 5.4.1** STM images of Co-TPP in a) and Co-TTBPP in b). The images were taken under scanning condition of $U_{gap} = -1.2$ V and $I_{set} = 0.3$ nA. The scan ranges are 32.7 nm x 32.7 nm for a) and 67 nm x 67 nm for b). 75
- Fig. 5.4.2.** STM 3D plot of Co-TPP with pits. The position of the pits is indicated by the arrows. 76
- Fig. 5.4.3** Two STM micrographs imaging the same area of an ordered layer of Co-TPP with different bias voltages. 77
- Fig. 5.4.4** Scheme for STM and UPS. 78

- Fig. 5.4.5** Comparison between UPS and STM measurements. Upper bias series of STM images show Co-TPP and bottom series Co-TTBPP molecules in their corresponding ordered molecular arrangements. The respective bias voltage position in the UP spectra are indicated with the colored vertical lines. 79
- Fig. 5.4.6** STM topography of 2H-TPP and Co-TPP mixture. (Scan ranges a) 76.6 nm x 76,6 nm; b) 47.8 nm x 47.8 nm; c) 57.2 nm x 57.2 nm and tunneling parameters: bias voltages -1.2 V for a and -1.0 V for b, c; tunneling current 0.3 nA). 81
- Fig. 5.4.7** High resolution image of 2H-TPP and Co-TPP mixture. The zoom image shows the 2H-TPP molecule. ($I_{set} = 0.4$ nA, $U_{gap} = -1.1$ V; scan range 26.8nm x 26.8 nm). 82
- Fig. 5.6.1** LEED patterns for porphyrin molecules for the multilayers regime (a) and monolayers regime (b). The beam voltages were around 18.7 eV; the sample temperature was 370 K for the multilayer pattern and 87 K for the monolayer pattern. 85
- Fig. 5.6.2** Series of topographic images acquired in a time total interval of 37 minutes. The scan area for all the images is 124 x 124 nm². The tunneling parameters were also kept constant at: $I_{set} = 0.3$ nA and $U_{gap} = -1.2$ V. 87
- Fig. 5.6.3** A profile line that shows the terrace height in the STM topography. 88
- Fig. 5.6.4** STM images from multilayers of Co-TPP. For all the images, the scan range is 300 nm x 300 nm. The area was scanned with a 1nA current and a negative bias voltage of -0.6 V. For the last images, the current was 0.5 nA and the negative bias was of -0.9 V. 89
- Fig. 5.7.1** XPS- temperature series for Co-TPP/Ag(111), Cls-region. The experiments were realized in a successive way. The inset shows the C 1s-signal position for the temperature series as temperature function [62]. 91
- Fig. 5.7.2** STM topographical images of Co-TPP after heating at a) 550 K and b) 575 K. The images were scanned with $I_{set}=0.3$ nA and $U_{gap} = -1.2$ V. 92
- Fig. 5.7.3** STM images of porphyrin molecules after heating at 590 K. (a, b: scan range 50 nm x 50 nm, $I_{set}=0.3$ nA, $U_{gap}=-1.2$ V; c: scan range 15nm x 15 nm, $I_{set}=0.3$ nA, $U_{gap}=-0.1$ V). 92
- Fig. 5.7.4** Porphyrin molecules after 600 K heating. (Scan range 20.6 nm x 20.6 nm; tunneling current 0.3 nA and a variable bias voltage of a -1.1V and b -1.2V). 93

Bibliography

- [1] J. K. Gimzewski, T. A. Jung, M. T. Cuberes, R. R. Schlittler, TOYOTA Conference on Atomic, Molecular and Electronic Dynamic Processes on Solid Surfaces, 386, 101.
- [2] M. Furukawa, H. Tanaka, K. Sugiura, Y. Sakata, T. Kawai, *Surface Science* 445 (2000) L58.
- [3] L. Ottaviano, L. Lozzi, S. Santucci, *Surface Science* 431 (1999) 242.
- [4] G. Binnig, H. Rohrer, C. Gerber, E. Weibel, *Applied Physics Letters* 40 (1982) 178.
- [5] M. Schmid, *Trickfilm zur Funktionsweise des Rastertunnelmikroskops*, http://www.iap.tuwien.ac.at/www/surface/STM_Gallery/D-STM-Animation.gif.
- [6] G. Binnig, H. Rohrer, *Reviews of Modern Physics* 59 (1987) 615.
- [7] JAXA, *Tunnel Effect*, http://spaceinfo.jaxa.jp/note/kagaku/e/kag106_tonneru_e.html.
- [8] L. Pauling, E. B. Wilson, *Introduction to quantum mechanics with applications to chemistry*, (1935).
- [9] K. S. Pitzer, *Quantum chemistry*, Prentice-Hall, INC, (1961).
- [10] T. Fauster, *STM tutorial*, <http://www.fkp.uni-erlangen.de/methoden/stmtutor/stmpage.html>.
- [11] J. G. Simmons, *Journal of Applied Physics* 34 (1963) 1793.
- [12] J. Tersoff, D. R. Hamann, *Phys. Rev. Lett.* 51 - PRL 50 (1983) 1998 LP.
- [13] J. Tersoff, D. R. Hamann, *Phys. Rev. B* 31 (1985) 805.
- [14] J. B. Feen, *Home-page*, <http://www.has.vcu.edu/che/people/bio/fenn.html>.
- [15] W. Bechmann, J. Schmidt, *Struktur-und Stoffanalytik mit spektroskopischen Methoden*, B.G. Teubner Stuttgart-Leipzig-Wiesbaden, (2000).
- [16] C. Davisson, L. H. Germer, *Phys. Rev.* 51 - PR 30 (1927) 705 LP.
- [17] V. Ertl, J. Küppers, *Low energy electrons and surface chemistry*, VCH Verlagsgesellschaft mbH, Weinheim (1985).
- [18] J. W. May, *Advances in Catalysis* 21 (1970) 151.

- [19] E. A. Wood, *Journal of Applied Physics* 35 (1964) 1306.
- [20] R. L. Park, J. Madden, Hannibal H., *Surface Science* 11 (1968) 188.
- [21] K. Besocke, *Surface Science* 181 (1987) 145.
- [22] RHKTechnology, *UHV 300 User's guide*, Rochester Hills, Michigan USA.
- [23] R. P. Lindner, *Modifikation des Wachstums von Kupfer auf Ni(111) untersucht mit dem Rastertunnelmikroskop*, (2004).
- [24] M. Hesse, H. Meier, B. Zeeh, *Spektroskopische Methoden in der organischen Chemie*, 7. Auflage, Thieme, Stuttgart, (2005).
- [25] L. R. Milgrom, *The colours of life- an introduction to the chemistry of porphyrins and related compounds*, (1997).
- [26] *The Oxford English Dictionary, XII*, 2nd Edition, Clarendon Press, Oxford (1989).
- [27] H. T. American, *The American Heritage ® Dictionary of the English language, 2000*, fourth Edition, Houghton Mifflin Company.
- [28] R. E. Palmer, Q. Guo, *Physical Chemistry Chemical Physics* 4 (2002) 4275.
- [29] A. Tepore, A. Serra, D. Manno, L. Valli, G. Micocci, D. P. Arnold, *Journal of Applied Physics* 84 (1998) 1416.
- [30] C. H. M. Maree, S. J. Roosendaal, T. J. Savenije, R. E. I. Schropp, T. J. Schaafsma, F. Habraken, *Journal of Applied Physics* 80 (1996) 3381.
- [31] Y. Harima, H. Okazaki, Y. Kunugi, K. Yamashita, H. Ishii, K. Seki, *Applied Physics Letters* 69 (1996) 1059.
- [32] C.-Y. Liu, H.-I. Pan, M. A. Fox, A. J. Bard, *Science* 261 (1993) 897.
- [33] J. R. Reimers, T. X. Lu, M. J. Crossley, N. S. Hush, *Nanotechnology* 7 (1996) 424.
- [34] L. Scudiero, D. E. Barlow, K. W. Hipps, *Journal of Physical Chemistry B* 104 (2000) 11899.
- [35] N. Batina, M. Kunitake, K. Itaya, *Journal of Electroanalytical Chemistry* 405 (1996) 245.
- [36] M. Kunitake, U. Akiba, N. Batina, K. Itaya, *Langmuir* 13 (1997) 1607.
- [37] M. Kunitake, N. Batina, K. Itaya, *Langmuir* 11 (1995) 2337.
- [38] D. E. Barlow, K. W. Hipps, *Journal of Physical Chemistry B* 104 (2000) 5993.

- [39] M. Lackinger, M. Hietschold, *Surface Science* 520 (2002) L619.
- [40] R. Strohmaier, C. Ludwig, J. Petersen, B. Gompf, W. Eisenmenger, *Journal of Vacuum Science & Technology B* 14 (1996) 1079.
- [41] K. W. Hipps, X. Lu, X. D. Wang, U. Mazur, *Journal of Physical Chemistry* 100 (1996) 11207.
- [42] S. B. Lei, *J.Phys.Chem.B* 105 (2001) 10838.
- [43] K. Itaya, *Progress in Surface Science* 60 (1999) 87.
- [44] M. D. Upward, P. H. Beton, P. Moriarty, *Surface Science* 441 (1999) 21.
- [45] S. M. Bayliss, S. Heutz, G. Rumbles, T. S. Jones, *Physical Chemistry Chemical Physics* 1 (1999) 3673.
- [46] I. Yin, Q. Guo, R. E. Palmer, N. Bampos, J. K. M. Sanders, *Journal of Physical Chemistry B* 107 (2003) 209.
- [47] L. Scudiero, K. W. Hipps, D. E. Barlow, *Journal of Physical Chemistry B* 107 (2003) 2903.
- [48] S. B. Lei, J. Wang, Y. H. Dong, C. Wang, L. J. Wan, C. L. Bai, *Surface and Interface Analysis* 34 (2002) 767.
- [49] T. Yokoyama, S. Yokoyama, T. Kamikado, S. Mashiko, *Journal of Chemical Physics* 115 (2001) 3814.
- [50] T. A. Jung, R. R. Schlittler, J. K. Gimzewski, H. Tang, C. Joachim, *Science* 271 (1996) 181.
- [51] P. Sautet, C. Joachim, *Surface Science* 271 (1992) 387.
- [52] P. Sautet, C. Joachim, *Chemical Physics Letters* 185 (1991) 23.
- [53] C. Chavy, C. Joachim, A. Altibelli, *Chemical Physics Letters* 214 (1993) 569.
- [54] T. A. Jung, R. R. Schlittler, J. K. Gimzewski, *Nature* 386 (1997) 696.
- [55] S. Yoshimoto, A. Tada, K. Suto, R. Narita, K. Itaya, *Langmuir* 19 (2003) 672.
- [56] S. Yoshimoto, J. Inukai, A. Tada, T. Abe, T. Morimoto, A. Osuka, H. Furuta, K. Itaya, *Journal of Physical Chemistry B* 108 (2004) 1948.
- [57] K. W. Hipps, L. Scudiero, D. E. Barlow, M. P. Cooke, *Journal of the American Chemical Society* 124 (2002) 2126.

- [58] X. Lu, K. W. Hipps, X. D. Wang, U. Mazur, *Journal of the American Chemical Society* 118 (1996) 7197.
- [59] X. Lu, K. W. Hipps, *Journal of Physical Chemistry B* 101 (1997) 5391.
- [60] W. Han, E. N. Durantini, T. A. Moore, A. L. Moore, D. Gust, P. Rez, G. Leatherman, G. R. Seely, N. Tao, S. M. Lindsay, *J. Phys. Chem. B* 101 (1997) 10719.
- [61] C. Rovira, K. Kunc, J. Hutter, M. Parrinello, *Inorganic Chemistry* 40 (2001) 11.
- [62] C. Yaniak, T. M. Klapötke, H.-J. Meyer, *Moderne anorganische chemie*, 1 auflage, (1999).
- [63] T. Lukasczyk, "Adsorption und reaktion von metalloporphyrinen auf einer Ag(111) oberfläche"-diplomarbeit, (2005).
- [64] G. L. Miessler, D. A. Tarr, *Inorganic chemistry*, (2004).
- [65] M.-S. Liao, S. Scheiner, *Journal of Computational Chemistry* 23 (2002) 1391.
- [66] H. Ohtani, R. J. Wilson, S. Chiang, C. M. Mate, *Phys. Rev. Lett.* 60 (1988) 2398 LP.
- [67] P. H. Lippel, R. J. Wilson, M. D. Miller, C. Wöll, S. Chiang, *Phys. Rev. Lett.* 62 (1989) 171 LP.
- [68] C. Ludwig, B. Gompf, W. Glatz, J. Petersen, W. Eisenmenger, M. Möbus, U. Zimmermann, N. Karl, *Zeitschrift für Physik B Condensed Matter* 86 (1992) 397.
- [69] C. Ludwig, B. Gompf, J. Petersen, R. Strohmaier, W. Eisenmenger, *Zeitschrift für Physik B Condensed Matter* 93 (1994) 365.
- [70] A. Hoshino, S. Isoda, H. Kurata, T. Kobayashi, *Journal of Applied Physics* 76 (1994) 4113.
- [71] J. Bardeen, *Phys. Rev. Lett.* 6 (1961) 57.
- [72] A. J. Fisher, P. E. Blöchl, *Phys. Rev. Lett.* 70 (1993) 3263 LP.
- [73] P. Sautet, C. Joachim, *Ultramicroscopy* 42-44 (1992) 115.
- [74] H. Ou-Yang, R. A. Marcus, B. Kallebring, *J. Chem. Phys.* 100 (1994) 7814.
- [75] R. Strohmaier, J. Petersen, B. Gompf, W. Eisenmenger, *Surface Science* 418 (1998) 91.
- [76] L. Scudiero, D. E. Barlow, U. Mazur, K. W. Hipps, *Journal of the American Chemical Society* 123 (2001) 4073.

- [77] G. P. Lopinski, D. J. Moffatt, D. D. Wayner, R. A. Wolkow, *Nature* 392 (1998) 909.
- [78] S. Weigelt, C. Busse, L. Petersen, E. Rauls, B. Hammer, K. V. Gothelf, F. Besenbacher, T. R. Linderoth, *Nature Materials* 5 (2006) 112.
- [79] T. Sekiguchi, Y. Wakayama, S. Yokoyama, T. Kamikado, S. Mashiko, *Thin Solid Films* 464-65 (2004) 393.
- [80] S. Stepanow, N. Lin, F. Vidal, A. Landa, M. Ruben, J. V. Barth, K. Kern, *Nano Letters* 5 (2005) 901.
- [81] Y. Wang, W. Wang, K.-N. Fan, J. Deng, *Surface Science* 490 (2001) 125.
- [82] J. T. Li, W. D. Schneider, R. Berndt, S. Crampin, *Phys. Rev. Lett.* 80 (1998) 3332.
- [83] N. Quaas, M. Wenderoth, R. G. Ulbrich, *Surface Science* 550 (2004) 57.
- [84] T. Kamikado, T. Sekiguchi, S. Yokoyama, Y. Wakayama, S. Mashiko, *Thin Solid Films* 499 (2006) 329.
- [85] D. E. Barlow, L. Scudiero, K. W. Hipps, *Langmuir* 20 (2004) 4413.
- [86] Meyer Emmanuel A., Ronald K. Castellano, François Diederich, *Angewandte Chemie International Edition* 42 (2003) 1210.
- [87] F. Buchner, *in preparation*
- [88] T. Lukasczyk, K. Flechtner, L. R. Merte, N. Jux, F. Maier, J. M. Gottfried, H.-P. Steinruck, *J. Phys. Chem. C* 111 (2007) 3090.
- [89] N. Lin, A. Dmitriev, J. Weckesser, J. V. Barth, K. Kern, *Angewandte Chemie-International Edition* 41 (2002) 4779.
- [90] H. Yanagi, H. Mukai, K. Ikuta, T. Shibutani, T. Kamikado, S. Yokoyama, S. Mashiko, *Nano Lett.* 2 (2002) 601.
- [91] J. K. Gimzewski, C. Joachim, R. R. Schlittler, V. Langlais, H. Tang, I. Johansen, *Science* 281 (1998) 531.
- [92] M. O. Lorenzo, C. J. Baddeley, C. Muryn, R. Raval, *Nature* 404 (2000) 376.

Acknowledgements

I would like to thank everyone who has contributed to the successful completion of my dissertation:

- Prof. Dr. Hans-Peter Steinrück, particularly, for the possibility to accomplish this work in his scientific working group and support.
- Dr. Florian Maier for helping me to gain insights in the field of surface science, for careful guidance through the STM and UHV equipments, and for many new ideas and open discussions.
- Dr. Hubertus Marbach for the consistent support, encouragement and advice through all the time here. I am grateful for the very fruitful discussions concerning my work, which helped to develop consistent interpretation of the STM results.
- Florian Buchner for cooperation and a very good working atmosphere in the STM laboratory.
- Dr. Michael Gottfried, Ken Flechtner and Thomas Lukasczyk for the additional UPS, XPS measurements and discussions.
- Norman Schmidt for the first QMS measurement and LEED experiments.
- Hans-Peter Bäumler, our electronics engineer, and Friedhold Wölfel and all his co-workers of the mechanic workshop for the constant advice for all possible technical problems.
- All members of the “Lehrstuhl für Physikalische Chemie II” for the pleasant working atmosphere.
- My parents and my brother, for their outstanding support.
- Last but not least, Radu, my husband, for the great help, support, love and understanding.

Lebenslauf

Persönliche Daten:

Name : Comanici
Vorname : Karmen
Geburtsdatum : 09.08.1977
Geburtsort : Călărași, Rumänien
Familienstand : Verheiratet, keine Kinder

Schulbildung:

1984 – 1992 Grundschole
1992 – 1996 M. Eminescu Gymnasium Calarasi Rumänien

Studium:

1998 – 2002 Studium der Physik an der Babes - Bolyai Universität
Klausenburg Rumänien
2002 Diplomarbeit
2002 – 2003 Masterstudium an der Babes - Bolyai Universität
Klausenburg Rumänien

Promotion:

2004 -2007 wissenschaftlicher Mitarbeiter am Lehrstuhl für
Physikalische Chemie II, FAU Erlangen Nürnberg